Liquid xenon detectors for particle physics and astrophysics

E. Aprile

Department of Physics, Columbia University, New York, New York 10027, USA

T. Doke

Advanced Research Institute for Science and Engineering, Waseda University, Tokyo 169-8555, Japan

(Published 29 July 2010)

This article reviews the progress made over the last 20 years in the development and applications of liquid xenon detectors in particle physics, astrophysics, and medical imaging experiments. A summary of the fundamental properties of liquid xenon as radiation detection medium, in light of the most current theoretical and experimental information is first provided. After an introduction of the different type of liquid xenon detectors, a review of past, current, and future experiments using liquid xenon to search for rare processes and to image radiation in space and in medicine is given. Each application is introduced with a survey of the underlying scientific motivation and experimental requirements before reviewing the basic characteristics and expected performance of each experiment. Within this decade it appears likely that large volume liquid xenon detectors operated in different modes will contribute to answering some of the most fundamental questions in particle physics, astrophysics, and cosmology, fulfilling the most demanding detection challenges. From detectors based solely on liquid xenon (LXe) scintillation, such as in the MEG experiment for the search of the rare "$\mu \rightarrow e\gamma$" decay, currently the largest liquid xenon detector in operation, and in the XMASS experiment for dark matter detection, to the class of time projection chambers which exploit both scintillation and ionization of LXe, such as in the XENON dark matter search experiment and in the Enriched Xenon Observatory for neutrinoless double beta decay, unrivaled performance and important contributions to physics in the next few years are anticipated.

DOI: 10.1103/RevModPhys.82.2053 PACS number(s): 95.35.+d, 29.40.Mc, 95.55.Vj

CONTENTS

I. INTRODUCTION

This article is concerned with liquid xenon as radiation detector medium and the experiments which use it in search of answers to some of the most intriguing questions in physics today. It is a tribute to the vision of those investigators who recognized early on the opportunity that this material would offer for particle detectors and who have continued their effort in the field for more than 30 years, inspiring new generations. Their vision and persistent work has significantly contributed to the successful realization of today's experiments using large scale liquid xenon detectors.

Historically, the advantages of liquid xenon for radiation detection were first recognized by Alvarez in 1968 (Alvarez, 1968). Simultaneously with the development of the first liquid xenon ionization detector by the Berkeley group, independent groups in Russia and Japan have also carried out experiments to study the fundamental properties of liquid xenon for radiation detection. From the seminal work of Dolgoshein *et al.* (1967), Doke (1980), and Kubota and co-workers (Kubota *et al.*, 1978) to the first development of a large volume liquid xenon time projection chamber as a Compton telescope (Aprile *et al.*, 1989), we have seen an evolution in liquid xenon detectors and their application in different fields. Exploiting the original idea by Dolgoshein of electron emission from the liquid to the gas, two-phase time projection chambers with single electron detection capability have been developed to search for dark matter particles. From space-based detectors for astrophysical gamma rays to detectors located at accelerators or deep underground in search of rare decays expected from physics beyond the standard model, liquid xenon remains the preferred medium for many reasons. Among liquid rare gases, liquid xenon has the highest stopping power for penetrating radiation, thanks to its high atomic number and density. It also has the highest ionization and scintillation yield, the latter comparable to that of NaI(Tl) and with a faster time response. Compared to all other detector media, liquid rare gases have the unique feature of responding to radiation with both ionization electrons and scintillation photons. Detectors which use both signals with high detection efficiency have a significant advantage in the measurement of the properties of the radiation. In recent years, much progress has been made in the development of photodetectors with high quantum efficiency at the 178 nm wavelength of the liquid xenon scintillation. Simultaneously, progress in the development of cryocoolers with sufficient power to liquefy and maintain the liquid temperature has enabled reliable detector operation. The relatively warm temperature of liquid xenon, compared to other liquid rare gases, makes the removal of electronegative contaminants more difficult to achieve since at colder temperatures, many impurities freeze out. On the other hand, purification systems with continuous cleaning through commercial purifiers have shown the required level of purity in large volume liquid xenon detectors. The current challenge for several experiments is in the stringent radio-purity requirement for all materials in contact with the liquid, from containment vessels and cryocoolers to photon and charge read-out sensors. Through materials selection and screening, the background level and the sensitivity of liquid xenon experiments for rare event searches continue to improve. Twenty years ago the standard size of a liquid xenon detector was limited to a few hundred grams of mass. Ten years ago the LXeGRIT and the RAPID time projection chambers had a mass of 30 and 60 kg, respectively. Today the XENON100 and the Enriched Xenon Observatory (EXO) time projection chambers have a mass of about 200 kg. The MEG experiment is currently operating the largest liquid xenon scintillating calorimeter with a mass of 2.7 tons. Several other detectors from 300 kg to 3 tons are under construction or are planned for the next few years. Most of the success of liquid xenon detectors can be attributed to the richness of the information contained in its charge and light signals. Looking back at the development over the last 20 years, it seems appropriate to summarize our current understanding and the status of the field.

The article is organized as follows. In Sec. II we summarize the properties of liquid xenon as detector medium, based on well-established experimental knowledge, some dating back more than 50 years, but accounting for the most recent work. In Sec. III, we review the basic operating principle of different type of detectors while the last section covers the applications of liquid xenon detectors in physics, astrophysics, and medical imaging experiments. Some selection was necessary, largely to comply with the length limit for this review, but we have tried to include the majority of current and planned experiments. We have included our own research work on many of the topics and experiments discussed in this review but have attempted also to cover all important contributions from other groups and apologize for any omission.

II. PROPERTIES OF LIQUID XENON AS DETECTOR MEDIUM

We review here the most important physical and operational properties of liquid xenon (LXe) as a detector medium for different types of particles. A unique and important feature of LXe, shared only by liquid argon (LAr) among liquid rare gases and specific to this class of materials, is the production of both charge carriers and scintillation photons in response to radiation. The charge and light signals are highly complementary and anticorrelated. When detected simultaneously and with high efficiency, the two signals enable a precise measurement of the particle's properties from its energy and interactions history in space and time to its type.

A. Physical properties of liquid xenon

Table I summarizes the physical properties of LXe critical to its function as a detector medium (Hollis Hallet, 1961; Crawford *et al.*, 1977; Gruhn and Loveman,

TABLE I. Physical properties of liquid xenon.

Property	Value
Atomic number Z	54
Isotopes	^{124}Xe(0.09%), ^{126}Xe(0.09%), ^{128}Xe(1.92%), ^{129}Xe(26.44%) ^{130}Xe(4.08%), ^{131}Xe(21.18%) ^{132}Xe(26.89%), ^{134}Xe(10.44%) ^{136}Xe(8.87%)
Mean atomic weight A	131.30
Density	3 g cm^{-3}
Boiling point	T_b=165.05 K, P_b=1 atm ρ_b=3.057 g cm^{-3}
Critical point	T_c=289.72 K, P_c=58.4 bars ρ_c=1.11 g cm^{-3}
Triple point	T_t=161.3 K, P_t=0.805 bar ρ_t=3.08 g cm^{-3}
Volume ratio ($\rho_{\text{liquid}}/\rho_{\text{gas}}$)	519
Thermal properties	
Heat capacity	10.65 cal g mol^{-1} K^{-1} for 163–166 K
Thermal conductivity	16.8×10^{-3} cal s^{-1} cm^{-1} K^{-1}
Latent heat of	
(a) evaporation at triple point	3048 cal g mol^{-1}
(b) fusion at triple point	548.5 cal g mol^{-1}
Electronic properties	
Dieletric constant	ϵ_r=1.95

1977; Schmidt, 2001). The high atomic number (54) and high density (~3 g/cm^3) of LXe make it very efficient to stop penetrating radiation. Compared to a crystal scintillator such as NaI (Tl) or to a semiconductor such as Ge, LXe offers the high stopping power benefit in a single large and homogeneous volume, which is not easily possible with the other media. The presence of many isotopes in natural Xe, with different spin and at a non-negligible isotopic abundance, is of interest for different physics applications, as we discuss in Sec. IV.

Figure 1 shows a phase diagram of crystalline, liquid, and gaseous xenon (Hollis Hallet, 1961). At atmospheric pressure, the liquid phase of Xe extends over a narrow temperature range, from about 162 to 165 K. The relatively high boiling point temperature of LXe, compared to other liquid rare gases, requires a modest cryogenics system for gas liquefaction.

B. Electronic structure

The electronic band structure picture is useful for understanding the ionization and the scintillation processes

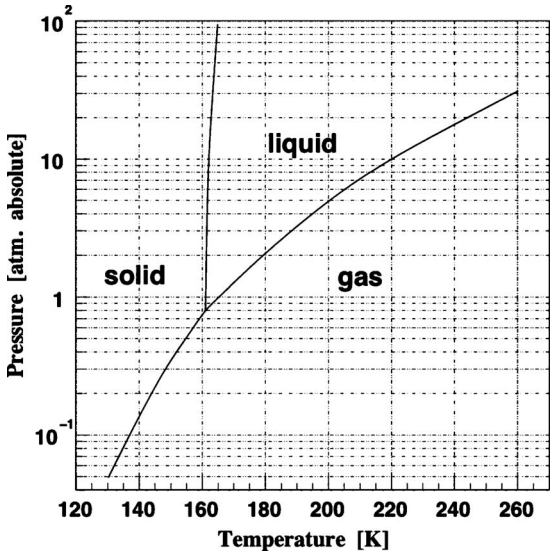

FIG. 1. Phase diagram of xenon.

in LXe. Solid rare gases are excellent insulators. They are crystals with a face-centered-cubic structure. With the exception of solid helium, they have electronic band structures despite the very weak atomic interactions due to van der Waals forces. Absorption spectroscopy provides the most direct method to measure the band-gap energy E_g, which is the energy difference between the bottom of the conduction band and the top of the valence band, as in a semiconductor or an insulator. Figure 2 shows the high-resolution absorption spectra for solid Ar, Kr, and Xe from which the band gaps have been determined [see Schwenter, Kock, and Jortner (1985), and references therein]. Exciton peaks were clearly observed in these spectra, providing direct evidence of the band structure of the solid rare gases. The observation of the exciton level (Beaglehole, 1965; Steinberger and Asaf, 1973) and the direct measurement of the band-gap energy of LXe, LAr, and LKr (Asaf and Steinberger, 1974; Reininger *et al.*, 1982, 1984; Bernstorff *et al.*, 1983) determined that the liquids also have a band structure (see Table II). Given the large band gap, liquid rare gases are also excellent insulators.

C. Ionization process

In rare gases, the energy deposited by radiation is expended in the production of a number of electron-ion pairs N_i, excited atoms N_{ex}, and free electrons with a kinetic energy lower than the energy of the first excited level, known as subexcitation electrons.

We can express the transfer of the deposited energy E_0 into ionization, excitation, and subexcitation electrons by an energy balance equation, as originally proposed by Platzman for rare gases (Platzman, 1961):

$$E_0 = N_i E_i + N_{\text{ex}} E_x + N_i \epsilon, \tag{1}$$

where N_i is the number of electron-ion pairs produced at an average expenditure of energy E_i, N_{ex} is the number

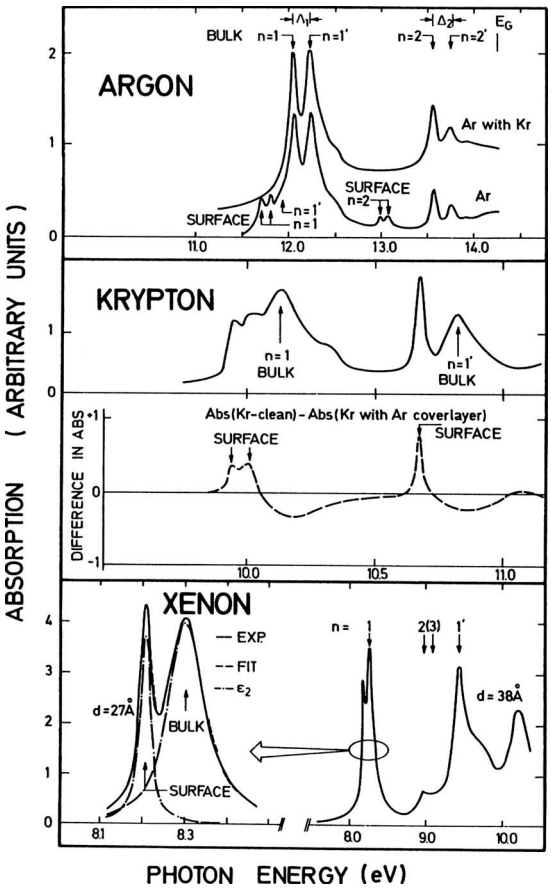

FIG. 2. High-resolution absorption spectra for solid Ar, Kr, and Xe in the range of the valence excitons. Volume and surface excitons are observed for all three samples. For Ar and Kr the results of surface coverage experiments are also shown. For Xe the experimentally determined spectrum in the range of the $n=1$ surface and volume exciton is displayed on an expanded scale together with a line-shape analysis. From Schwenter, Kock, and Jortner, 1985.

of excited atoms at an average expenditure of energy E_x, and ϵ is the average kinetic energy of subexcitation electrons. The W value is defined as the average energy required to produce one electron-ion pair and is given as

TABLE II. Ionization potentials or gap energies and W values in liquid argon, krypton, and xenon.

Material	Ar	Kr	Xe
Gas			
Ionization potential I (eV)	15.75	14.00	12.13
W values (eV)	26.4[a]	24.2[a]	22.0[a]
Liquid			
Gap energy (eV)	14.3	11.7	9.28
W value (eV)	23.6±0.3[b]	18.4±0.3[c]	15.6±0.3[d]

[a]Doke (1969).
[b]Miyajima *et al.* (1974).
[c]Aprile *et al.* (1993).
[d]Takahashi *et al.* (1975).

$$W = E_0/N_i = E_i + E_x(N_{ex}/N_i) + \epsilon. \quad (2)$$

In solid or liquid rare gases, the established existence of an electronic band structure allows us to rewrite the Platzman equation with the band-gap energy E_g replacing the ionization potential of the gas:

$$W/E_g = E_i/E_g + (E_x/E_g)(N_{ex}/N_i) + \epsilon/E_g. \quad (3)$$

To calculate W/E_g for LXe, the ratios E_x/E_g and N_{ex}/N_i were estimated using the oscillator strength spectrum of solid Xe obtained from photoabsorption data, in the optical approximation (Takahashi *et al.*, 1975). For E_i, the data of Rossler (1971) are used, assuming the width of the valence band to be negligibly small. For an estimate of ϵ, the Shockley model (Shockley, 1961; Doke *et al.*, 1976) was used. The calculated ratio W/E_g is about 1.65 for LXe, LAr, and LKr, in good agreement with the measured value of about 1.6 for all three liquids, reported in Table II. This supports the electronic band structure assumption for the liquid rare gases heavier than Ne.

1. Ionization yield

The ionization yield is defined as the number of electron-ion pairs produced per unit absorbed energy. In radiation chemistry, the G value is usually used as such unit, defined to be the average number of electron-ion pairs produced per 100 eV of absorbed energy. In physics, however, we prefer to use the W value, which is inversely proportional to G. Since the W value depends weakly on the type and the energy of the radiation, except for very low energies, we consider it to be almost constant. Therefore the ionization signal produced in a LXe detector can be used to measure the deposited energy. To correctly measure the number of electron-ion pairs produced by radiation in LXe, one needs (a) to minimize the loss of charge carriers by attachment to impurities, i.e., the liquid has to be ultrapure; (b) to minimize the recombination of electron-ion pairs and thus collect all the original charge carriers produced, i.e., by applying a very high electric field; and (c) to estimate the deposited energy correctly. Measurements of the ionization yield in LXe have been carried out with small gridded ionization chambers that met these requirements, irradiated with electrons and gamma rays from internal radioactive sources. From these measurements, the W value is inferred by extrapolation to infinite field. Table II summarizes the measured W values in LAr, LKr, and LXe (Doke, 1969; Miyajima *et al.*, 1974; Takahashi *et al.*, 1975; Aprile *et al.*, 1993); they are smaller than the corresponding W values in gaseous Ar, Kr, and Xe (also shown, along with the ionization potential of the gas). LXe has the smallest W value, hence the largest ionization yield, of all liquid rare gases.

As discussed, the energy lost by radiation in LXe is expended in ionization, excitation, and subexcitation electrons. The average energy lost in the ionization process is slightly larger than the ionization potential or the gap energy because it includes multiple ionization pro-

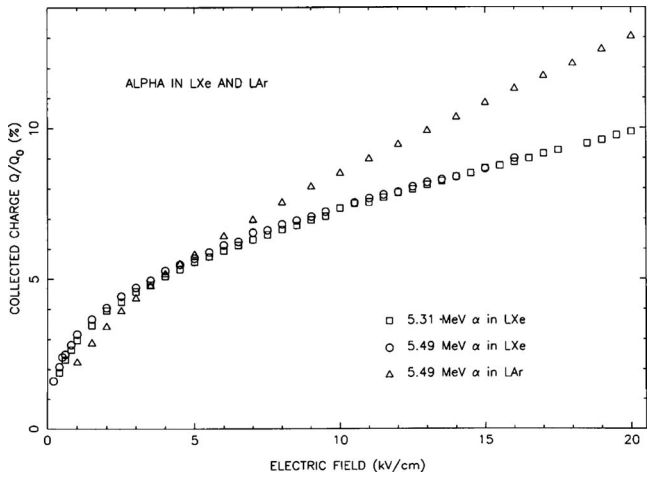

FIG. 3. Collected charge (Q/Q_0%) as a function of electric field for ^{210}Po in liquid xenon (squares) and ^{241}Am in liquid xenon (circles) and liquid argon (triangles) (Aprile, Mukherjee, and Suzuki, 1991b).

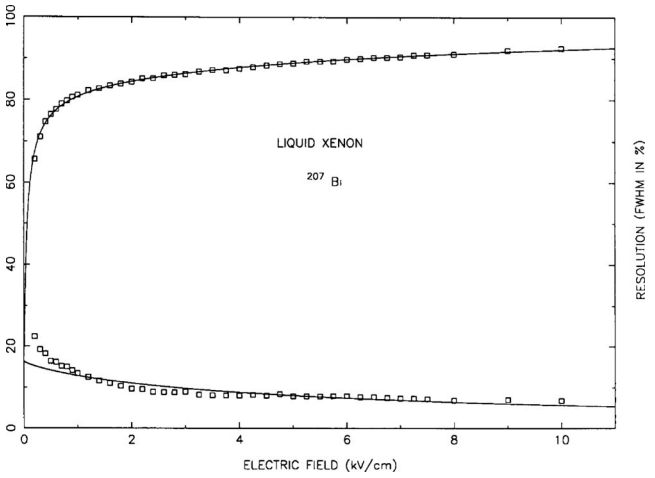

FIG. 4. Energy resolution and collected charge for 570 keV gamma rays in LXe as a function of electric field (Aprile, Mukherjee, and Suzuki, 1991a).

cesses. The average energy lost in the excitation process is comparatively small [~5% (Takahashi *et al.*, 1975; Aprile *et al.*, 1993]. The energy transferred to subexcitation electrons is larger than 30% of the ionization potential or gap energy. As a result, the ratio of the W value to the ionization potential or the gap energy is 1.7–1.8 for rare gases (Platzman, 1961), 1.6–1.7 for liquid rare gases (Takahashi *et al.*, 1975; Aprile *et al.*, 1993) and ~2.8 for semiconductors with a wide conduction and valence bands (Klein, 1968). In 1992, Seguinot *et al.* reported a small W value of 9.76±0.76 eV for LXe, using an electron beam with a kinetic energy of 100 keV (Seguinot *et al.*, 1992). This value is just slightly higher than the band-gap energy of solid xenon [9.33 eV (Zimmerer, 1998)], and the ratio W/E_g=1.046 is too small and inconsistent with the above considerations. See Miyajima, Sasaki, and Shibamura (1995) for a critical analysis of these data.

Measurements of the ionization yield of heavily ionizing alpha particles in LXe have also been carried out [see Aprile, Mukherjee, and Suzuki (1991b), and references therein] as they provide important information on the electron-ion recombination process. Alpha particles have a cylindrical track in which most of the energy is lost in a dense core with a high recombination rate, surrounded by a sparse "penumbra" of delta rays. Complete charge collection for alpha particles is thus difficult, and indeed less than 10% of the total charge is typically collected at an electric field as high as 20 kV/cm. Figure 3 shows the characteristic nonsaturation feature of the ionization yield of alpha particles in LXe and LAr, for comparison (Aprile, Mukherjee, and Suzuki, 1991b). The different ionization densities of alpha tracks in the two liquids explain the different slope of the saturation curves. On the other hand, almost complete charge collection at modest electric fields is possible for minimum ionizing particles. Figure 4 shows a typical saturation curve, or charge collected as a function of field, measured for 570 keV gamma rays in a gridded ionization chamber (Aprile, Mukherjee, and Suzuki, 1991a). The corresponding energy resolution is also shown.

Existing models (Jaffé, 1913; Onsager, 1938; Kramers, 1952; Thomas, Imel, and Biller, 1988; Mozumder, 1995) explain some of the experimental data, for various special cases. However, it is fair to say that to date there is no recombination model which can fully explain data from liquid rare gases. Recently, the interest in LXe as target and detector medium for dark matter searches has triggered measurements of the ionization yield of low-energy nuclear recoils in LXe, as there was no prior experimental data. The ionization yield, defined as the number of observed electrons per unit recoil energy (e^-/keV$_r$), was measured for the first time by Aprile *et al.* (2006) as a function of electric field and recoil energy. It is shown in Fig. 5.

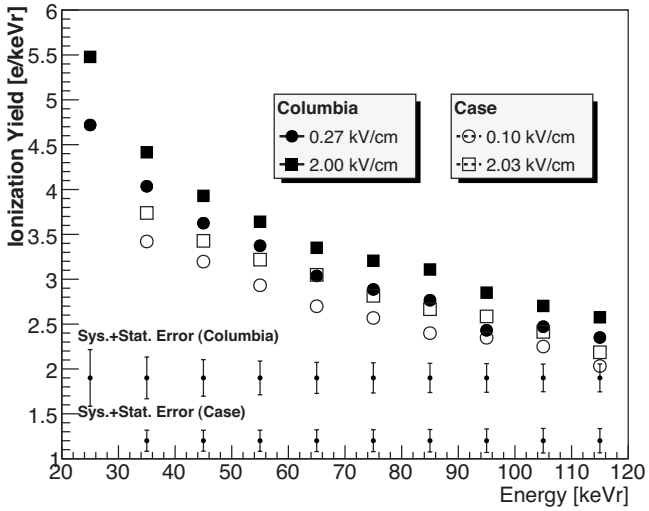

FIG. 5. Ionization yield from nuclear recoils measured with small scale two-phase xenon detectors (labeled Columbia and Case) at different electric field (Aprile *et al.*, 2006).

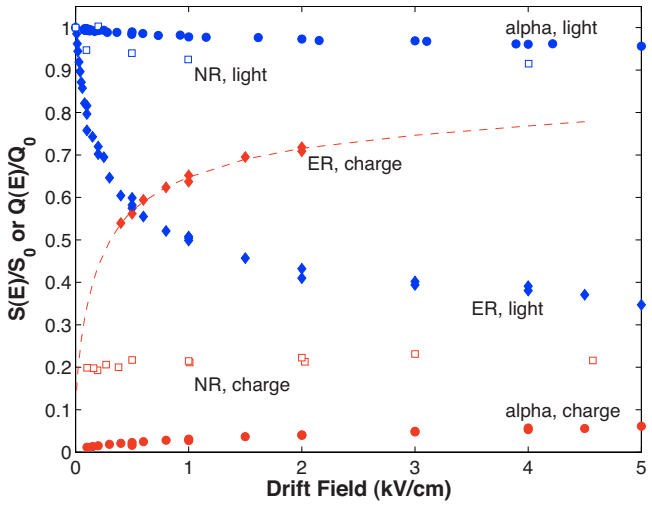

FIG. 6. (Color online) Field dependence of scintillation and ionization yield in LXe for 122 keV electron recoils (ERs), 56.5 keV_r nuclear recoils (NRs) and 5.5 MeV alphas, relative to the yield with no drift field (Aprile *et al.*, 2006).

It was expected that the stronger recombination rate along the dense track of low-energy Xe ions would result in a much smaller number of electron-ion pairs, compared to that produced by electron-type recoils of the same energy. It was not expected, however, that the number of carriers would increase with decreasing energy. Also, it was not expected that the ionization yield would be largely unaffected by the applied electric field. Figure 6, also from Aprile *et al.* (2006), shows the field dependence of both the ionization and the scintillation yields of 56.5 keV$_r$ nuclear recoils, as well as for electron recoils (122 keV gamma rays from ^{57}Co) and alpha recoils (5.5 MeV from ^{241}Am). The observed field dependence may be explained by the different rate of recombination, which depends on the electric field and also on the ionization density along the particle's track, with stronger recombination at low fields and in denser tracks. Simulations of low-energy nuclear recoils in LXe show that most energy is lost to a large number of secondary branches, each having substantially lower energy than the initial recoil. The recombination in the very sparse ends of the many secondary branches is strongly reduced at all fields. This situation is quite different from that of an alpha particle. A rough measure of the ionization density is the electronic stopping power, shown in Fig. 7 (Aprile *et al.*, 2006), for alphas, electrons, and Xe nuclei, respectively. Also shown is a recent calculation by Hitachi *et al.* (2005) of the total energy lost to electronic excitation per path length for Xe nuclei, which differs from the electronic stopping power in that it includes energy lost via electronic stopping of secondary recoils. At very low energies, the ionization yield appears to be high both for slow recoil Xe atoms and for electrons. This seems to be confirmed by the observation of very low-energy electron recoils with two-phase Xe detectors such as XENON10 (Angle *et al.*, 2008b).

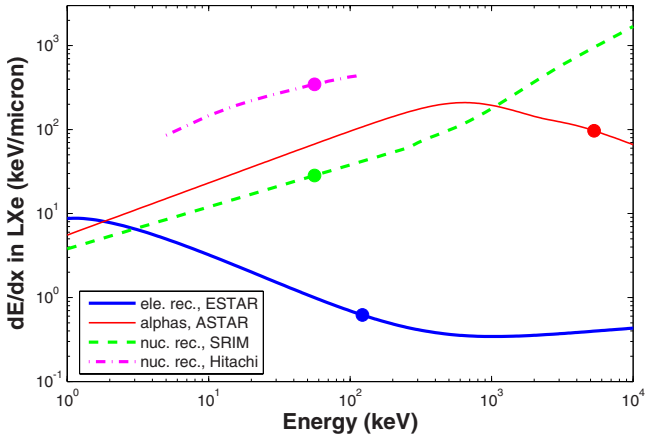

FIG. 7. (Color online) Predicted electronic stopping power dE/dx for different particles in LXe, based on various references. The circles refer to the particle energies discussed by Aprile *et al.*, 2006.

2. Fano limit of energy resolution

In 1947, Fano (1947) demonstrated that the standard deviation δ in the fluctuation of electron-ion pairs produced by an ionizing particle when all its energy is absorbed in a stopping material is not given by Poisson statistics but by

$$\delta^2 = \langle (N - N_i)^2 \rangle = F \times N_i, \tag{4}$$

where F is a constant less than 1, known as the Fano factor, and depends on the stopping material. When $F = 1$, the distribution is Poisson-like. The calculation of the Fano factor for LXe and other liquid rare gases was carried out by Doke (1980), in the optical approximation. With the known Fano factor and W value, the ultimate energy resolution of a LXe detector is given by

$$\Delta E(\text{keV}) = 2.35\sqrt{FW(\text{eV})E(\text{MeV})}, \tag{5}$$

where ΔE is the energy resolution, expressed as full width at half maximum [(FWHM): keV], and E is the energy of the ionizing radiation, in MeV. This energy resolution is often called the Fano limit of the energy resolution. Table III shows F and FW for electrons or

TABLE III. Calculated Fano factor F and FW in gaseous state and liquid states.

Material	Ar	Kr	Xe
Gas			
F	0.16[a]	0.17[b]	0.15[c]
FW (eV)	4.22	4.11	3.30
Liquid			
F	0.116[d]	0.070[d]	0.059[d]
FW (eV)	2.74	1.29	0.92

[a]Alkhazov (1972).
[b]Policarpo *et al.* (1974).
[c]de Lima *et al.* (1982).
[d]Doke *et al.* (1976).

gamma rays in LAr, LKr, and LXe (Alkhazov, 1972; Policarpo *et al.*, 1974; Doke *et al.*, 1976; de Lima *et al.*, 1982).

The Fano limit of the resolution of LXe, which is comparable to that measured with a Ge or Si detector (Doke, 1969; Owen, Fraser, and MacCarthy, 2002), has however not yet been achieved. In fact, the best energy resolution measured with a LXe ionization chamber is even worse than the Poisson limit, with the value of 30 keV for ^{207}Bi 554 keV gamma rays, measured at the highest field of 17 kV/cm (Takahashi *et al.*, 1975; Doke, 1980). Recently, a similar value was measured (Aprile *et al.*, 2006) at a field of 1 kV/cm, using the summed signals of ionization and scintillation measured simultaneously.

3. Experimental energy resolution

Large fluctuations in the number of such δ rays are considered to be the main contribution to the spread in energy resolution, as proposed by Egorov *et al.* (1982). Thomas, Imel, and Biller (1988) attempted to explain the experimental energy resolution measured from the ionization signal with a recombination model between electrons and ions produced along δ-ray tracks. Aprile, Mukherjee, and Suzuki (1991a) also attempted to explain their experimentally obtained energy resolution on the basis of the recombination model (see Fig. 4), while Obodovsky, Ospanov, and Pokachalov, presented the concept of dual W value in LXe, one for high-energy electrons and one for x rays or electrons with lower energy (Obodovsky, Ospanov, and Pokachalov, 2003). The conclusion that recombination is the primary reason for the poor energy resolution measured with pure LXe contradicts, however, the measured improvement of the energy resolution in LXe doped with photoionizing molecules, as discussed by Shibamura *et al.* (1995). The energy resolution of compressed Xe gas measured by Bolotnikov and Ramsey (1997) also does not support the recombination model since the resolution improves at lower gas density without an increase in collected charge. Figure 8 shows the density dependence of the energy resolution (% FWHM) measured for 662 keV γ rays. The resolution improves when reducing the density from 1.4 to 0.5 g/cm^3, where it is close to the Fano limit.

To date the reasons for the discrepancy between the experimental and theoretical energy resolution of LXe and other liquid rare gases remain unclear, pointing to the need for more data to reach a complete understanding of the ionization process in liquid rare gases.

4. Drift velocity of electrons and ions

LXe has a distinct band structure which consists of a conduction band and a valence band. Electrons are excited to the conduction band from the valence band by high-energy radiation and become free electrons. As a result, holes are formed in the top of the valence band. The motion of these carriers under an external electric field has been studied as a function of field strength, concentration of impurities in the liquid, and liquid temperature (Pack, Voshhall, and Phelps, 1962; Miller, Howe, and Spear, 1968; Yoshino, Spwada, and Schmidt, 1976; Gushchin, Kinglov, and Obodovski, 1982). Figure 9 (Pack, Voshhall, and Phelps, 1962; Miller, Howe, and Spear, 1968; Yoshino, Spwada, and Schmidt, 1976) shows the dependence of the electron drift velocity on the applied electric field in liquid and gaseous argon and xenon.

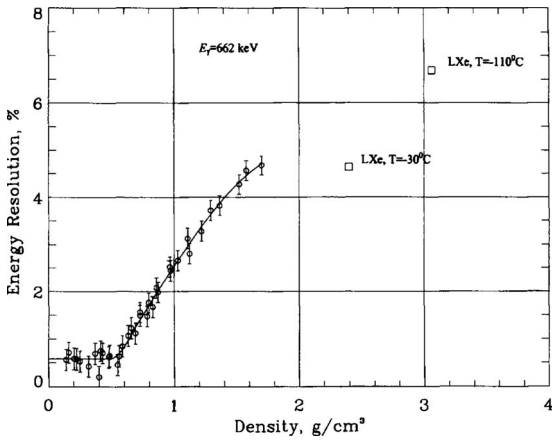

FIG. 8. Density dependence of the energy resolution (% FWHM) measured for 662 keV γ rays (Bolotnikov and Ramsey, 1997).

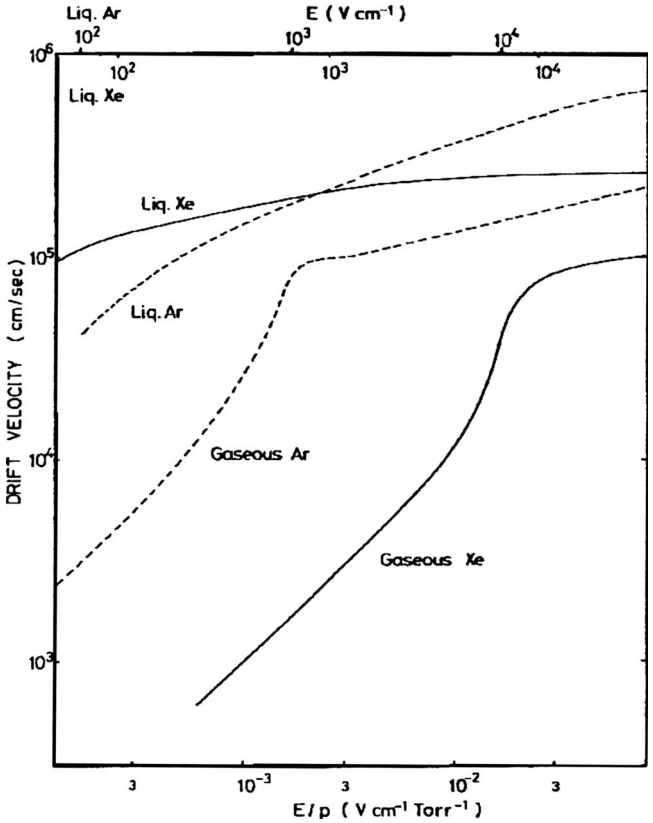

FIG. 9. Electron drift velocity in gaseous and liquid xenon and argon, as a function of reduced electric field (Pack, Voshhall, and Phelps, 1962; Miller, Howe, and Spear, 1968; Yoshino, Spwada, and Schmidt, 1976).

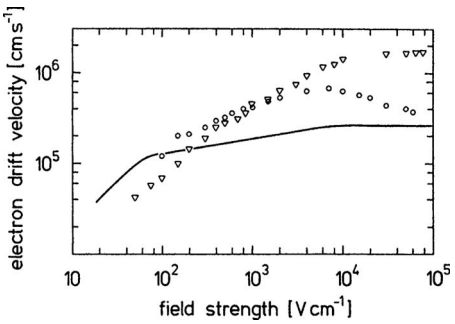

FIG. 10. Influence of butane on the electron drift velocity in liquid xenon. Butane (○, 0.09%), (△, 1.4%), and solid line: pure xenon (Yoshino, Spwada, and Schmidt, 1976).

At low fields, the electron drift velocity v_d is almost proportional to the field strength E, with the electron mobility μ as the proportionality constant ($v_d = \mu E$). The electron mobility in LXe is about 2000 cm^2 V^{-1} s^{-1}, which is near the mobility of electrons in silicon. At high fields, the electron drift velocity saturates (becomes independent of electric field strength). Figure 9 also shows that the drift velocity of electrons in LAr and LXe is much higher than the velocity in the corresponding gas phase. Specifically, the difference is more marked in LXe.

The drift velocity of electrons in LXe increases by doping organic materials into the pure liquid, as it is also found in LAr (Shibamura *et al.*, 1975). Collisions with the organic molecules cause this effect by reducing the average excitation energy of the electrons. Figure 10 shows one example involving LXe doped with butane (Yoshino, Spwada, and Schmidt, 1976). However, pure LXe is preferred as a detector medium because its purification is less difficult than the purification of organic molecules.

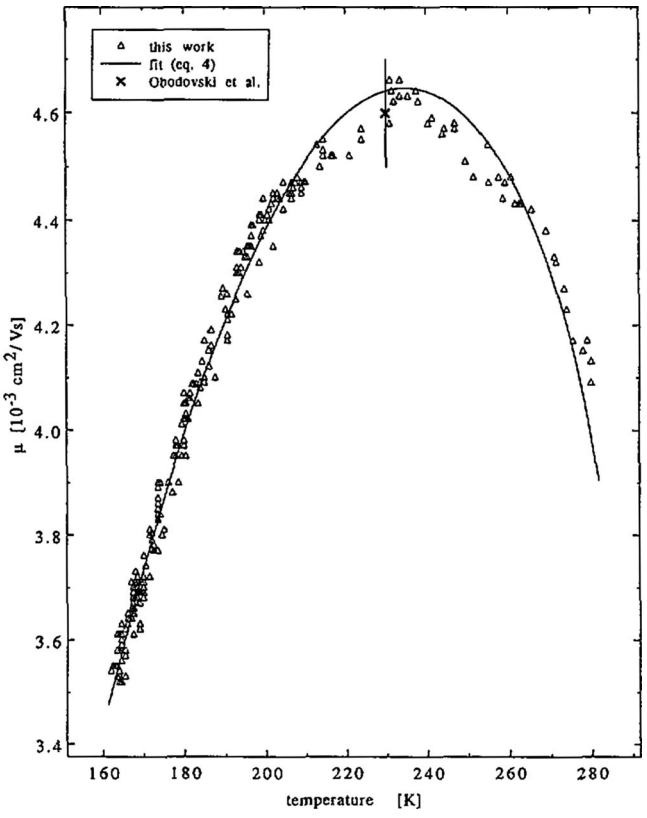

FIG. 11. Mobility of positive holes in liquid xenon as a function of temperature (Hilt and Schmidt, 1994).

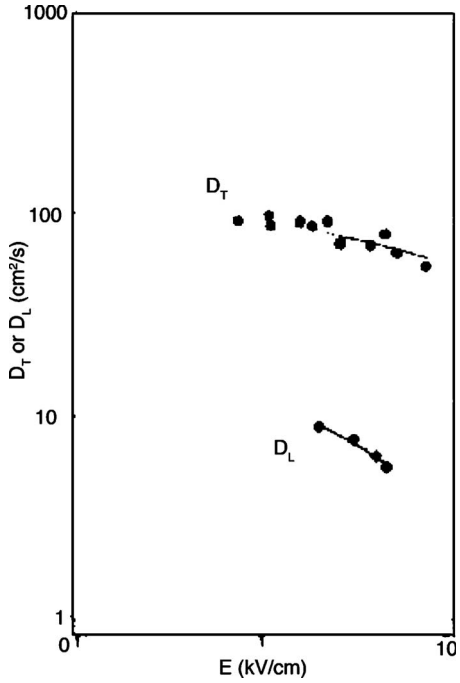

FIG. 12. Transverse and longitudinal diffusion coefficients for electrons in LXe as a function of electric field (Doke, 1980; Shibamura *et al.*, 2009).

The electron drift velocity in LXe depends slightly on the temperature of the liquid and is almost inversely proportional to the liquid temperature with a rate of about 0.5%/°C (Masuda, Doke, and Takahashi, 1981). Aprile, Mukherjee, and Suzuki (1991c) measured the electron velocity at the relatively high temperature of 195 K, from which a zero-field mobility of 4230 ± 400 cm^2 V^{-1} s^{-1} was obtained.

In LXe, positive carriers are holes, with a mobility that is several orders of magnitude less than the above-mentioned electron mobility. Its temperature dependence is shown in Fig. 11 (Hilt and Schmidt, 1994).

5. Electron diffusion

The spread of the electron cloud due to drift in an electric field is determined by the diffusion rate. This spread determines the intrinsic limit to the position resolution of a LXe detector operated in the time projection mode discussed in Sec. III.D. The electron diffusion coefficient depends on the direction of the electric field. Specifically, the diffusion coefficient D_L in the electric field direction is different from that in the direction transverse to the drift field D_r. The former is much smaller than the latter. The experimental results on these diffusion coefficients for LXe are shown in Fig. 12

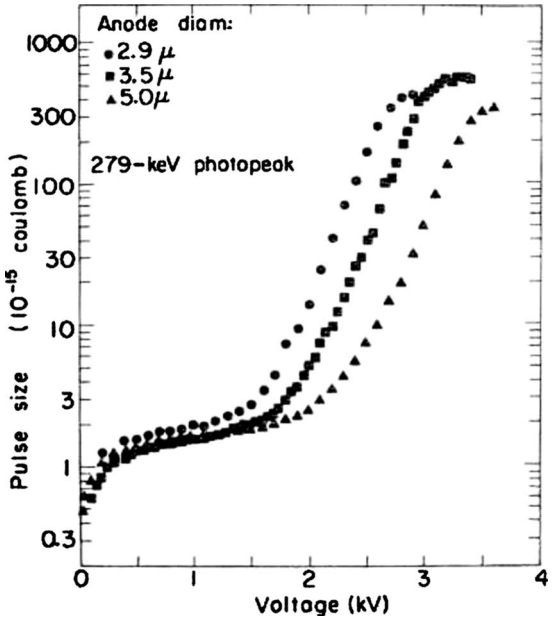

FIG. 13. Pulse height of 279 keV photopeak as a function of voltage for 2.9-, 3.5-, and 5.0-μm-diameter anode wires (Derenzo *et al.*, 1974).

(Doke, 1980; Shibamura *et al.*, 2009).

The longitudinal diffusion coefficient is about 1/10 of the transverse diffusion coefficient. This is theoretically expected (Robson, 1972). The transverse spread of an electron cloud drifting over a distance d is given by

$$\sigma_{D_T} = \sqrt{D_T t_d}, \tag{6}$$

where $t_d = d/v_d$ is the electron drift time at the drift velocity v_d. This spread contributes a negligible amount to the position resolution of a LXe detector even over a long distance.

6. Electron multiplication and proportional scintillation

In LXe, under a sufficiently high electric field (higher than 10^6 V/cm) a phenomenon known as electron multiplication (or avalanche) occurs. The first observation of this process was made by the Berkeley group (Muller *et al.*, 1971); this group later quantitatively measured the electron avalanche (Derenzo *et al.*, 1974). Their results were confirmed by the Grenoble and Waseda groups (Prunier, Pisarev, and Revenko, 1973). Figure 13 shows the variation in the gain of multiplication as a function of applied voltage to an anode wire of 2.9, 3.5, or 5.0 μm in diameter in a cylindrical counter (Derenzo *et al.*, 1974). The maximum gain measured in these cylindrical counters is a factor of several hundred and the energy resolution deteriorates with an increase in gain.

Another process occurring in LXe, with an electric field lower than the threshold for electron avalanche, is photon multiplication, also known as "proportional scintillation." The process was first observed by the Saclay group (Lansiart *et al.*, 1976) and systematically investigated by the Waseda group. In Fig. 14 (Masuda *et al.*, 1979), the solid lines show the variation of the relative photon yield as a function of applied voltage to anode wires of different diameters. The dotted lines show the variation in charge gain as a function of applied voltage to the anode wires.

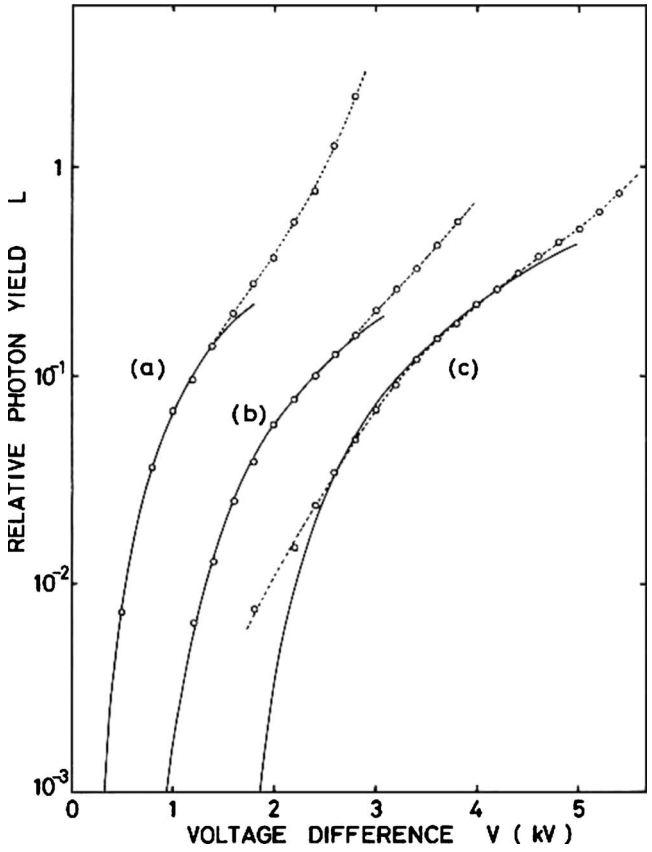

FIG. 14. Relative photon yield of proportional scintillation and charge gain as a function of applied voltage to anode wires of different diameter. Solid lines are results of the fit by Derenzo *et al.* (1974) to the data points in the region of the ionization chamber mode: (a) for 4-μm-diameter wire, (b) for 10 μm, and (c) for 20 μm (Masuda *et al.*, 1979).

The measured energy spectrum does not deteriorate with applied voltage as long as the counter is operated below electron multiplication. The maximum photon gain for 20-μm-diameter wire at 5 kV is estimated to be about 5 photons per electron (Doke, 1982).

7. Electron attachment to impurities

For stable observation of ionization signals with high ionization yield, the concentration of electronegative impurities in LXe has to be below the 1 part per billion (ppb) level of O_2 equivalent substances. The reaction of an electron with an impurity S leads to the formation of a negative ion,

$$e + S \rightarrow S^-, \tag{7}$$

and the decrease in the electron concentration $[e]$ is given as

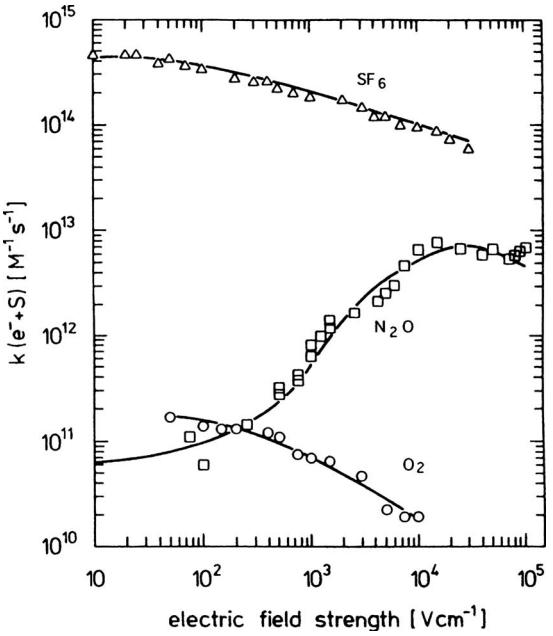

FIG. 15. Rate constant for the attachment of electrons in liquid xenon (T=167 K) to several solutes: (△) SF_6, (□) N_2O, and (○) O_2 (Bakale, Sowadaand, and Schmidt, 1976).

$$d[e]/dt = -k_S[e][S], \tag{8}$$

where $[S]$ is the concentration of impurity given in mol/l and k_S is the attachment rate constant in l/(mol s). The temporal variation of the electron concentration $[e]$ is then given as

$$[e(t)] = [e(0)]\exp(-k_S[S]t) \tag{9}$$

and the time

$$\tau = (k_S[S])^{-1} \tag{10}$$

is called the electron lifetime. Usually, in the detection of impurities in a sample of LXe, both k_S and $[S]$ are unknown. One measures an exponential decay in time of the electron concentration, through the measurement of the direct current induced by the drift of the electrons or its integrated value of collected charge. Attachment leads to a decrease in the current with time or to a reduction in the collected charge. Instead of quoting τ, one often quotes the attenuation length of the electrons,

$$\lambda_{att} = \mu E \tau, \tag{11}$$

where μ is the electron mobility and E is the field.

Two types of electronegative impurities are normally found in LXe: those with an attachment cross section that decreases with increasing electric field and those with a cross section that increases with increasing field. Figure 15 shows the attachment cross section as a function of applied electric field for some electronegative gases, SF_6, N_2O, and O_2 (Bakale, Sowadaand, and Schmidt, 1976). Here SF_6 and O_2 correspond to the first type of impurity and N_2O to the second.

A concentration of 1 ppb (oxygen equivalent) corresponds to an attenuation length of 1 m. Several methods

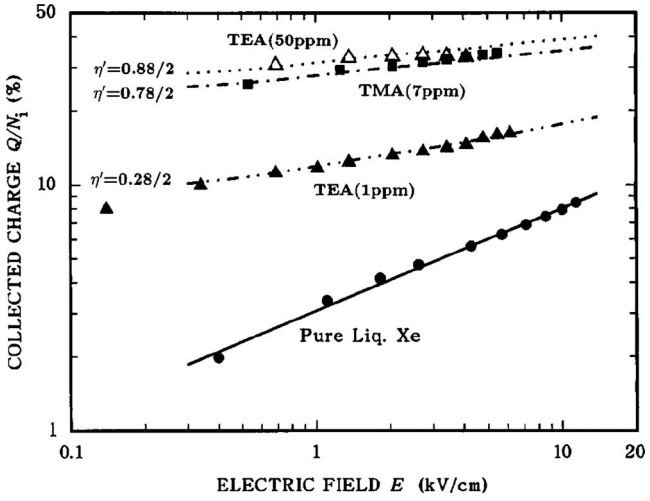

FIG. 16. Collected charge Q/N_i, where N_i is the total ionization (number of electrons), for P_o α particles as a function of applied electric field, in pure liquid xenon (●), and in liquid xenon doped with TMA (■, 7 ppm) and TEA (▲, 1 ppm; △, 50 ppm). The curves give the calculated results from Eq. (3) in Hitachi *et al.*, 1997.

have been developed for the removal of impurities, and the choice of the most appropriate method depends not only on the volume of liquid to be purified but also on the application. They include adsorption and chemical reaction methods, filtration, separation, electrical discharges, and irradiation with gamma rays. Outgassing from the liquid containment vessel and other detector's materials contribute to the total concentration of electron-attaching impurities in the liquid, through a diffusion process. The outgassing rates and the diffusion time scale depend on the type of material and on the surface finish. For LXe a purity at the ppb level has been achieved using hot metal getters and/or cold molecular sieves. For details of purification methods and different purification systems used to date with LXe detectors see Prunier, Pisarev, and Revenko (1973); Masuda *et al.* (1981); Aprile, Mukherjee, and Suzuki (1991c); Barabash and Bolozdynia (1993); Carugno *et al.* (1993); Ichige *et al.* (1993); and Angle *et al.* (2008b).

8. Photoionization

Some organic molecules have a high photosensitivity. If the dopant molecules have an ionization potential lower than the energy of the scintillation photons emitted from LXe, these photons will ionize the molecules, producing additional charge carrier pairs. This idea of increasing the ionization yield of liquid rare gases with photosensitive dopants was first proposed by Policarpo *et al.* (1982) and first observed by Anderson (1986) in LAr. For LXe, results on the increased ionization yield with appropriate photosensitive molecules were first reported by Suzuki *et al.* (1986).

Figure 16 shows the collected charge for alpha particles as a function of electric field in liquid xenon doped with triethylamine (TEA) or trimethylamine (TMA) (Hitachi *et al.*, 1997).

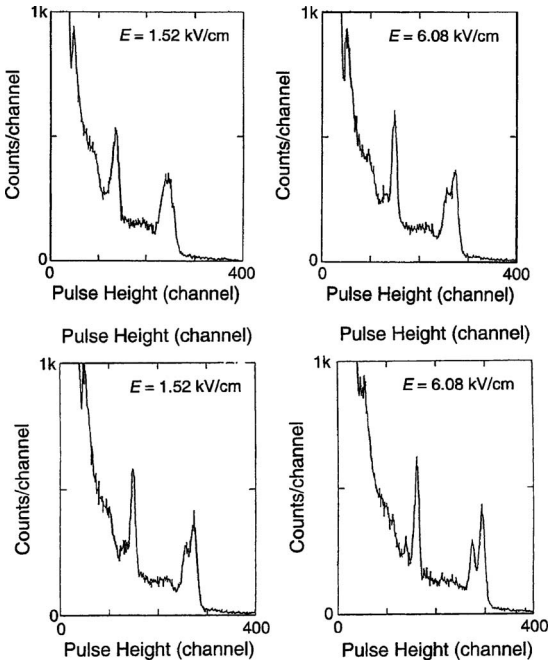

FIG. 17. Comparison between the energy spectra of ^{207}Bi internal conversion electrons and gamma rays measured from ionization: (top) in pure liquid xenon and (bottom) in TEA-doped liquid xenon (Hitachi *et al.*, 1997).

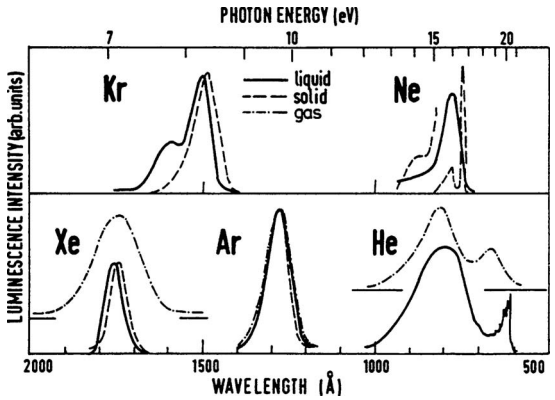

FIG. 18. Emission bands in liquid rare gases, together with solid- and gas-phase spectra (Jortner *et al.*, 1965; Schwenter, Kock, and Jortner, 1985).

As shown in Fig. 3, the collected charge in pure LXe for alpha particles is only 1–10 % of the total charge estimated from the W value, over the applied electric field of 1 to 10 kV/cm, reflecting the strong electron-ion recombination rate. However, doping liquid xenon with 1–50 ppm of TEA recovers part of the charge lost in the recombination process, and the collected charge increases to almost 40% of the total, at the maximum applied field. On the basis of these data, the quantum efficiency of photoionization of TEA in LXe is estimated to be 80%.

The photoionization effect was used to improve the energy resolution of a LXe ionization chamber irradiated with gamma rays (Ichinose *et al.*, 1992), as shown in Fig. 17. The separation of the internal conversion electron peak (976 keV) and the gamma-ray peak (1047 keV) can be seen to be much better in the TEA doped LXe when compared to pure LXe. An electric field higher than 10 kV/cm is necessary to realize the separation of the two peaks in pure LXe.

In TEA-doped LXe, photon-mediated electron multiplication also occurs at the electric field where proportional scintillation takes place (Sano *et al.*, 1989). The maximum gain of photomediated multiplication is about 200, which is almost equal to that of electron multiplication but with poorer energy resolution.

D. Scintillation process

The emission of luminescence, also called scintillation, from liquid rare gases is attributed to the decay of excited dimers (excimers, in short) to the ground state. The luminescence emission bands for Ar, Kr, Ne, and He in liquid, solid, and gas phases are shown in Fig. 18 (Jortner *et al.*, 1965; Schwenter, Kock, and Jortner, 1985). We note that the emission bands in the three phases of Xe, Ar, and Kr are almost identical. In contrast, the emission band for liquid Ne differs dramatically from that of solid Ne. For LXe, the wavelength of the scintillation photons is centered at 177.6 nm.

1. Origin of scintillation

Both direct excitation of atoms and electron-ion recombination lead to the formation of excited dimers, Xe_2^*. Thus, the origin of the vacuum ultraviolet (vuv) scintillation light in LXe is attributed to two separate processes involving excited atoms (Xe^*) and ions (Xe^+), both produced by ionizing radiation (Kubota, Hishida, and Ruan, 1978)

$$\begin{aligned} &Xe^* + Xe + Xe \rightarrow Xe_2^* + Xe, \\ &Xe_2^* \rightarrow 2Xe + h\nu, \end{aligned} \tag{12}$$

$$\begin{aligned} &Xe^+ + Xe \rightarrow Xe_2^+, \\ &Xe_2^+ + e^- \rightarrow Xe^{**} + Xe, \\ &Xe^{**} \rightarrow Xe^* + \text{heat}, \\ &Xe^* + Xe + Xe \rightarrow Xe_2^* + Xe, \\ &Xe_2^* \rightarrow 2Xe + h\nu. \end{aligned} \tag{13}$$

2. Scintillation pulse shape

The scintillation light from pure LXe has two decay components due to deexcitation of singlet and triplet states of the excited dimer Xe_2^*. Figure 19 (Hitachi *et al.*, 1983) shows the decay curves of the scintillation light for electrons, alpha particles, and fission fragments in LXe, without an electric field. The decay shapes for

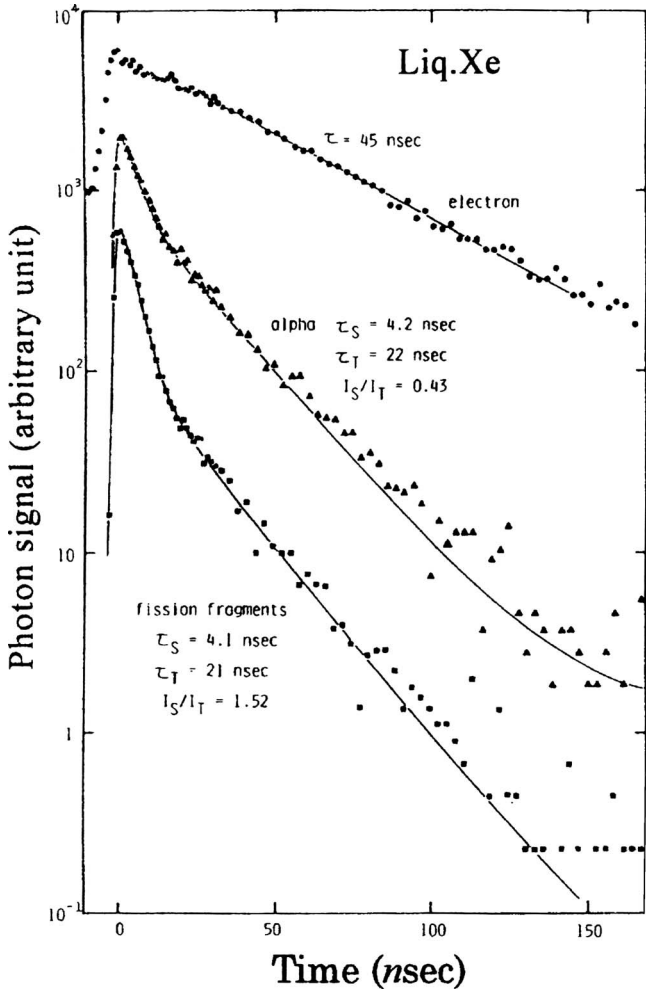

FIG. 19. Decay curves of scintillation from liquid xenon excited by electrons, α particles, and fission fragments, without an applied electric field (Kubota, Hishida, and Ruan, 1978; Hitachi *et al.*, 1983).

α particles and fission fragments have two components. The shorter decay shape is produced by the deexcitation of singlet states and the longer one from the deexcitation of triplet states. Specifically, the short and long decay times are 4.2 and 22 ns for alpha particles. For fission fragments, the values are 4.1 and 21 ns, respectively. These decay times make LXe the fastest of all liquid rare gas scintillators. While the singlet and triplet lifetimes depend only weakly on the density of excited species, the intensity ratio of singlet to triplet states is larger at higher deposited energy density.

For relativistic electrons, the scintillation has only one decay component, with a decay time of 45 ns (Kubota *et al.*, 1979; Hitachi *et al.*, 1983). Since this component disappears with an applied electric field, it is likely due to the slow recombination between electrons and ions produced by relativistic electrons. Figure 20 (Kubota, Hishida, and Ruan, 1978) shows the decay curves of LXe scintillation light, with an electric field of 4 kV/cm, with two distinct decay components. From this figure, it is estimated that the short decay time for relativistic electrons is 2.2±0.3 ns and the long decay time is 27±1 ns.

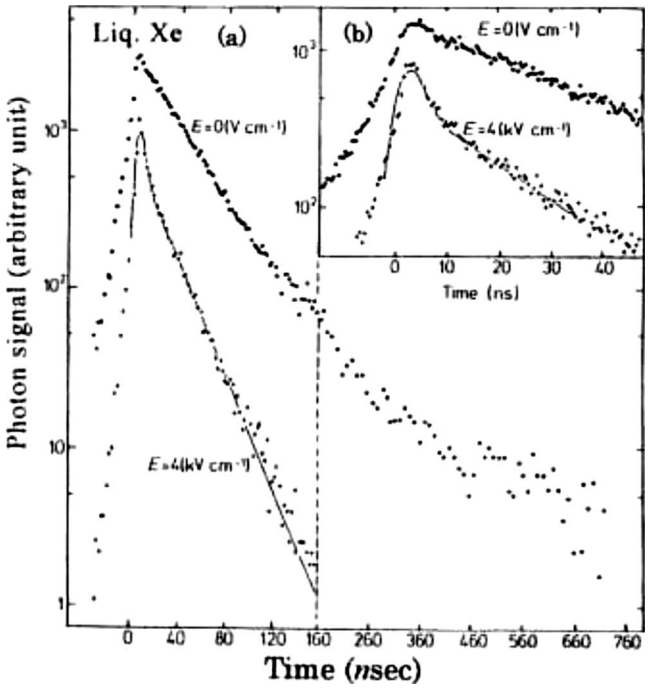

FIG. 20. Decay curves of scintillation from liquid xenon with and without an electric field of 4 kV/cm, (a) over a long time scale and (b) a short time scale. Note the change in time scale at 160 ns in (a) (Kubota, Hishida, and Ruan, 1978).

The difference in the scintillation pulse decay shape for different types of particle in liquid rare gases can be used to effectively discriminate these particles. Pulse shape discrimination (PSD) is, however, difficult for LXe given the small time separation of the two decay components. On the other hand, for LAr, the large time separation of the singlet and triplet components with values of 5.0 and 1590 ns, respectively, makes PSD very effective (Hitachi *et al.*, 1983; Lippincott *et al.*, 2008).

3. Scintillation yield

If E is the energy deposited by the ionizing radiation, the maximum scintillation yield is given as E/W_{ph}, where W_{ph} is the average energy required for the production of a single photon. Assuming the absence of photon reduction (or quenching) processes, W_{ph} can be expressed as (Doke *et al.*, 2002)

$$W_{\mathrm{ph}} = W/(1 + N_{\mathrm{ex}}/N_i), \tag{14}$$

where W is the average energy required to produce an electron-ion pair. N_{ex} and N_i are the numbers of excitons and electron-ion pairs, respectively, produced by the ionizing radiation.

The scintillation yield depends on the linear energy transfer (LET), that is, the density of electron-ion pairs produced along the track of a particle, because the recombination probability between electrons and ions increases with the density of electron-ion pairs. Figure 21 (Doke *et al.*, 1988, 2002) shows such an LET dependence of the scintillation yield in LAr. As seen from the figure, the scintillation yield stays at a maximum value over an

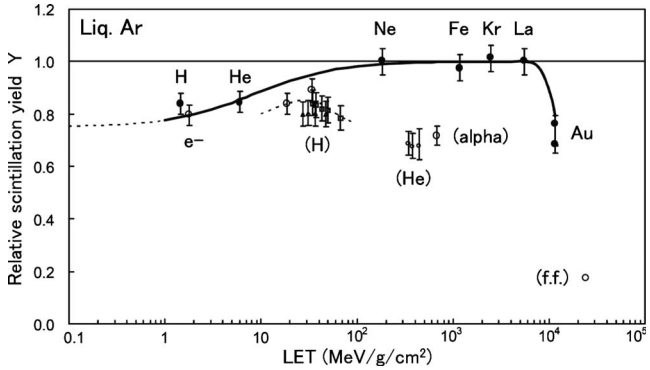

FIG. 21. LET dependence of scintillation yield Y in liquid argon (Doke *et al.*, 1988, 2002). Solid circles show the yields for relativistic particles. Nonrelativistic particles are represented by open circles. Open squares and triangles show the yields for nonrelativistic protons, whereas small open circles show those for nonrelativistic helium ions.

extended region of the LET. In these experiments involving relativistic heavy ions, the scintillation signals were simultaneously observed with the ionization signals. The sum of ionization and scintillation signals, properly normalized (Crawford *et al.*, 1987) and divided by $N_{ex}+N_i$, gives a completely flat LET dependence, except for alpha particles, fission fragments, and relativistic Au ions as shown in Fig. 22 (Doke *et al.*, 1988, 2002). It should be noted that the flat level in Fig. 21 corresponds to the maximum limit of the sum signals. In the low LET region, the scintillation yield gradually decreases with decreasing LET, and in the high LET region, the scintillation yield decreases as the LET increases. The former behavior is caused by the so-called "escape electrons," namely, those electrons that do not recombine with parent ions for an extended period of time (on the order of a few ms), in the absence of electric field. The latter behavior is due to the so-called quenching effect. The observed behavior of nonrelativistic protons and helium ions is explained by a combination of both effects (escape electrons and quenching).

The LET dependence of scintillation yield in LXe is shown in Fig. 23 (Tanaka *et al.*, 2001; Doke *et al.*, 2002).

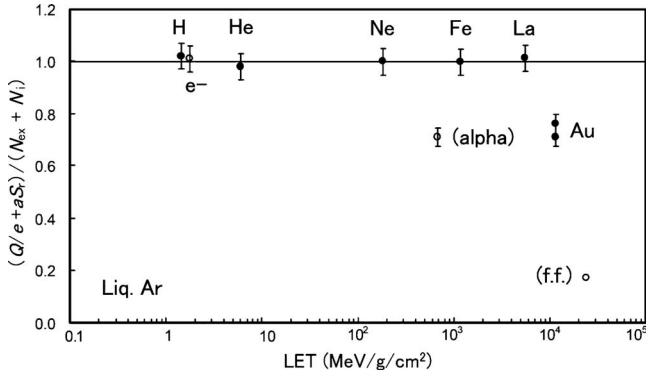

FIG. 22. LET dependence of the ratio $(Q/e+aS_r)/(N_{ex}+N_i)$ in liquid argon (Doke *et al.*, 1988, 2002). The label (f.f.) stands for fission fragments.

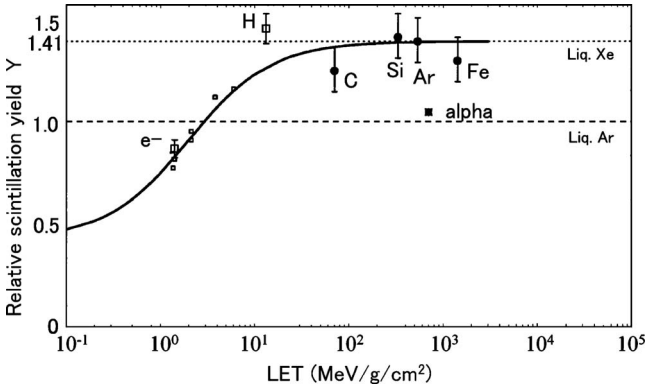

FIG. 23. LET dependence of the scintillation yield in liquid xenon for various ionizing particles (Tanaka *et al.*, 2001; Doke *et al.*, 2002).

LAr and LXe display a similar LET dependence. In the case of LXe, however, the ionization and scintillation signals were not observed simultaneously. Therefore, it is not straightforward to conclude on this basis that the flat behavior of the LET in LXe corresponds to the maximum scintillation yield. However, as discussed by Doke *et al.* (2002), this assumption is consistent with results obtained for LAr and LXe.

On the basis of these experimental results on the maximum scintillation yield measured over a wide LET region in LXe, the W_{ph} value was estimated to be 13.8±0.9 eV (Doke *et al.*, 2002). The $W_{ph}(\beta)$ value for 1 MeV electrons and $W_{ph}(\alpha)$ for α particles are both lower than the derived maximum W_{ph} because of escape electrons or scintillation quenching. Doke *et al.* (2002) estimated a value of 17.9 eV for $W_{ph}(\alpha)$ and a value of 21.6 eV for $W_{ph}(\beta)$. N_{ex}/N_i, W_{ph}, β/α, and $W_{ph}(\alpha,\beta)$ in LXe are shown in Table IV (Doke *et al.*, 2002). The same quantities are also given for LAr. Compared to all liquid rare gases, LXe has the highest scintillation light yield, similar to that of the best crystal scintillators.

4. Relative scintillation efficiency of nuclear recoils

The energy loss by nuclear collisions and the higher excitation density of nuclear recoils compared to electron recoils of the same energy are such that the scintillation light yield is different for these two types of par-

TABLE IV. Most probable values of N_{ex}/N_i, W_{ph}(max), β/α ratio, $W_{ph}(\alpha)$, and $W_{ph}(\beta)$ in liquid argon and xenon, derived from data in Figs. 21 and 23. α and β mean α particle and β ray and β/α is the ratio of scintillation yields for β ray and α particle.

Item	Liquid Ar	Liquid Xe
N_{ex}/N_i	0.21	0.13
W_{ph}(max) (eV)	19.5±1.0	13.8±0.9
β/α	1.11±0.05	$0.81^{+0.07}_{-0.13}$
$W_{ph}(\alpha)$ (eV)	27.1	17.9
$W_{ph}(\beta)$ (eV)	24.4	21.6

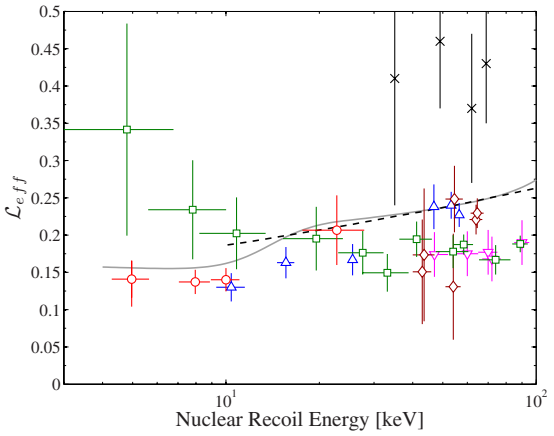

FIG. 24. (Color online) Relative scintillation efficiency of nuclear recoils in LXe (Aprile *et al.*, 2009, and references therein).

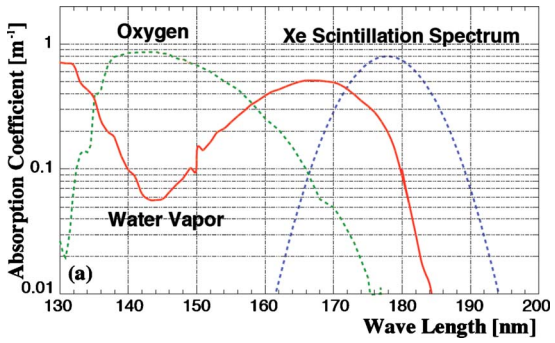

FIG. 25. (Color online) Absorption coefficient for vuv photons in 1 ppm water vapor and oxygen and superimposed Xe emission spectrum (Ozone, 2005).

ticles. Knowledge of the ratio between the two scintillation yields, called relative scintillation efficiency ($L_{\rm eff}$), is important for the determination of the sensitivity of LXe-based detectors to dark matter weakly interacting massive particles (WIMPs), which we discuss in Sec. IV.B. The Xe nuclear recoils which result from WIMPs (or neutrons) scattering off Xe nuclei have energies in the range of a few keV up to several tens of keV. Several measurements of $L_{\rm eff}$ have been carried out (Arneodo *et al.*, 2000; Bernabei *et al.*, 2001; Akimov *et al.*, 2002; Aprile *et al.*, 2005; Chepel *et al.*, 2006) with the most recent one extending down to 5 keV_r nuclear recoil energy (Aprile *et al.*, 2009). The relative scintillation efficiency for recoils of this energy is 14%, constant around this value up to 10 keV_r. For higher energy recoils, the value is on average about 19%. Figure 24 summarizes all the measurements to date. A fit through the data and the predicted curve by Hitachi *et al.* (2005) are also shown as solid and dotted lines, respectively.

Compared to the scintillation yield of electron or alpha particle excitation, the scintillation yield of nuclear recoil excitation is significantly reduced due to nuclear quenching (Lindhard, 1963). Hitachi estimated the additional loss in scintillation yield that results from the higher excitation density of nuclear recoils. Rapid recombination in LXe under high LET excitation (Hitachi *et al.*, 1983, 1992) provides a mechanism for reducing the scintillation yield of nuclear recoils in addition to that of nuclear quenching treated by Lindhard (1963). In order to estimate the total scintillation yield, Hitachi *et al.* (1992, 2005) considered biexcitonic collisions, or collisions between two "free" excitons that emit an electron with a kinetic energy close to the difference between twice the excitation energy $E_{\rm ex}$ and the band-gap energy E_g (i.e., $2E_{\rm ex}-E_g$):

$$\mathrm{Xe}^* + \mathrm{Xe}^* \rightarrow \mathrm{Xe} + \mathrm{Xe}^+ + e^-. \tag{15}$$

The electron then loses its kinetic energy very rapidly before recombination. This process reduces the number of excitons available for vuv photons since it requires two excitons to eventually produce one photon. Hitachi therefore considered this to be the main mechanism responsible for the reduction of the total scintillation yield in LXe under irradiation by nuclear recoils. The Hitachi model (Hitachi *et al.*, 1992, 2005), however, does not hold at energies below 10 keV_r.

5. Absorption length and Rayleigh scattering

Impurities dissolved in LXe may absorb the vuv photons, reducing the observed scintillation light yield. Light attenuation can be described by

$$I(x) = I(0)\exp(-x/\lambda_{\rm att}), \tag{16}$$

where $\lambda_{\rm att}$ is the photon attenuation length, which consists of two separate components, the absorption length $\lambda_{\rm abs}$, describing true absorption and loss of photons by impurities, and the scattering length $\lambda_{\rm sca}$, representing elastic scattering of photons without any loss. The latter is dominated by Rayleigh scattering. The two are related by

$$1/\lambda_{\rm att} = 1/\lambda_{\rm abs} + 1/\lambda_{\rm sca}. \tag{17}$$

The attenuation length can be measured after removing the contribution from Rayleigh scattering. The Rayleigh scattering length is theoretically estimated to be about 30 cm (Seidel, Lanou, and Yao, 2002; Baldini *et al.*, 2005) which roughly agrees with the $\lambda_{\rm sca}$ experimentally obtained (Braem *et al.*, 1992; Chepel *et al.*, 1994; Ishida *et al.*, 1997; Solovov *et al.*, 2004).

The wavelength of scintillation light from liquid argon or krypton doped with xenon is different from that from pure liquid argon or krypton. Accordingly, the measurement of the attenuation length in liquid argon or krypton doped with xenon should show the wavelength dependency of the attenuation length due to Rayleigh scattering. The attenuation length due to Rayleigh scattering calculated for liquid Ar+Xe (3%) and liquid Kr +Xe (3%) roughly agreed with the results obtained experimentally (Ishida *et al.*, 1997).

The most serious impurity for the vuv light of LXe is water vapor, which is largely contributed by the outgassing of the liquid containment vessel and other detector materials placed inside the liquid. Figure 25 shows the absorption coefficient for vuv photons in 1 ppm water

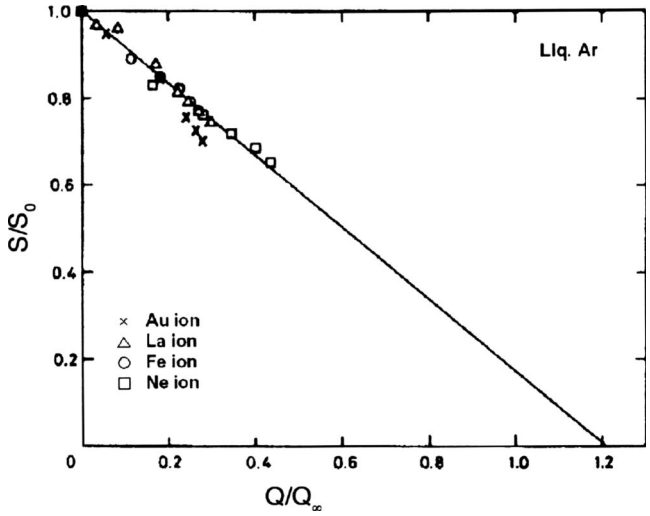

FIG. 26. Anticorrelation between scintillation intensity and collected charge in liquid argon for relativistic Ne ions (□), Fe ions (○), La ions (△), and Au ions (×). The solid line is the theoretically estimated relation (Masuda *et al.*, 1989).

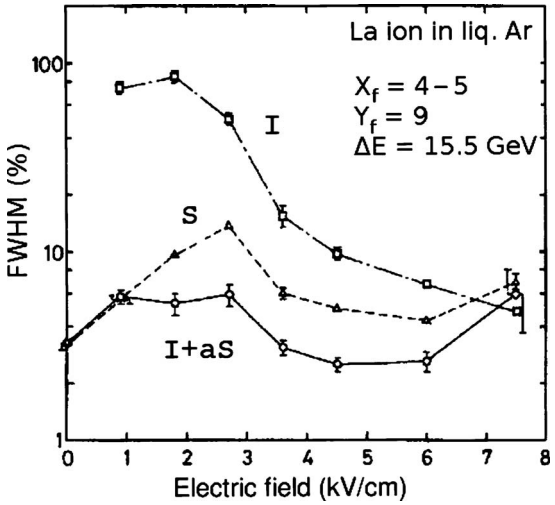

FIG. 27. Energy resolution (FWHM) of La ions in LAr as a function of the electric field, measured separately from scintillation, ionization, and their sum (Crawford *et al.*, 1987).

vapor and oxygen. The absorption spectra of water and oxygen largely overlap with the xenon scintillation spectrum [see Signorelli (2004) and Ozone (2005), and references therein]. Within the R&D program for the development of the large LXe scintillation calorimeter for the MEG experiment (PSI, 1999), an absorption length longer than 100 cm at 90% confidence level was achieved (Baldini *et al.*, 2005), corresponding to less than 100 ppb concentration of water vapor. This work has been useful for other experimenters in the field, bringing out the awareness of the careful detector's preparation to minimize absorption by water vapor.

6. Refractive index for scintillation light

To simulate the number of photons collected in a LXe detector, knowledge of the refraction index in the region of the Xe vuv light emission is also relevant. Measurements of this quantity range from 1.54 to 1.69 (Subtil *et al.*, 1987; Barkov *et al.*, 1996; Solovov *et al.*, 2004).

E. Correlation between ionization and scintillation

As mentioned, in heavy liquid rare gases the two signals of ionization and scintillation can be observed simultaneously. The amplitude of the two signals are complementary and strongly anticorrelated. In the LET region in which the scintillation yield is maximum (see Figs. 21–23), both signals are perfectly anticorrelated.

1. Correlation in liquid argon for relativistic heavy ions

The simultaneous measurement of ionization and scintillation signals due to relativistic heavy ions has not been carried out for LXe. Yet, measurements of the correlation between ionization and scintillation for relativistic heavy ions in LAr (Masuda *et al.*, 1989) provide a good example (see Fig. 26). The scintillation intensity S, normalized to the scintillation intensity at zero-electric field S_0, is shown as a function of the collected charge Q normalized to the charge expected for infinite electric field Q_∞. The figure shows that the correlation between S/S_0 and Q/Q_∞ is perfectly complementary for relativistic Ne, Fe, and La ions, whose scintillation yields are 100%. On the other hand, for relativistic Au ions, the data deviate from the straight line corresponding to a perfectly complementary relation because the scintillation yield of relativistic Au ions is not 100% due to quenching.

Figure 27 shows the energy resolution of the ionization signal, the scintillation signal, as well as from the two signals combined, measured for relativistic La ions in the above experiment. As expected, the energy resolution of the summed signals is better than that of each individual signal despite the fact that only a small fraction of the scintillation light was collected in this experiment because of the limited solid angle for photon collection and the low PMT quantum efficiency.

2. Correlation in liquid xenon for relativistic electrons

For relativistic electrons whose scintillation yield is lower than 100%, the correlation of both signals does not reflect a perfectly complementary relation. Figure 28 (Doke *et al.*, 2002) shows the correlation between charge and light signals measured for 1 MeV conversion electrons emitted from ^{207}Bi in LXe. The solid straight line indicates a perfect anticorrelation of the two signals. Only the data obtained at high electric fields are on the straight line. Recent data obtained by the Columbia University group for ^{137}Cs gamma rays show a perfect anticorrelation even at modest fields, as discussed in Sec. III.C and shown in Fig. 40. These measurements show that the anticorrelation of ionization and scintillation in LXe reduces the fluctuation in the summed signal to a lower level than that in each individual signal and results in a better energy resolution.

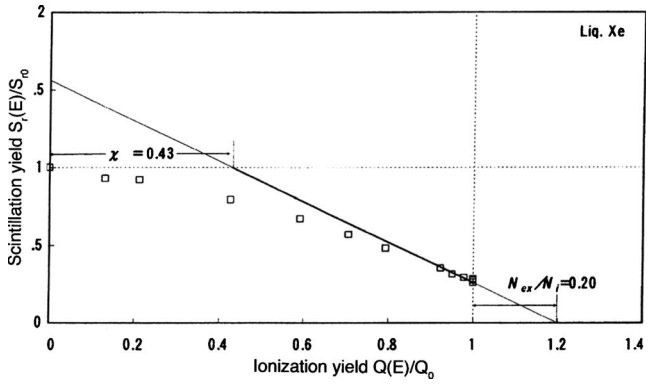

FIG. 28. Relation between S_r/S_{r_0} and Q/Q_0 in liquid xenon (Doke *et al.*, 2002). The straight line indicates the perfect anticorrelation of the charge and light signal. χ is the ratio of number of escaping electrons at zero electric field over the numbers of ion pairs produced by the ionizing radiation.

All fundamental parameters of LXe as detector medium described in this section are summarized in Table V.

TABLE V. Properties of liquid xenon as detector medium.

Item	Values
Ionization properties	
W value	15.6±0.3 eV
Drift velocity and hole mobility	
Electron mobility	2000±200 $cm^2/V\,s$
Saturated drift velocity of electrons at an electric field of 3–10 kV/cm	$2.6\times10^5\pm10\%$ cm/s
Hole mobility	3.6×10^{-3} $cm^2/V\,s$
Diffusion coefficient of electrons	
Transverse diffusion coefficient (D_T)	
at an electric field of 1 kV/cm	80 $cm^2\,s^{-1}$
at electric field of 10 kV/cm	50 $cm^2\,s^{-1}$
Longitudinal diffusion coefficient (D_L)	$0.1D_T$
Multiplications	
Electron multiplication	
Threshold electric field	$(1–2)\times10^6$ V/cm
Maximum gain	400
Photon multiplication	
Threshold electric field	$(4–7)\times10^6$ V/cm
Scintillation properties	
Wavelength	177.6 nm
W_{ph} value	See Table IV
Decay time constants	
from singlet state	
for electrons	2.2±0.3 ns
for alpha particles	4.3±0.6 ns
from triplet state	
for electrons	27±1 ns
for alpha particles	22±1.5 ns
due to recombination	
for electrons	45 ns
Radiation length	2.87 cm
Moliere radius	4.1 cm
Refraction index	1.54–1.69
Attenuation length due to	
Rayleigh scattering (theoretical)	30 cm
Rayleigh scattering (experimental)	29–50 cm

III. LIQUID XENON DETECTOR TYPES

Among liquid rare gases suitable for radiation detection, liquid xenon (LXe) has the highest atomic number and density at a modest boiling temperature, the best ionization, and scintillation yields, as well as the highest electron mobility and lowest diffusion. All these are important features for a practical detector. The ionization and scintillation can be detected simultaneously to provide a precise measurement of the energy, position, and time of an event occurring in the sensitive liquid volume. Most of the early LXe detectors have exploited only the ionization process due to the difficulty of efficiently detecting the vuv scintillation. In the mid-1990s, we initiated a R&D program with Hamamatsu Photonics Co., aimed at the development of new vuv sensitive photomultipliers (PMTs), which would operate immersed in LXe, withstanding up to 5 bar overpressure. This development, together with the more recent development of large area avalanche photodiodes (LAAPDs) (Solovov *et al.*, 2002c; Ni *et al.*, 2005), also able to work in LXe with high sensitivity in the vuv, has had a dramatic impact on the evolution of LXe detectors, leading to an explosion of new detectors exploiting the benefits of the double signature of charge and light in LXe. In this section we review the basic operating principle and characteristics of the most common classes of LXe detectors. The applications which use these detectors in specific experiments are covered in the last section.

A. Ionization mode

We consider first a LXe detector sensitive only to the ionization process. The passage of ionizing radiation depositing an energy E_0 in the liquid results in a number of electron-ion pairs N_i given as

$$N_i = E_0/W, \tag{18}$$

where W is the W value in LXe, defined previously.

Measurement of the total charge associated with an ionizing event N_i is referred to as the ionization mode and is usually used only for electrons, γ rays, or minimum ionizing particles. For heavily ionizing particles, such as alphas, the electron-ion recombination rate is too high to allow a complete charge collection, as shown in Fig. 3.

The most straightforward detector to measure N_i is a gridded ionization chamber, a device consisting of a cathode and an anode, separated by a third electrode, called a Frish grid (Frish, 1945). The cathode is kept at a

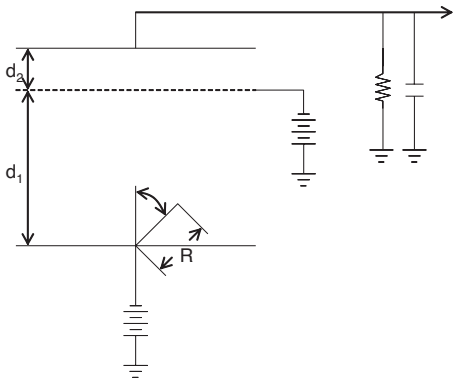

FIG. 29. Schematic of a gridded ionization chamber. d_1 is the drift gap between the cathode (on the bottom) and the Frish grid, d_2 is the field region between the Frish grid and the anode (on the top).

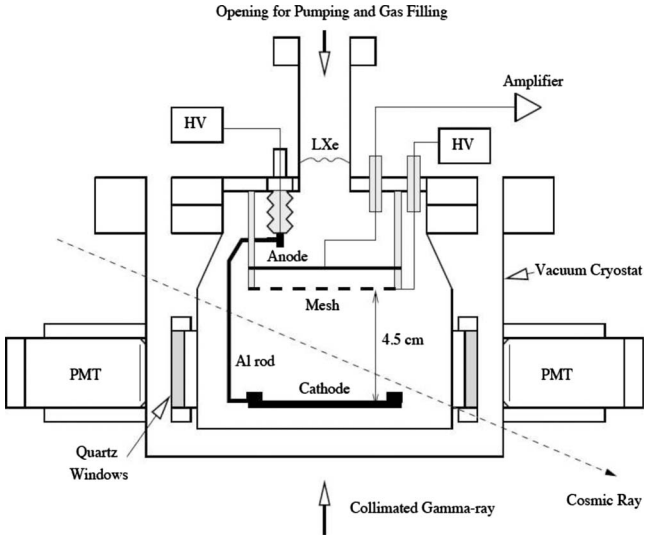

FIG. 30. Schematic of a 3.5 l LXe gridded ionization chamber, triggered by the scintillation light (Aprile *et al.*, 2002).

more negative potential with respect to the anode, and the grid is at an intermediate potential. Figure 29 shows the schematic of a gridded parallel plate ionization chamber. The ionizing particle track of length R is oriented at an angle θ with respect to the electric field created between cathode and grid. The electric field separates the carriers, with the electrons drifting towards the anode, and the ions towards the cathode. The purpose of the grid is twofold: (1) it allows the electron signal to be induced only after they cross the grid and (2) it shields the anode from the slow motion of the positive ions. Thus the signal on the anode is derived only from the drift of the electrons, with an amplitude which is proportional to number of electron-ion pairs, but independent of the position where they were created (Knoll, 2000). Calculation of the shielding inefficiency of a Frish grid and the condition for maximum electron transmission has been carried out by Bunemann *et al.* (1949).

To measure the X and Y coordinates of the ionizing event, one can use the signal induced on two orthogonal planes of wires between the Frish grid and the anode. In this case, the Frish grid serves the additional purpose of focusing the electric field lines and maximizing electron transmission. This is the approach used for the time projection chamber (TPC) of the LXeGRIT Compton telescope (Aprile *et al.*, 2000), discussed in Sec. III.D.

Many of the results obtained on ionization yield, energy resolution of electrons and gamma rays in LXe have been obtained with gridded ionization chambers, with drift gaps of several millimeters [see, e.g., Takahashi *et al.* (1975) and Aprile, Mukherjee, and Suzuki (1991a)]. Figure 30 shows a larger gridded ionization chamber, with a volume of 3.5 l, used to measure gamma rays in the MeV energy range (Aprile *et al.*, 2002). The drift gap of 4.5 cm is viewed by two vuv-sensitive PMTs, coupled to the LXe vessel by quartz windows, to detect the fast scintillation signal as event trigger.

Another method for eliminating the position dependence of the charge signal in an ionization chamber was proposed by Luke (1995) and successfully applied to semiconductor detectors but not yet to liquid rare gases.

The anode plate is segmented in parallel strips, grouped into two sets, indicated as A and B in Fig. 31(a); the cathode is C and Q is a negative charge. The potential of the anode A is adjusted so that all electrons produced by the ionizing radiation can be collected. The shape of the charge signals q_A and q_B induced by the motion of Q onto each set of strips is shown in Fig. 31(b). The difference $q_A - q_B$ is the charge given only by the electrons. Thus, one can measure the total charge produced by drifting electrons without using a Frish grid. This configuration, known as the virtual Frish grid method (Bolozdynya *et al.*, 2006), results in much reduced electronic noise and thus allows for better energy resolution

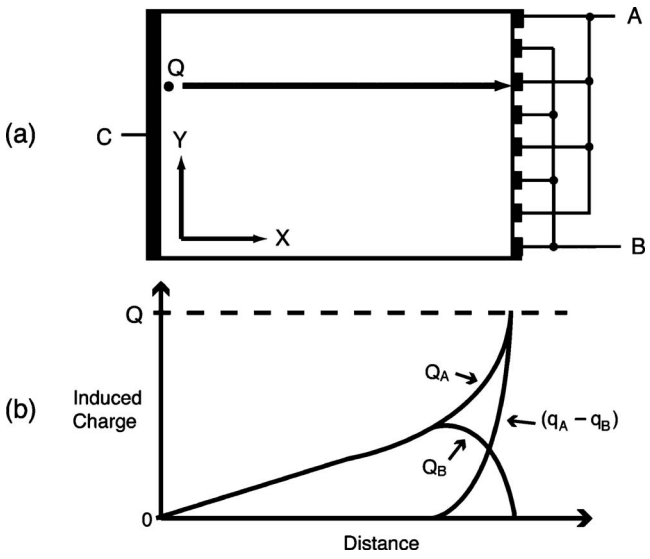

FIG. 31. Schematic of an ionization chamber with coplanar electrodes. (a) Anode made of parallel strips. (b) Time variation of the induced charge signals and the resulting signal in case the charge Q is collected onto the group of strips marked as A (Luke, 1995).

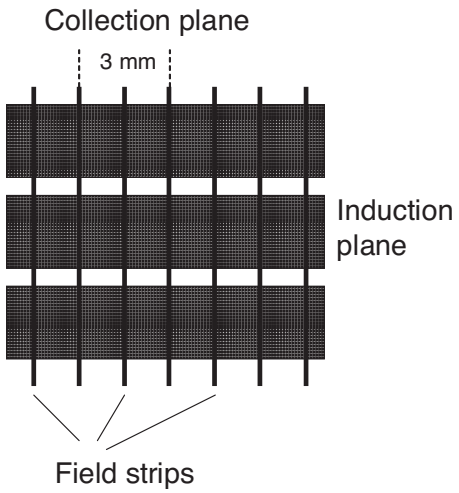

FIG. 32. An example of two-dimensional position-sensitive electrode, with orthogonal strips for collection and induction signals (Cennini *et al.*, 1994).

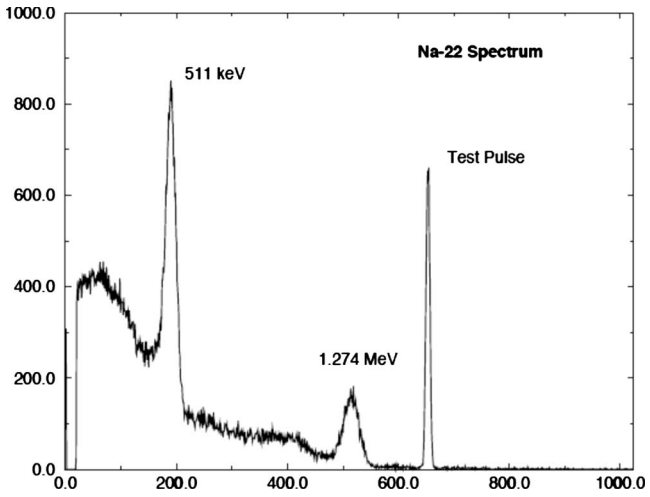

FIG. 33. The energy spectrum of ^{22}Na gamma rays measured with the gridded ionization chamber shown in Fig. 30 at 4 kV/cm drift field (Aprile *et al.*, 2002). The energy resolution of the 511 keV line is about 8% (FWHM).

and lower minimum energy threshold. Tests of such devices in LXe are planned for the near future.

With a two-dimensional strip electrode such as shown in Fig. 32, one can measure the X and Y coordinates from the collected and induced charge (Cennini *et al.*, 1994). The strips are deposited on opposite sides of a thin glass plate perpendicular to each other. The collecting strips are very thin and widely spaced, and those deposited on the back are wide, allowing a large induced signal on the back strips for a deposited energy as low as 100 keV.

Several factors contribute to the spread of the energy measured from the ionization signal detected with a gridded ionization chamber, in addition to the intrinsic fluctuation in the number of electron-ion pairs, expressed by the Fano factor and discussed in Sec. II. These include electronic noise, variation in the signal rise time due to different emission angles of the primary particle, and shielding inefficiency of the grid. As discussed in Sec. II, the best energy resolution measured to date with LXe gridded chambers is far from the Fano limit given by Eq. (5).

Figures 33 and 34 show the energy spectra of ^{22}Na and ^{60}Co gamma rays measured at a field of 4 kV/cm with the ionization chamber of Fig. 30 (Aprile *et al.*, 2002). The noise-subtracted energy resolution achieved with this chamber is consistent with 5.9% (FWHM) at 1 MeV, scaling as $E^{-1/2}$ over the measured energy range.

To measure high-energy electrons and gamma rays, which produce electromagnetic showers, a massive detector is required. A simple LXe gridded ionization chamber is not practical as a calorimeter since the very long sensitive region required for full energy deposition would involve very high voltage to generate an adequate electric field [see Fig. 35(a)]. In addition, the signal from such a chamber would be extremely slow, given the electron drift velocity in LXe. The approach used instead is a multiparallel plate electrode system such as shown in Fig. 35(b).

If the individual plate electrodes are thin, the energy loss in the electrodes is small and one can measure the energy deposited in the sensitive volume in almost fractional amounts. Such a chamber is referred to as a homogeneous calorimeter (Doke, 1993). Each cell of the calorimeter consists of two electrodes, with no wire grid. As a result, the charge Q induced in each cell can be expressed as

$$Q/e = \frac{E_0(1 - \Delta E/E_0)}{2W}, \tag{19}$$

where E_0 is the energy (expressed in eV) deposited in the calorimeter and ΔE is the fraction of energy (expressed in eV) deposited in each cell of electrodes. The effective W value under these conditions becomes $2W$ due to the positive ion effect (Doke *et al.*, 1992). In place

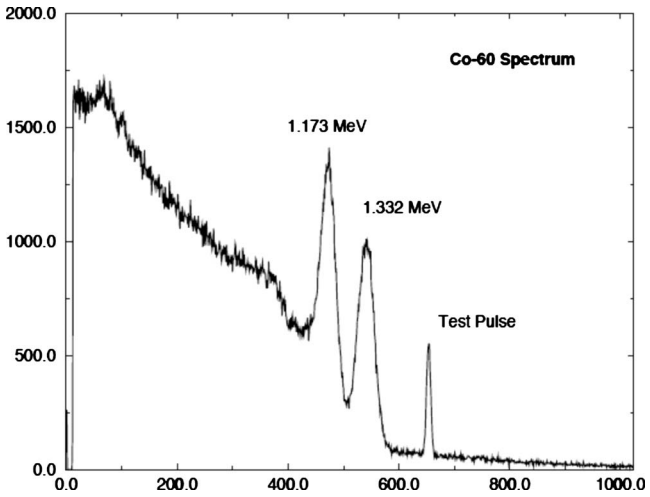

FIG. 34. The energy spectrum of ^{60}Co gamma rays measured with the gridded ionization chamber shown in Fig. 30 at 4 kV/cm drift field (Aprile *et al.*, 2002). The energy resolution of the 1.3 MeV line is about 5% (FWHM).

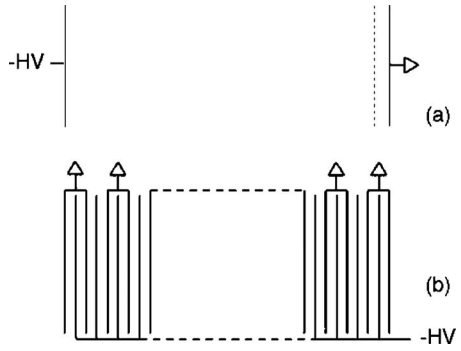

FIG. 35. Schematic of electrodes arrangement for an ionization calorimeter. (a) Gridded ionization chamber with a long sensitive region. (b) Multiparallel plate electrode system (Doke, 1993).

of such a thin electrode system, a wire electrode system may be used (Doke, Kasahara, and Suson, 1992). In addition, sometimes an electrode system with a complicated shape is used, but in such a case $2W$ should be used as the W value to estimate the charge produced by penetrating particles.

If the individual plate electrodes were thick or massive, the calorimeter is referred to as a sampling calorimeter. In this case, the calorimeter is more compact and can be used to measure the energy of very high-energy radiation. However, the energy resolution of a sampling calorimeter is significantly inferior to that of a homogeneous calorimeter. To date, large volume ionization or sampling calorimeters for high-energy physics experiments have used liquid krypton and liquid argon, respectively, but not liquid xenon, largely because of its cost.

B. Scintillation mode

Now we consider a LXe detector which is sensitive only to the scintillation process. Typically, a PMT is used to detect the scintillation photons produced by an event depositing an energy E_0 in the liquid, and the number of photoelectrons emitted from the photocathode of the PMT follows a Poisson distribution. Its spread can be expressed as $(N_{\mathrm{phe}})^{1/2}$, where N_{phe} is the number of photoelectrons, generally expressed as

$$N_{\mathrm{phe}} = \eta L_c E_0 / W_{\mathrm{ph}}. \tag{20}$$

Here η is the quantum efficiency of PMT, L_c is the light collection efficiency, and W_{ph} is the average energy required for the production of one photon.

An energy resolution better than that of an ionization detector should be obtained if η and L_c are 100%, since for a given energy E_0 deposited in LXe, the total number of scintillation photons (N_i+N_{ex}) is greater than the total number of ionization electrons (N_i), as discussed in Sec. II. However, it is difficult to achieve a complete light collection and to date the best quantum efficiency of PMTs sensitive to the vuv regime is about 35%. The energy resolution, expressed as

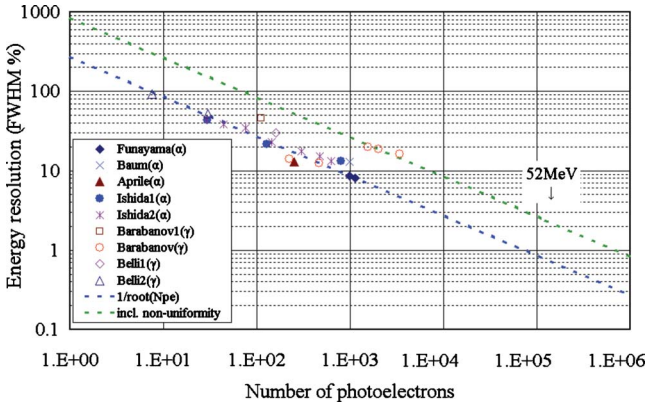

FIG. 36. (Color online) Relation between energy resolutions and the estimated number of photoelectrons obtained for α particles and γ rays (Doke and Masuda, 1999, and references therein). The lower line expresses a relation of energy resolution which is inversely proportional to the square root of the number of photoelectrons. The upper line shows a worse energy resolution expected from the nonuniformity of light collection.

$$\Delta E/E_0(\mathrm{FWHM}) \approx 2.35(N_{\mathrm{phe}})^{1/2}, \tag{21}$$

was confirmed by experiments with LXe scintillation detectors irradiated with alpha particles. Figure 36 shows the relation between the measured energy resolution and the estimated number of photoelectrons for alpha particles and for gamma rays (Doke and Masuda, 1999). The data points in the log-log plot for alpha particles are almost on a line of $1/(N_{\mathrm{phe}})^{1/2}$. In contrast, the data points for the gamma rays are scattered, and the best data were obtained only for gamma rays with energies below 0.5 MeV, where the interaction points in the liquid are localized.

In 1998, a LXe scintillation prototype, shown in Fig. 37, was built to study the detector concept later pro-

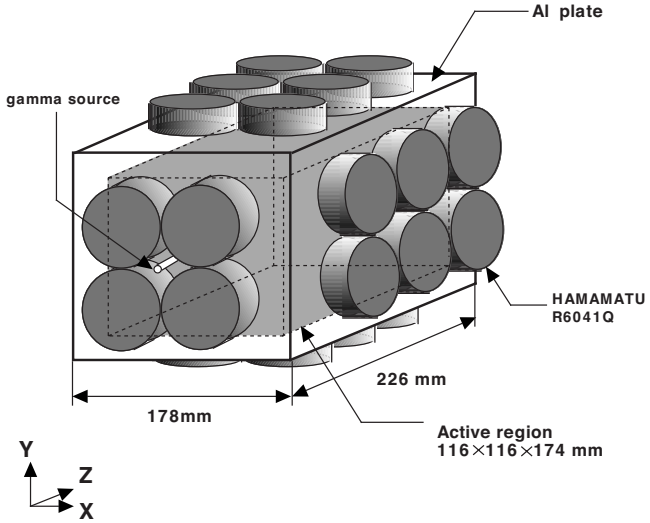

FIG. 37. Schematic of the LXe scintillation prototype with 32×2 in. PMTs (Hamamatsu R6041Q) developed for the MEG experiment (Mihara *et al.*, 2002).

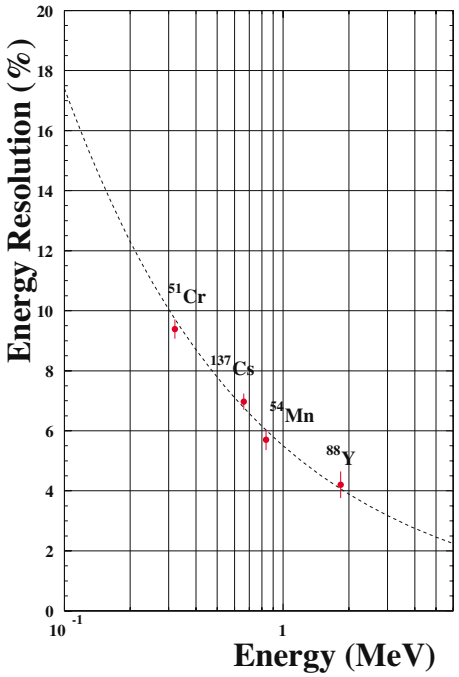

FIG. 38. (Color online) Energy resolution (1σ) as a function of gamma-ray energy, measured with the MEG detector. The data follow $1/\sqrt{N_{\mathrm{phe}}}$ as expected (Mihara *et al.*, 2002).

posed for the MEG experiment (PSI, 1999; Baldini *et al.*, 2002) discussed in Sec. IV.C.3. The prototype used 32 $\times 2$ in. PMTs (Hamamatsu R6041Q), with a quantum efficiency (QE) of about 6% (Terasawa *et al.*, 1998), to view a 2.3 l volume of LXe. Figure 38 shows the energy resolution as a function of gamma-ray energy between 0.3 and 2 MeV, measured with the MEG detector (Mihara *et al.*, 2002).

Doke, Sawada, and Tawara (2001) suggested that an energy resolution better than 1% (1σ) could be achieved for 52.8 MeV gamma rays of interest to the MEG experiment using a large sensitive volume of LXe surrounded by PMTs. The distribution of the light pattern on the PMTs would also allow a precise determination of the gamma-ray interaction points in the LXe volume. These conclusions led to the final MEG detector's design. The expected resolution of 0.8% (1σ) at 52.8 MeV was indeed directly measured in 2005 with the larger MEG prototype (see Sec. IV.C.3).

C. Sum signal mode

We now consider a LXe detector in which one simultaneously observes both ionization and scintillation signals produced by a particle interaction in the liquid, and uses their sum to infer a better energy resolution than allowed by each mode separately. As described in Sec. II, the ionization signal and scintillation signals are complementary and anticorrelated, therefore, the fluctuations of ionization and scintillation are also anticorrelated. As a result, the fluctuation of the sum signal is smaller than that of the individual signals. We have already discussed the first observations of this anticorrelation in LAr irradiated with relativistic heavy ions (Crawford *et al.*, 1987; Masuda *et al.*, 1989), later proven also in LXe irradiated with relativistic electrons (Doke *et al.*, 2002). Here we discuss more recent measurements exploiting the sum signal mode in LXe, irradiated with high-energy electrons and gamma rays. A clear anticorrelation and a substantial improvement of the energy resolution was observed by two independent groups. Conti (2003) used a single PMT coupled with an optical window to a LXe gridded ionization chamber irradiated by ^{207}Bi. A resolution of 3% (1σ) for 570 keV gamma rays was achieved at a field of 4 kV/cm.

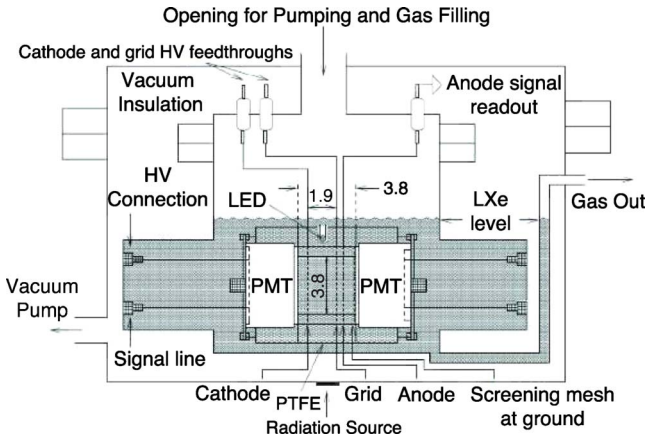

FIG. 39. (Color online) Schematic of a "sum signal mode" detector (Aprile *et al.*, 2007b).

Better results were obtained by Aprile *et al.* (2007b), using a gridded ionization chamber with PMTs immersed in the liquid. Figure 39 shows a schematic view of this detector's inner structure. The ionization chamber consists of three optically transparent mesh electrodes that serve as the cathode, Frish grid, and anode enclosed by a polytetrafluoroethylene (PTFE) tube. PTFE is used for its high reflectivity to vuv light (Yamashita *et al.*, 2004). Two Hamamatsu R9288 PMTs, mounted on both sides of the PTFE tube, detect the LXe scintillation light. One additional shielding mesh is placed between the PMT and the anode mesh to avoid induction between the PMT and the anode-charge signals. The 1.9 cm drift region between the Frish grid and the cathode defines the liquid xenon sensitive volume. The distance between the grid and the anode is 3 mm. The structure is mounted in a stainless-steel vessel and surrounded by a vacuum cryostat for thermal insulation.

The sum of the light and charge yields should be constant with applied electric field if the light yield measured in this apparatus is normalized so that it represents the number of photons emitted from the liquid xenon, and the charge yield is obtained by the number of electrons collected, as shown in Fig. 40. The variation in the light and charge yields with field is also shown in the figure. The energy spectra of ^{137}Cs γ rays measured with a 1 kV/cm drift field are shown in Fig. 41. The top two spectra were obtained separately from scintillation and ionization signals, with an energy resolution of

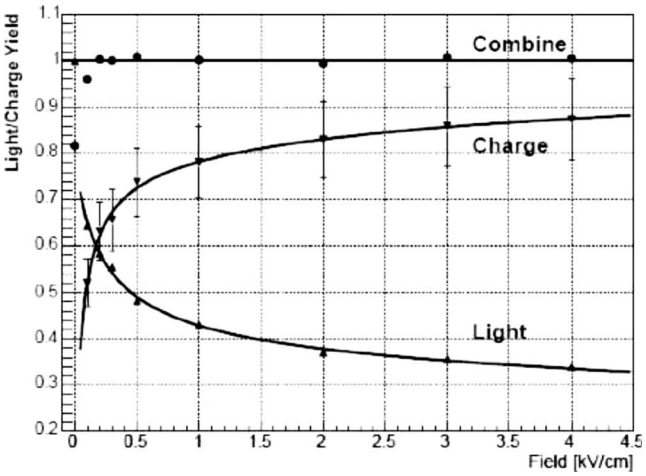

FIG. 40. Light and charge as a function of drift field for ^{137}Cs 662 keV γ rays (Aprile *et al.*, 2007b).

10.3% (1σ) and 4.8% (1σ), respectively. The strong charge-light anticorrelation is indicated in the bottom-right plot of Fig. 41. The straight line indicates the charge-light correlation angle. The charge-light combined spectrum (bottom-left) revealed a greatly improved energy resolution with a value of 1.7% (1σ).

D. Time projection chamber mode

The concept of a liquid TPC was first proposed by Rubbia (1977) for a large scale liquid argon detector dedicated to proton decay, solar neutrino, and other rare phenomena in particle physics. This type of detector allows three-dimensional (3D) event imaging, energy measurement, and particle identification. The theory of electron imaging of ionizing events and the design of the electrode system of a liquid TPC was developed by Gatti *et al.* (1979). This type of nondestructive electrode system was successfully implemented in a LXe TPC, first proposed by Aprile in 1989 for spectroscopy and Compton imaging of MeV gamma rays from astrophysical sources (Aprile and Suzuki, 1989b; Aprile *et al.*, 1995). We use this example to describe the basic principle of a TPC with three-dimensional position sensitivity.

Figure 42 shows a schematic of the TPC electrodes arrangement and of the expected pulse shapes. The LXe sensitive volume, a box of $\sim 19 \times 19 \times 7$ cm^3, is defined by a cathode, a series of field shaping rings, a wire-electrode system, and four independent anodes made of

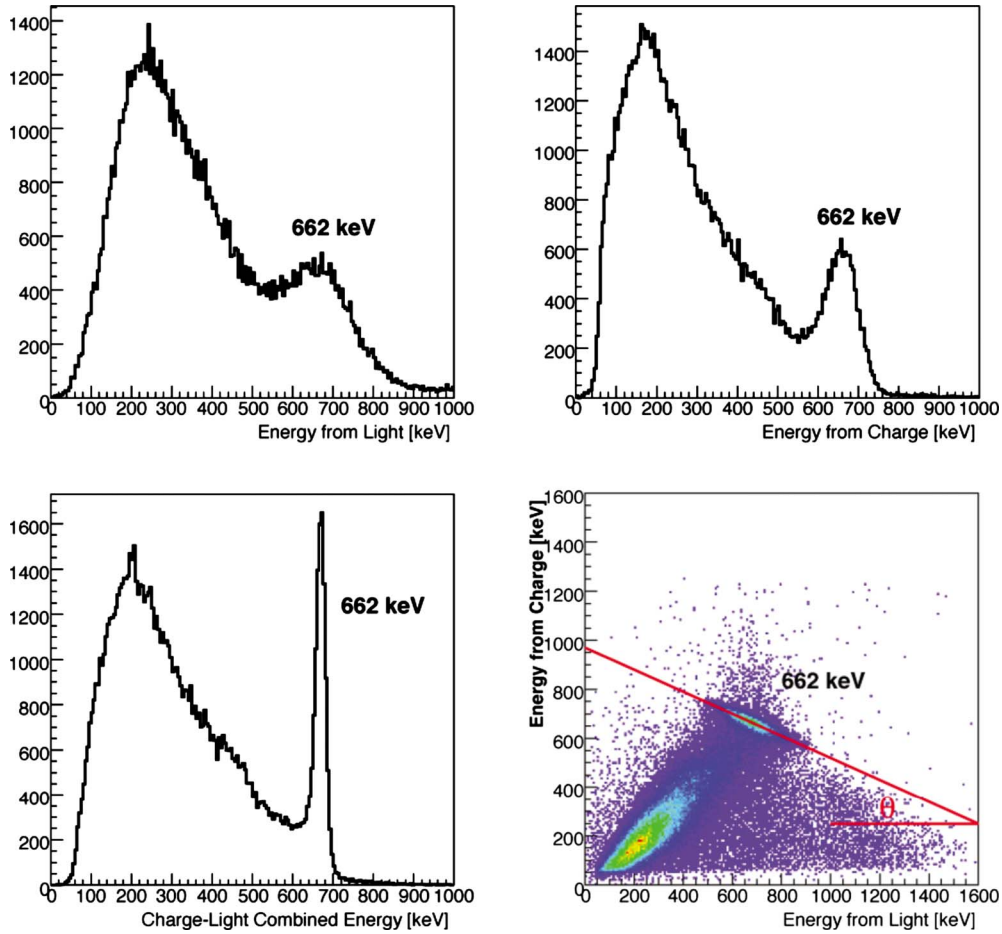

FIG. 41. (Color online) Energy spectra of ^{137}Cs 662 keV γ rays measured with 1 kV/cm field in LXe, separately from charge and light (top panels) and from combined charge and light (lower panel, left); charge-light anticorrelation and its angle (lower panel, right) (Aprile *et al.*, 2007b).

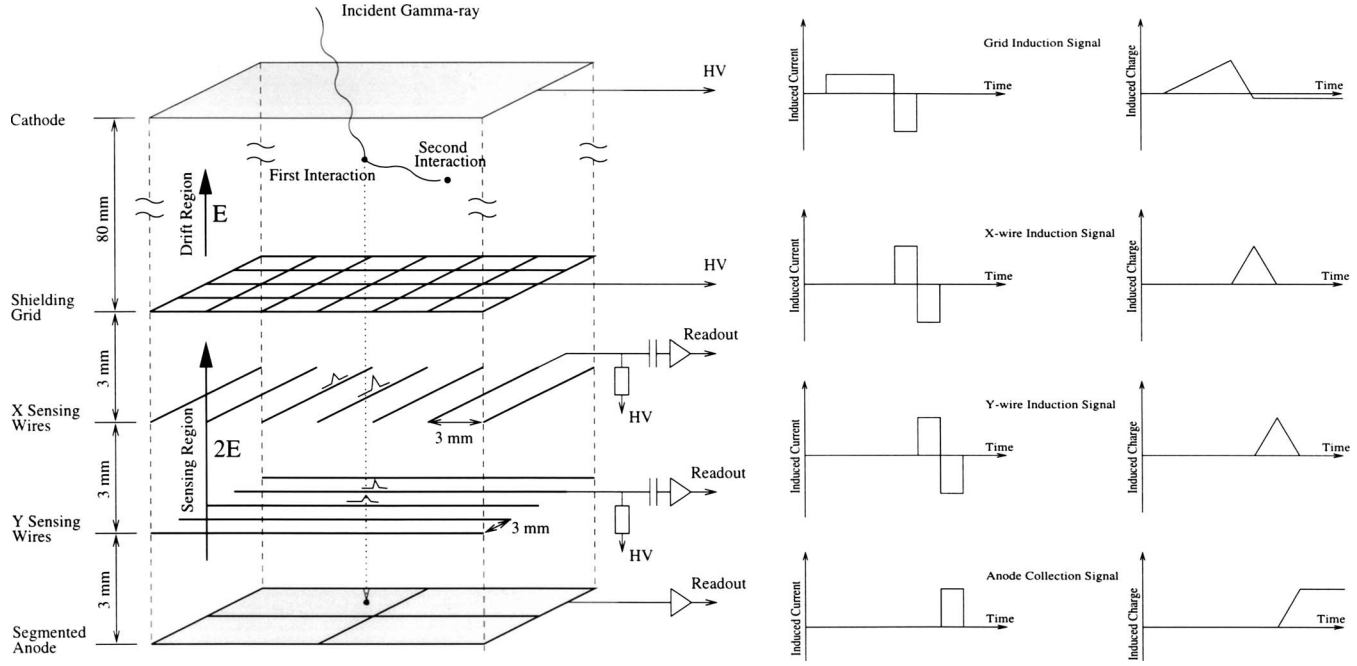

FIG. 42. Schematic of the LXe-TPC. Left: Electrodes structure (not to scale). Right: Corresponding pulse shapes (Aprile *et al.*, 1998).

wire meshes. Four vuv sensitive photomultipliers (PMTs), not shown in Fig. 42, are used to detect the scintillation light providing the initial event time t_0. Ionization electrons produced by a gamma-ray interaction in the sensitive volume, drift under an applied electric field of ~1 kV/cm, inducing a signal on two orthogonal planes of parallel wires, with a 3 mm pitch, before collection on the anodes. The signals from the wires in each plane and from the anodes are amplified and digitized at a sampling rate of 5 MHz to record the pulse shape. The location of the hit wire(s) in the two planes provide the X and Y coordinates in the TPC reference frame, while the time, measured starting from t_0, and the known drift velocity give the interaction depth (Z coordinate). The energy of the event is measured from the total charge collected by the anode(s). From the measured spatial coordinates and energy deposited in each interaction point, Compton kinematics allow reconstruction of the incoming gamma-ray direction, within the ambiguity due to the unknown direction of the Compton scattered electron. An example of the event imaging capability of this TPC is shown in Fig. 43. The event shows a 1.8 MeV γ ray with multiple Compton interactions, fully contained in the sensitive volume. The digitized pulses (0.2 μs/sample) on the wires and anodes are plotted as a function of the drift time. A new TPC of similar design as the one described above but with PMTs immersed in the liquid was built by the Waseda group (Takizawa *et al.*, 2002). It uses a wireless structure for X and Y readout and the first vuv PMTs operating at LXe temperature which were developed within the LXeGRIT R&D program in collaboration with Hamamatsu.

E. Two-phase time projection chamber mode

Excess electrons liberated in LXe by ionizing radiation can be efficiently extracted from the liquid into the gas (Bolozdynya *et al.*, 1995) for effective amplification. The process by which amplification occurs in the gas phase is called electroluminescence or proportional scintillation. Proportional scintillation of LXe was first observed by Dolgoshein *et al.* (1967). The detector that uses this secondary scintillation emission is known as a two-phase detector and it is typically operated as a TPC.

Figure 44 shows the principle of operation of a typical two-phase TPC, developed for the detection of dark

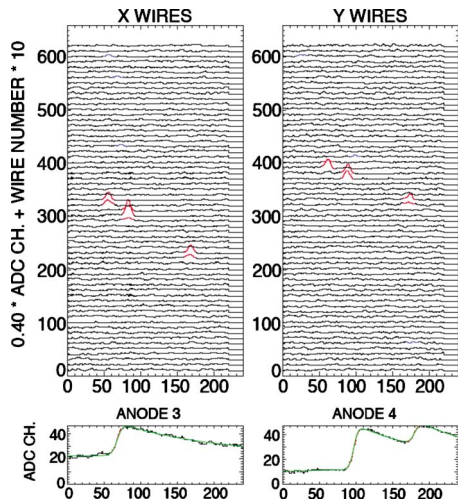

FIG. 43. (Color online) Display of a 1.8 MeV γ-ray event with multiple Compton interactions, recorded with the LXe-TPC (Aprile *et al.*, 1998).

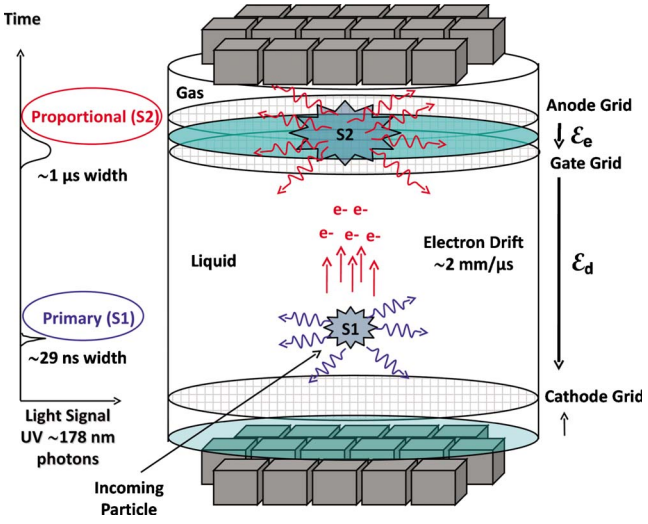

FIG. 44. (Color online) Schematic of a two-phase xenon TPC.

matter WIMPs and discussed in Sec. IV.B. Both the scintillation and the ionization, typically called the S1 and S2 signals, produced by radiation in the sensitive LXe volume are detected. As in the previous LXe TPC, ionization electrons drift under an applied electric field but once they reach the liquid surface, they are extracted into the gas phase where they emit proportional scintillation light. Figure 45 shows the extraction yield of electrons from LXe as a function of the electric field in the gas phase (Aprile *et al.*, 2004a). It is 100% for a field greater than 10 kV/cm.

The number N_γ of proportional scintillation photons is given by

$$N_\gamma = \alpha N_e(E/p - \beta)pd. \tag{22}$$

Here p is the gas pressure, E is the extraction field, d is the distance traveled by the extracted electrons in gas, N_e is the number of electrons extracted from the liquid to the gas phase, α is the amplification factor, and β is the threshold of the reduced field for proportional light production (Bolozdynya *et al.*, 1995). Typically, both the direct scintillation and the proportional scintillation are detected with vuv sensitive PMTs, located in the gas and in the liquid. Given the different index of refraction of liquid and gaseous Xe, the direct light suffers total internal reflection at the interface, and thus is most effectively detected by the PMTs in the liquid. The PMTs in the gas detect mostly the proportional scintillation light and provide x-y event localization, with a resolution ranging from millimeters to centimeters, depending on the PMTs size and granularity of the array. The third coordinate, along the drift direction, is inferred from the time difference between the direct and the proportional scintillation signals and the known electron drift velocity in the liquid, with a resolution better than ~1 mm.

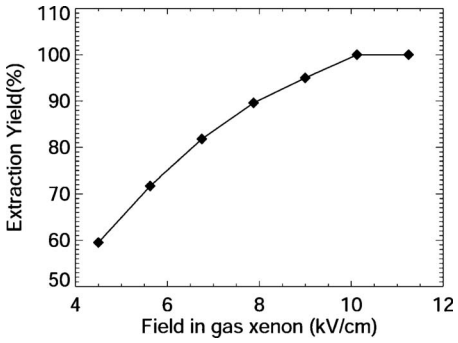

FIG. 45. Electron-extraction yield in LXe as a function of the electric field in the gas phase (Aprile *et al.*, 2004a).

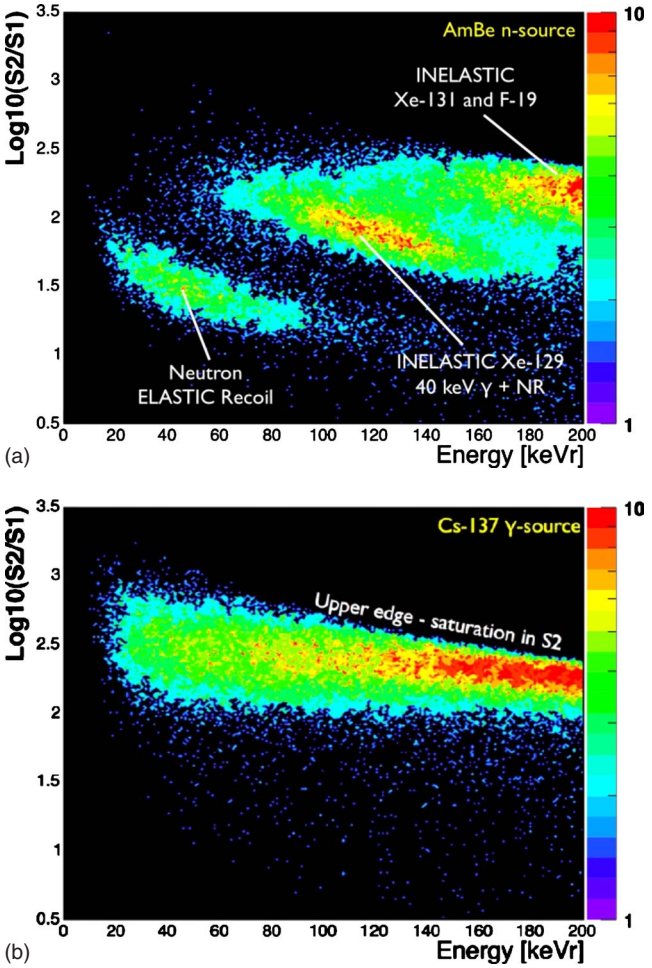

FIG. 46. (Color online) A two-phase xenon detector's response to AmBe neutrons (top) and ^{137}Cs gamma rays (bottom), at 2 kV/cm drift field (Aprile *et al.*, 2006).

The 3D position sensitivity of the TPC allows one to correct the position dependence of both the direct and proportional scintillation signals, which in turn results in improved energy resolution. The key criterion of these two-phase XeTPCs in the search for rare processes is their ability to discriminate nuclear from electron recoils. This discrimination relies on the different ratio of ionization and scintillation for nuclear and electron recoils in LXe, expected from the different ionization density and different geometry of the track structure for these two types of particles. This was first verified using a small two-phase prototype (Aprile *et al.*, 2006) developed as part of the R&D work for the XENON experiment (see Sec. IV.B.1). Figure 46 shows the response of

the two-phase prototype to neutrons and low-energy Compton scattered gamma rays. The logarithm of the ratio S2/S1 is plotted as a function of nuclear recoil energy. The elastic nuclear recoil band is clearly separated from the electron recoil band, providing the basis for discrimination against background gamma and beta rays in the two-phase Xe detectors for dark matter searches.

IV. APPLICATIONS OF LIQUID XENON DETECTORS

Several LXe detectors based on the operating principles discussed previously have been developed to address some of the most intriguing and fundamental questions in physics today, from the search for dark matter in the form of WIMPs to the search for neutrinoless double beta decay of ^{136}Xe to determine the neutrino mass. Additionally, a search for the rare $\mu \rightarrow e\gamma$ decay is currently underway with the largest ever built LXe detector, probing new physics beyond the standard model of particle physics. Finally, several R&D projects are aiming to establish LXe detectors for positron emission tomography in medicine, with direct benefit to society. In this section we review these applications of LXe detectors, covering especially the developments of the past ten years.

A. Applications to gamma-ray astrophysics

1. LXe Compton telescope for 0.3 to 20 MeV γ rays

Gamma-ray astrophysics in the medium-energy range is concerned with nuclear transition lines and the 511 keV positron annihilation line, in addition to high-energy continuum emission from accreting black holes and cosmic-ray interactions with the interstellar medium. Gamma-ray lines make this band of the electromagnetic spectrum particularly powerful for the study of the lifecycle of matter: formation and evolution of stars result in generation and ejection of heavy nuclei during the hydrostatic burning stages of stars or in their explosive end stages as supernovae. The chemically enriched interstellar medium, in turn, becomes the birth place for a new generation of stars, providing the building blocks of life in the Universe. Gamma-ray lines, through spectroscopy and imaging, provide the deepest look into the explosion mechanism of both gravitational core collapse supernovae and thermonuclear white dwarf supernovae (Diehl, Prantzos, and von Ballmoos, 2006).

The various astrophysical sources impose different requirements on the energy resolution of an instrument: for gamma-ray line spectroscopy of white dwarf supernovae, an energy resolution of ~3% FWHM at ~847 keV is necessary. For other sources such as diffuse ^{26}Al or ^{60}Fe emission, gamma-ray lines are below the resolution of even germanium spectrometers (Diehl *et al.*, 2008), and hence the accessible astrophysical information lies predominantly in the observed intensity distribution, which must be determined with a resolution of order 1°.

The low source fluxes combined with high background from interactions of cosmic rays or trapped protons with

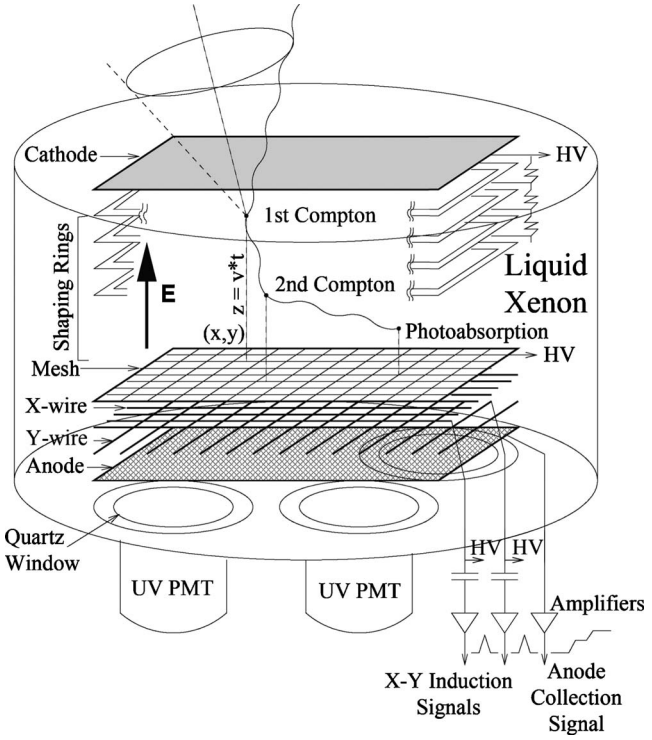

FIG. 47. Schematic of a LXe-TPC as Compton telescope (Aprile *et al.*, 2004b).

structural and detector materials require a large field of view (FOV), a large effective area, low intrinsic background, and excellent background discrimination. Given the dominance of the Compton cross section at these energies, a compact Compton telescope, ideally with time of flight (TOF) capability, is the most promising concept. The idea of a LXeTPC as a Compton telescope for MeV γ-ray astrophysics was first proposed by Aprile *et al.* (1989). A series of experiments with LXe detectors followed, aimed at establishing the charge and light yields, with specific emphasis on the use of LXe in a position sensitive detector (Aprile, Mukherjee, and Suzuki, 1990, 1991a, 1991b, 1991c). The development of the first LXe-TPC prototype, described in Sec. III.D, led to the realization of a balloon-borne instrument, the liquid xenon gamma-ray imaging telescope (LXeGRIT) (Aprile *et al.*, 1998, 2000; Curioni *et al.*, 2007). Figure 47 shows the principle of operation of a LXe-TPC as Compton telescope.

A mechanical drawing of the TPC is shown in Fig. 48. The TPC electrodes are mounted on a 42-cm-diameter flange (see Fig. 49) which encloses a 10 l cylindrical vessel. Four PMTs, coupled to the vessel via quartz window, detect the scintillation light, used as trigger. Xe gas, purified to <1 ppb O_2 equivalent, by a combination of a hot metal getter and a cooled molecular sieve filter, is liquefied into the vessel by a controlled flow of liquid nitrogen (LN_2) through the copper coil of a condenser on the top. Thermal insulation of the cold vessel is provided by a vacuum cryostat. To maintain the insulation and the cooling during a balloon flight, a sorption pump embedded in the custom-built LN_2 Dewar carried on

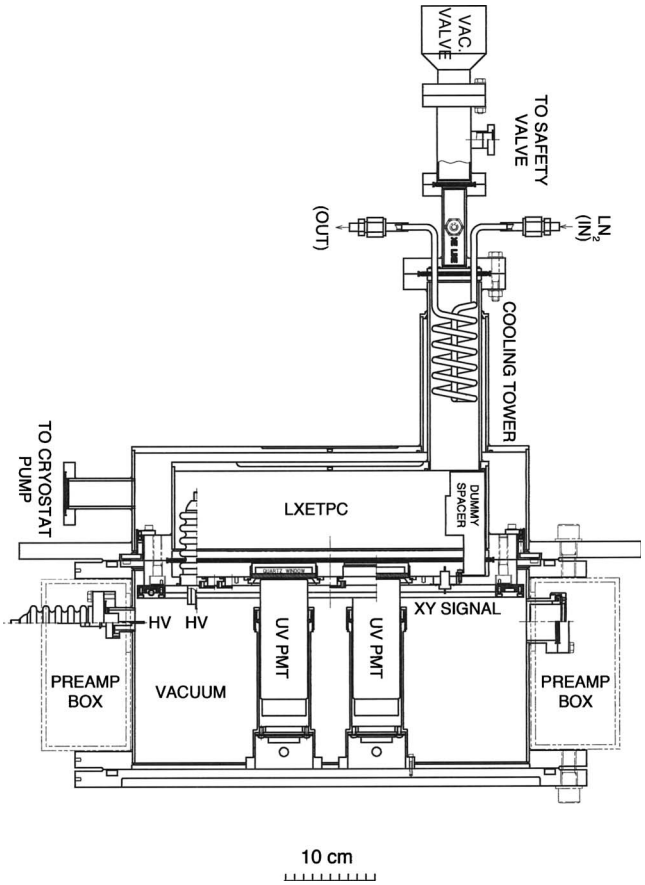

FIG. 48. Mechanical drawing of the LXeGRIT TPC (Aprile *et al.*, 2004b).

board was used. The liquid temperature of ~−95 °C, corresponding to a pressure of 1.5 atm, was reliably maintained for periods of many days. As the launch date and time are not known *a priori*, the detector must be filled and operational well in advance (a couple of days) of a launch opportunity. This requires a good purity of the gas, a low outgassing rate for the detector, and a reliable cooling system. We note that this first LXe-TPC did not use continuous gas circulation through purifiers,

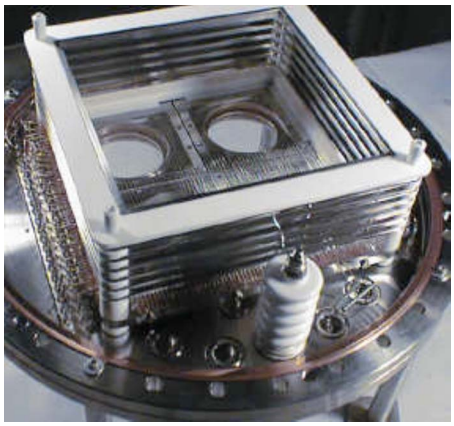

FIG. 49. (Color online) Photo of the LXeGRIT TPC structure (cathode removed) (Aprile *et al.*, 2004b).

TABLE VI. LXeGRIT payload characteristics.

Energy range	0.2–20 MeV
Energy resolution (FWHM)	$8.8\% \times (1\ \text{MeV}/E)^{1/2}$
Position resolution (1σ)	1 mm (three dimensions)
Angular resolution (1σ)	3° at ~1.8 MeV
Field of view (FWHM)	1 sr
Effective area (imaging)	16 cm^2 at 1 MeV
LXeTPC active volume	20 cm × 20 cm × 7 cm
Active back shield	2730 cm^2, 10-cm-thick NaI(Tl)
Active side shield	4750 cm^2, 10-cm-thick NaI(Tl)
Active top shield	1600 cm^2, 1.2-cm-thick plastic
LN_2 Dewar	100 l
Instrument mass, power	1100 kg, 450 W
Telemetry, onboard storage	~2 × 500 kbps, ~2 × 9 GB

yet long electron lifetime was achieved and the charge stability with time was verified both in laboratory testing and after the recovery of the payload.

LXeGRIT was tested in balloon flights in 1999 and 2000 (Aprile *et al.*, 2003, 2004b; Curioni *et al.*, 2003, 2007), measuring for the first time the internal and atmospheric background spectrum at balloon altitude, confirming the comparatively low intrinsic background of a LXe instrument. Table VI shows the characteristics of the payload in the 1999 flight configuration.

A Compton telescope works by reconstructing statistically the arrival direction of multiple source gamma rays from measurement of the Compton scatter angle and the direction of the scattered gamma ray. This requires identification of the locations of the first Compton scatter location, and the second interaction point, including their sequence. For determination of the Compton scatter angle φ, the energy deposit in the first interaction point E_1 and measurement of the total gamma-ray energy are required, according to

$$\cos\varphi = 1 - \frac{E_0}{E_{\text{tot}} - E_1} + \frac{E_0}{E_{\text{tot}}}, \tag{23}$$

where E_0 is the electron rest energy. The angular resolution is determined not only by the uncertainty in the locations of the first and second interaction points but also by the energy resolution of the detector. For best efficiency, the energy threshold should be as low as 50 keV, placing stringent requirements on the noise performance of the charge readout system. LXeGRIT achieved a position resolution of 0.85 mm (1σ) in X/Y and 0.25 mm in Z, an energy resolution of 4.3% (1σ) at 1 MeV (Curioni *et al.*, 2007) (see Fig. 50), and an energy threshold for imaging of 150 keV (below 100 keV for spectroscopy). LXeGRIT demonstrated successful reconstruction of the interaction sequence for three or four interactions in the sensitive volume (Oberlack *et al.*, 2000) and imaging performance with 3° resolution (1σ) at ~1.8 MeV (Aprile *et al.*, 2008). Figure 51 shows an image of two calibration sources, imaged using a maximum likelihood technique. The angular resolution is

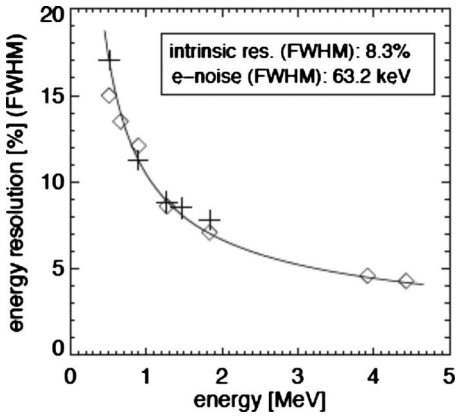

FIG. 50. The energy resolution of LXeGRIT as a function of energy, as measured in flight. The crosses and diamonds are data from two balloon flights (Curioni *et al.*, 2007).

dominated by the selection of scatter angles (large scatter angles were preferred due to the limited drift gap of ~7 cm) and the energy resolution of the instrument, whereas the position resolution for individual interactions plays a role mainly for scatter angles below 40°.

LXeGRIT was truly a prototype, in that it successfully demonstrated the principle while also indicating paths for future improvements. Lacking powerful event rejection, the digital readout system turned out to be a bottleneck for the performance of the instrument (Aprile *et al.*, 1998). The light yield, based on the readout of 4 PMTs mounted outside the cryostat, was too limited to provide effective trigger cuts in energy and could therefore not effectively discriminate against charged particles at the trigger level.

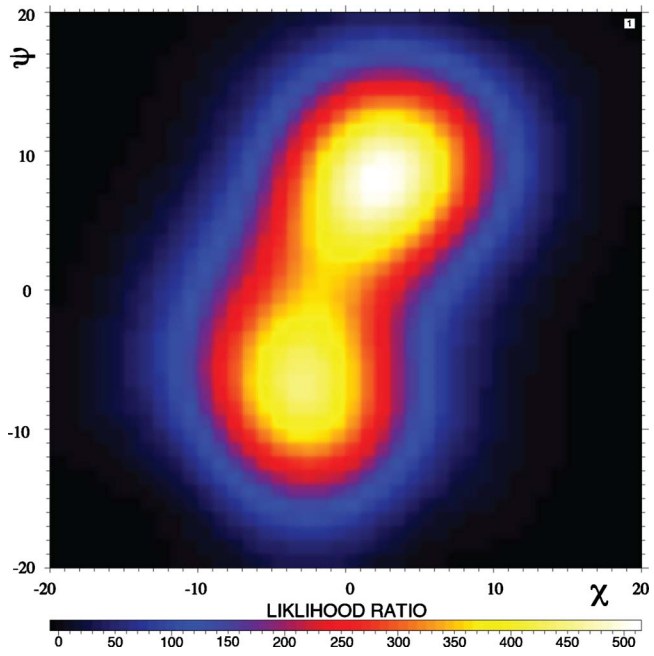

FIG. 51. (Color online) LXeGRIT image (reconstructed angles in degrees) of two calibration sources, ^{60}Co and ^{60}Na, using a maximum likelihood imaging technique (Aprile *et al.*, 2008).

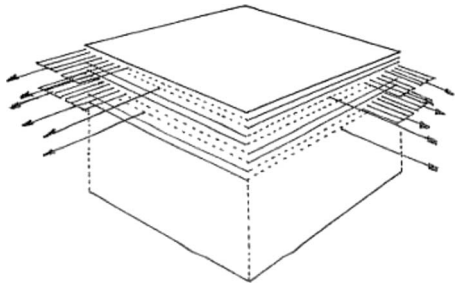

FIG. 52. Schematic of the wire electrode system for the LXe ionization calorimeter for GeV gamma rays (Doke *et al.*, 1989; Doke, Kasahara, and Suson, 1992).

Various improvements over LXeGRIT have been suggested and tested in smaller setups, from enhanced light collection with PMTs in the liquid to enhanced energy resolution based on light-charge anticorrelation as discussed in Sec. II. Moreover, the fast scintillation light should enable TOF in a compact double scatter Compton telescope with 10–15 cm separation between detector planes. This would not only result in powerful discrimination against background at the trigger level, by distinguishing between forward and backward scattered events, but also in greatly enhanced efficiency.

2. LXe ionization calorimeter for 10 to 100 GeV γ rays

A design study of a LXe homogeneous calorimeter for astrophysical gamma-ray lines in the 10–100 GeV energy range was carried out in early 1990 by the Waseda group (Doke *et al.*, 1989; Doke, Kasahara, and Suson, 1992). The goals were a geometric factor of ~1 m^2 sr, requiring a LXe volume of ~0.6 m^3 (1.7 tons) and an energy resolution better than 1% (1σ) for energies in the 3–70 GeV range. By comparison, the energy resolution of the crystal calorimeter on board the recently launched Fermi observatory is about 10% (1σ) at 80 GeV (Atwood *et al.*, 2009). A schematic drawing of the LXe calorimeter is shown in Fig. 52 including a cross-section view of the wire electrodes. Monte Carlo simulations have shown that an energy resolution <0.5% (1σ), a position resolution of 2.4 mm, and an angular resolution of 0.3°–1.6° could be achieved for gamma rays at normal incidence, in the 3–70 GeV energy range.

With its large effective area and superior energy resolution, such a detector would be ideal to search for gamma-ray lines in the range 10–100 GeV which may result from the annihilation of WIMPs in the Galactic halo (see next section for methods of direct detection of these). Fast timing is necessary for rejection of charged particle background, and scintillation light detection by fast PMTs or LAAPDs embedded in the calorimeter is needed for a reliable trigger of the gamma events.

While there are currently no plans for the realization of such a LXe telescope for a space mission, we believe that the advancement of efficient photodetectors operating in the liquid and of efficient cryocoolers able to maintain the cryogenic liquid for extended periods of

time are two enabling technologies for this application. On the other hand, the intrinsic long dead time limitation of this type of calorimeter can be resolved by a LXe scintillating calorimeter, with energy and spatial resolution still superior to most other detector approaches. This has recently been in fact achieved by the MEG experiment discussed in Sec. IV.C.3.

B. Applications to dark matter direct detection

A major experimental effort worldwide aims at the direct detection of Galactic dark matter, with a variety of detectors and methods (Jungman, Kamionkowski, and Griest, 1996). The motion of stars and gas in galaxies, including our own, indicates that the stars are immersed in a dominant component of nonluminous matter, 5–10 times the total mass of the stars, and responsible for most of the gravitational binding. Other evidence indicates that this "dark matter" is nonbaryonic and cold. The leading theoretical suggestion, based on supersymmetry theory, is that it consists of new particles (WIMPs) in the mass range 10–1000 GeV. Such particles could be detected through collisions with targets of normal matter, producing nuclear recoils, with energies <100 keV. Xenon is a particularly suitable dark matter target because of its high atomic number (coherent weak interaction rates being proportional to A^2) and because it contains odd and even isotopes allowing a study of both spin-dependent and spin-independent interactions.

The principal experimental obstacle is that the predicted interaction cross sections are typically in the range 10^{-6}–10^{-10} pb (1 pb$=10^{-36}$ cm^2) giving event rates $\sim 1\times 10^{-4}$/(kg d) in a Xe target, compared with ambient background rates typically 10^6 times higher from radioactivity in detector materials, shielding structures and the surrounding environment, as well as from cosmic-ray muons. The latter can be reduced by operating detectors deep underground, while the former can be reduced using high-purity detector and shielding materials, veto techniques, and detectors with discriminating power against gamma, electron (beta decay) and alpha background. To achieve the large mass and the low-energy threshold which is required for Xe as a WIMP target, the favorite approach is a TPC operated in two-phase (liquid or gas), originally proposed by Barabash and Bolozdynia (1989) and discussed in Sec. III.E. Simultaneous detection of both ionization and scintillation signals provides greater information than detection of either ionization or scintillation alone. Both signals are typically detected with photomultipliers placed around the target region. The direct scintillation signal is referred to as S1 and the ionization signal turned into a proportional scintillation signal is referred to as S2, as shown in Fig. 44. The ratio S2/S1 is found to differ significantly for nuclear and electron recoils (the latter from gammas or beta decay) and a mixture of signal and background separates into two populations of events with an overlap of only 0.1–1 %, dependent on the geometry and electric fields. The event energy can be obtained, after calibration with gamma sources, from the amplitude of the S1 signal, while the event position can be reconstructed in the transverse x-y plane from the distribution of the S2 signal in the PMT array, and in the vertical direction from the time difference between the prompt S1 signal and the ionization drift time. Thus the two-phase XeTPC approach provides full 3D event localization with a position resolution varying from a millimeter to several centimeters, determined largely by the granularity of the PMTs array. The energy threshold is determined by the collection efficiency of the direct light.

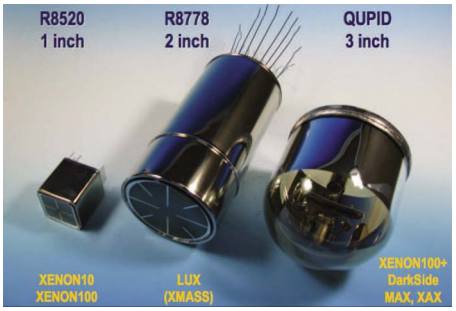

FIG. 53. (Color online) Photo of the different Hamamatsu PMTs developed for the XENON and XMASS dark matter experiments.

Four collaborations are currently using or developing LXe detectors for dark matter: the XENON, ZEPLIN, and LUX Collaborations have chosen the two-phase TPC approach, while the XMASS Collaboration has chosen the single-phase detector approach, using only the scintillation signal. The XENON detectors have so far adopted a geometry with the drift length similar to the detector diameter, and with PMT arrays in the gas and in the liquid, to achieve a very low-energy threshold for nuclear recoils. A moderate field of ~ 1 kV/cm is used and by adopting small size metal channel PMTs with 1 in. square geometry, good photocathode coverage for maximum S1 signal detection and high spatial resolution with S2 signal detection is emphasized. For larger scale devices, radioactivity and cost considerations have led to a design based on a larger size (3 in spherical shape) novel-type PMT, the quartz photon intensifying detector (QUPID), developed by UCLA and Hamamatsu (Arisaka *et al.*, 2009). Figure 53 shows a photo of the QUPID device, in comparison with the other special PMTs developed by Hamamatsu for the XENON and XMASS experiments.

The ZEPLIN detectors have adopted a single array of large size PMTs. ZEPLIN II used 3 in. diameter PMTs placed in the gas phase, resulting in comparatively low light yield due to the loss of light by total internal reflection at the liquid/gas interface. ZEPLIN III focused on high light yield, viewing the sensitive volume from below with an array of 2 in. diameter PMTs, and on high field operation, resulting in a shallow geometry, with a short drift gap and hence a more limited mass of LXe.

The LUX detector, currently in development, follows the XENON design with larger size PMTs both in liquid

and gas. A taller geometry is used to allow a large cut in the drift direction, required to suppress backgrounds from the PMTs radioactivity. Finally, XMASS uses a single large volume of LXe surrounded on all sides by PMTs, to efficiently detect the scintillation light for both energy and position measurement. The original 2 in. diameter PMT developed by Hamamatsu for XMASS (R8778) has been modified into an "hexagonal" geometry to enable better photocathode coverage of a near spherical volume of LXe.

The sensitivity to dark matter is dependent on target mass, running time, achieved background levels, and energy threshold. So far no signal has been seen in a few months running of any of the detectors. These searches have chosen to make faster and more cost-effective progress by upgrading or constructing new detectors to achieve improvements of an order of magnitude at each step. Thus the detectors reviewed below are often in the form of a series of detectors, progressively improving the sensitivity limits, using larger target masses and/or improvements in background.

The measure of the sensitivity of a given experiment is normally given by the 90% confidence upper limit on the hypothetical WIMP-nucleon dark matter cross section. The determination of this signal upper limit, in the presence of residual background, is more difficult than in the case of a measured positive signal. There is no unique definition of "90% confidence" when one wishes to look both for a nonzero signal and at the same time find an upper limit (Feldman and Cousins, 1998). There is also a difference of definition between a "one-sided" or "two-sided" limit (Feldman and Cousins, 1998) so that the quoted value from a given experiment can vary by a factor of 2 depending on the method and definition used, and in particular on the method used to take account of residual backgrounds.

1. The XENON detectors

The XENON dark matter search is a phased program aiming at progressively improved sensitivity by the series of two-phase TPCs, XENON10, XENON100, and XENON1000, the numbers referring to the order of magnitude of fiducial target mass in kg.

The XENON10 experiment (Aprile *et al.*, 2010) contained a total of 25 kg of pure LXe, of which 14 kg were used in the active target enclosed by a PTFE cylinder of 20 cm inner diameter and 15 cm height. PTFE is used for its high reflectivity in the vuv regime (Yamashita *et al.*, 2004). Figure 54 shows the detector's schematic. The TPC was equipped with four meshes: the cathode and one mesh below the liquid surface set up the drift field, together with field shaping rings in the cylinder. One mesh just above the liquid surface is kept at positive high voltage, providing a field of ~10 kV/cm for fully efficient electron extraction. A fourth mesh on top serves to close the field lines. The active volume was observed by top and bottom arrays totaling 88 (Hamamatsu R8520-06-Al) PMTs, selected for low U/Th radioactivity. The majority of the S1 signal is seen by the lower array (located in the liquid) due to total internal reflection from the liquid surface, while the S2 signal (from the gas) is seen mainly by the top array. The light yield in XENON10 was 2.2 photoelectron/keV allowing 5 keV nuclear recoil energy threshold. To eliminate background events at the edges of the detectors, the volume was fiducialized (by radial, top, and bottom software cuts) to a mass of 5.4 kg. The maximum drift length in the liquid was 15 cm, and the drift field was 0.7 kV/cm.

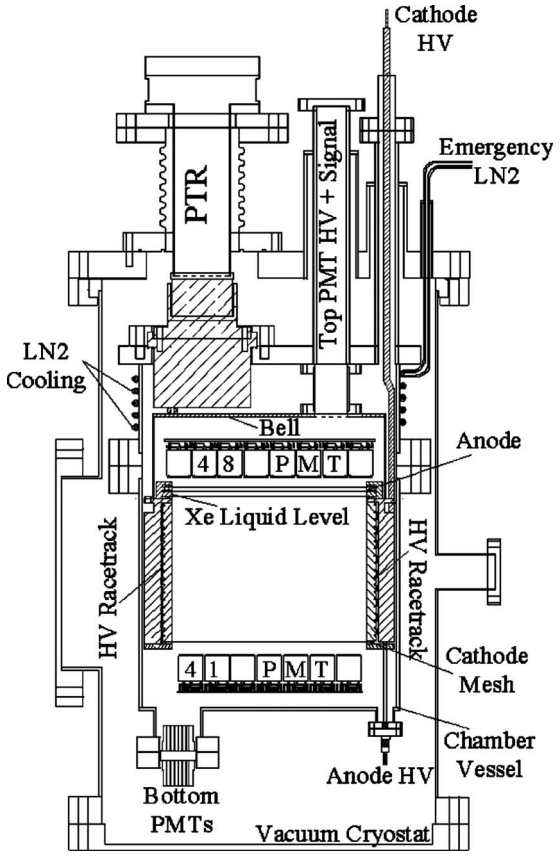

FIG. 54. Schematic of the XENON10 detector (Aprile *et al.*, 2010).

XENON10 was cooled by a 65 W pulse tube refrigerator (PTR) (Haruyama *et al.*, 2004) coupled to the liquid volume via a copper head in the top of the detector, as shown in Fig. 54. Xenon was purified in the gas phase by continuous circulation through a commercial hot getter. An electron lifetime in excess of 2 ms was achieved with this system. Figure 55 shows a schematic of the purification system. The experiment was located in the Gran Sasso National Laboratory at a depth of 3800 m water equivalent (mwe). The XENON10 cryostat, made of stainless steel, was enclosed in a structure made of 20-cm-thick lead and 20-cm-thick polyethylene to shield it from gamma rays and neutron background. After calibration with gamma and neutron sources, the experiment ran for two months, obtaining in the predefined signal region a background of six events as expected from the gamma background, and four spurious events which could be rejected as possible signal events. Based

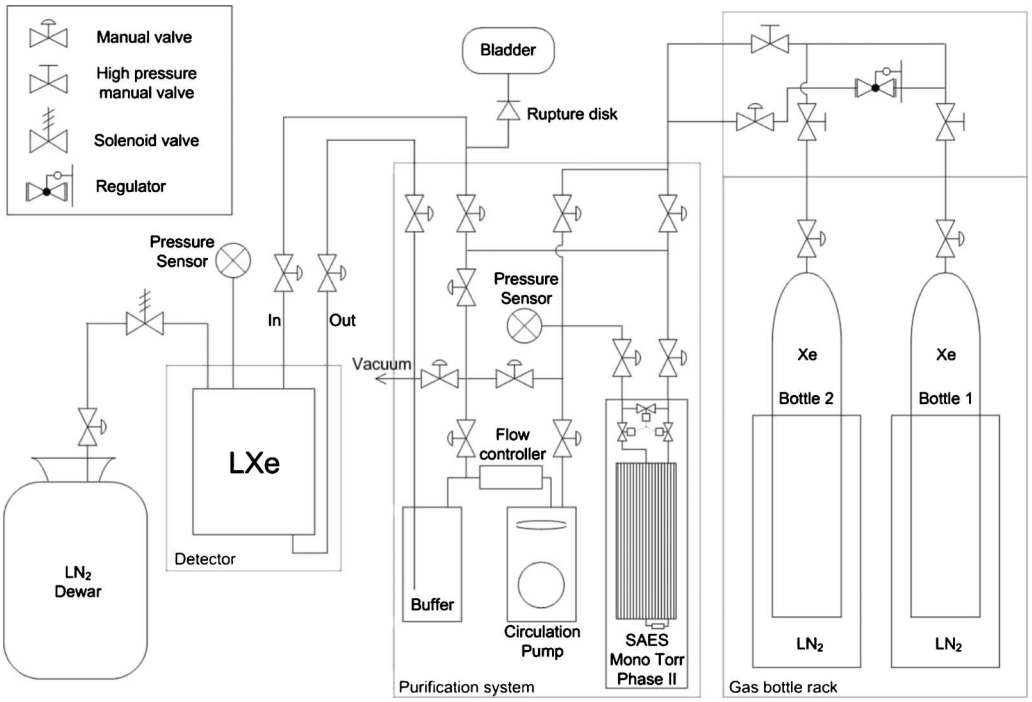

FIG. 55. The XENON10 detector purification system (Aprile *et al.*, 2010).

on these data, the XENON10 experiment was able to exclude previously unexplored parameter space in WIMP-nucleon scattering cross section, setting improved upper limits on both spin-independent (Angle *et al.*, 2008b) and spin-dependent (Angle *et al.*, 2008a) WIMP coupling to matter. The excellent XENON10 results, validated the scientific reach of a position sensitive, homogeneous and self-triggered LXe-TPC for dark matter direct detection.

The XENON100 detector (Aprile and Baudis, 2008) has replaced XENON10 and is now operating underground at the Gran Sasso National Laboratory. The new TPC incorporates the successful design features of XENON10 but aims at improving the background rate by a factor of 100 by the use of (a) lower background version of the same type of PMT (Hamamatsu R8520-06-Al-mod), (b) reduction in the mass and radioactivity of the cryostat, including selection of low-activity stainless steel, (c) improved screening of other construction materials, and (d) a new cryogenic system designed to remove the refrigerator system from the vicinity of the experiment. In addition, an active LXe veto was added around the target volume. The active veto and target volume are separated by a PTFE cylinder. The target is viewed from the top and the bottom by a total of 178 $\times 1$ in. low background PMTs. The Xe veto region is independently viewed by 64 PMTs, from the XENON10 detector. The XENON100 TPC has a drift length of 30 cm and requires a total of ~170 kg of LXe of which ~70 kg are in the target. The LXe is contained in a double wall stainless steel vessel and cooling is provided by a 170 W PTR, the same type as used on the MEG detector discussed later (Haruyama *et al.*, 2004). The PTR is used both to liquefy the gas and to maintain the liquid temperature during operation. Figure 56 shows a schematic of the XENON100 TPC and its overall assembly in the vacuum cryostat. Figure 57 shows the assembled (a) top and (b) bottom PMT arrays used in XENON100.

The detector is enclosed in a passive shield of polyethylene and lead to reduce the neutron and gamma background. Figure 58 shows the assembled XENON100

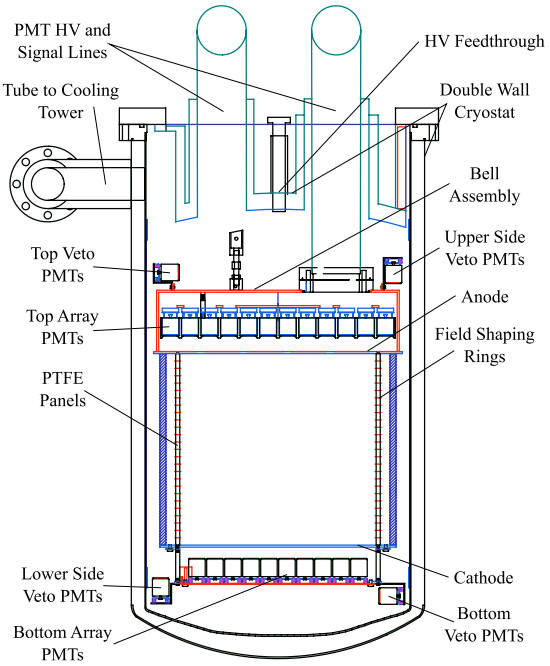

FIG. 56. (Color online) Schematic of the XENON100 detector (Aprile and Baudis, 2008).

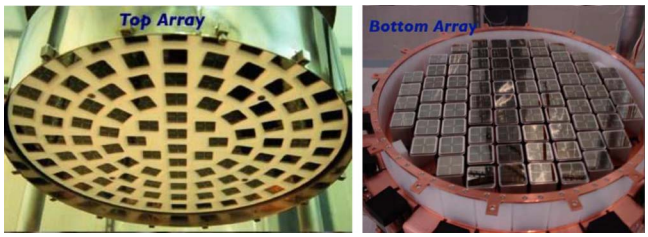

FIG. 57. (Color online) Photos of the top and bottom PMT arrays of the XENON100 detector.

mounted inside the open shield cavity. From the improvements in design and materials selection, the background objective is to reach $<10^{-3}$ gamma/(kg d keV), and <1 neutron/(100 kg yr), in 50 kg fiducial mass. High-energy neutrons from muon spallation in the rock are calculated to be <0.3/(100 kg yr). The intrinsic rate of electron recoils from radioactive ^{85}Kr in Xe will be reduced to 10^{-4} event/(kg d keV), corresponding to a Kr/Xe level of 5 parts per trillion (ppt), using a dedicated cryogenic distillation column. After full commissioning and calibration with neutron and gamma sources, this detector has become operational for science runs in late 2009, aiming at a spin-independent sensitivity of 2×10^{-9} pb for 100 GeV WIMPs. This large gain over XENON10 is achievable partly through the increase in fiducial mass and partly through the reduction in background, while maintaining the same low-energy threshold.

If a dark matter signal is seen at this cross-section level, there will be a clear need to obtain a sufficient number of events to make a spectrum, from which the WIMP mass could be estimated. Studies of a larger 1 ton detector are already in progress, and the XENON100 phase provides the testing of many of the key technologies and performance characteristics relevant to the realization of 1–20 ton Xe detectors. To achieve the necessary further background reduction, an increased amount of Xe self-shielding and a full 4π coverage with QUPID photodetectors (Arisaka *et al.*, 2009) is planned (Fig. 59).

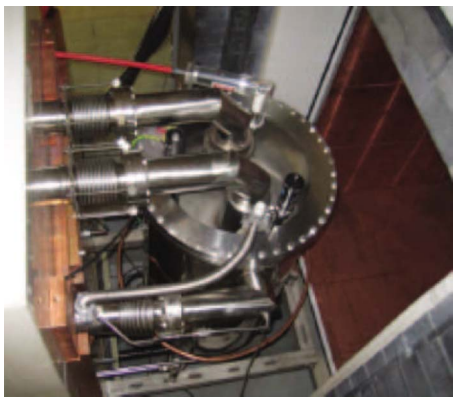

FIG. 58. (Color online) Photo of the XENON100 detector installed in its shield (Aprile, 2008).

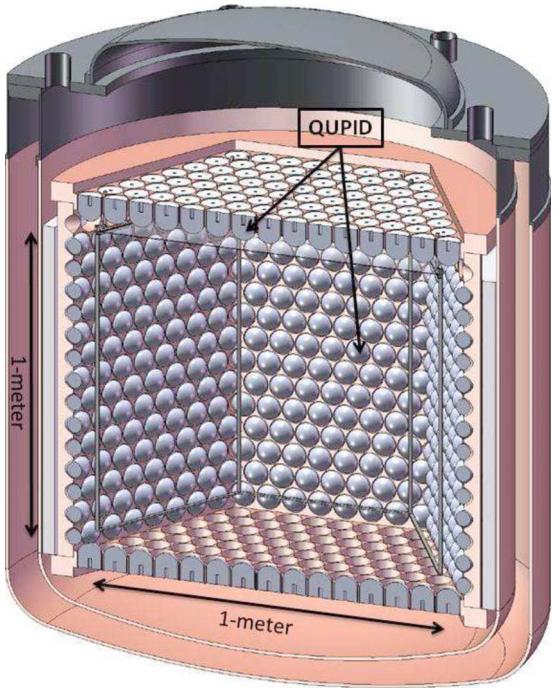

FIG. 59. (Color online) Schematic of the XENON1T detector.

Recent Monte Carlo studies indicate that for an adequate amount of self-shielding, a xenon TPC with an inner fiducial volume of 1 ton would require a total mass of 2.4 tons. In addition to the intended capability of measuring a spectrum of events at 10^{-10} pb, this detector would have an ultimate sensitivity of 10^{-11} pb. Studies have also been made of a multiton, two target system (Xe and Ar) for dark matter, double beta decay, and *pp* solar neutrinos (Arisaka *et al.*, 2009).

2. The ZEPLIN detectors

The ZEPLIN Collaboration has been operating LXe detectors for dark matter at the UK Boulby Mine underground site, already prior to the XENON Collaboration. After ZEPLIN I, a 3 kg single phase detector that reached a sensitivity 10^{-6} pb in 90 days of operation, the collaboration focused on constructing the first two-phase Xe TPC. ZEPLIN II used a 35 kg LXe target viewed by seven 3 in. low background PMTs (ETL D742) located in the gas above the liquid (Fig. 60). The electron drift distance was 14 cm, similar to that of XENON10. Shielding was 20 cm lead outside of a 30 cm thickness liquid scintillator active veto, which provided both passive neutron shielding and active gamma shielding to remove residual gamma rays penetrating the lead shield. The target region was defined by a tapered PTFE annulus serving as a light reflector and support for electric field-shaping rings. Grids above and below the liquid provided a drift field of 1 kV/cm in the liquid, and a third grid in the gas provided an 8 kV/cm field to extract electrons from the liquid with 90% efficiency. The light yield was limited to 1.5 photoelectron/keV, giving an energy threshold of 5 keV for electron recoils. The whole assembly was located in the 2800 mwe Boulby salt

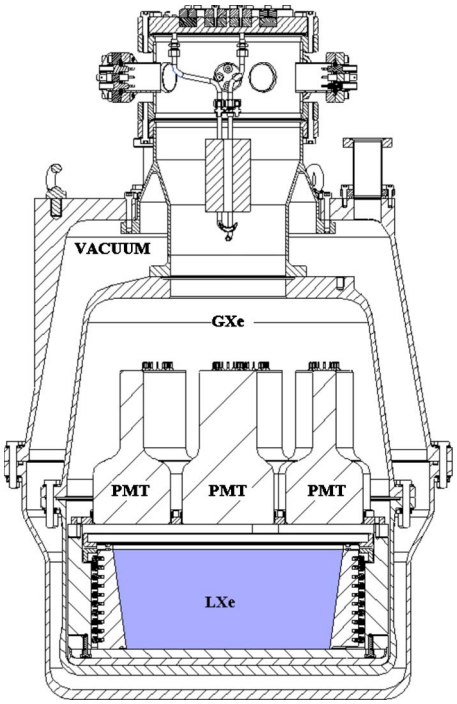

FIG. 60. (Color online) Schematic of the ZEPLIN II detector (Alner *et al.*, 2007).

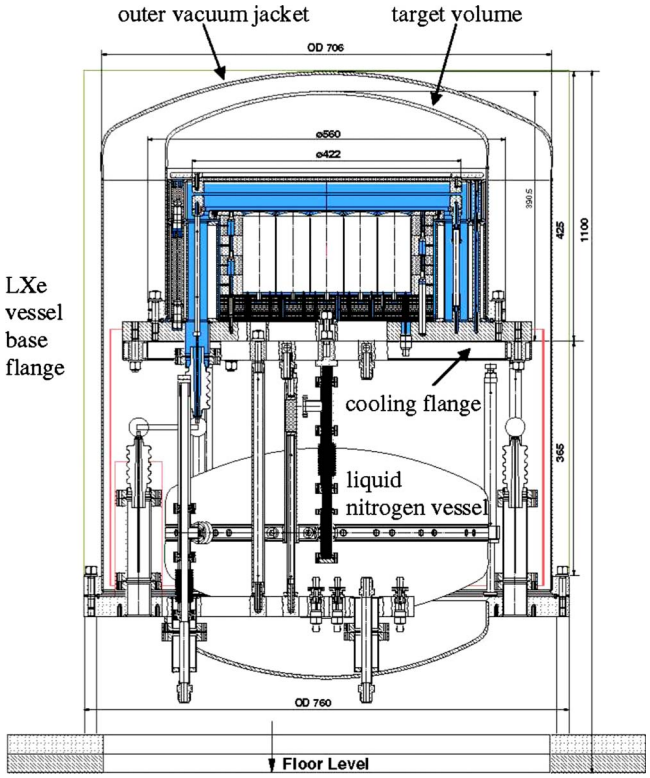

FIG. 61. (Color online) Schematic of the ZEPLIN III detector (Lebedenko, 2008).

mine. The radon-related wall events had not been anticipated at that time, and to remove these necessitated a quite severe software cut, reducing the mass to an inner 7 kg fiducial region and hence reducing the effective target mass and sensitivity by a factor of 4. Nevertheless, a 31 day run produced a (90%, two-sided) lower limit of zero and upper limit of ten signal events in a 50% efficiency event region between 5 and 15 keV, which translates into a dark matter cross section 90% upper limit (two-sided) of 7×10^{-7} pb at 60 GeV WIMP mass or a one-sided upper limit of 4×10^{-7} pb (Alner *et al.*, 2007).

Another detector based on the same two-phase TPC principle, but aiming at a lower energy threshold and higher field operation, was developed by the same collaboration in parallel with ZEPLIN II. The completed ZEPLIN III detector (see Fig. 61) was deployed underground in 2008. It uses a thin layer of liquid Xe (thickness 3.5 cm and diameter 38 cm) viewed by an array of 31×2 in. PMTs (ETL 730) immersed in the liquid, to achieve a light collection ~3 photoelectron/keV. In addition, a higher drift field (several kV/cm) can be used with the shallower target, producing a larger separation between the gamma and nuclear recoil populations (an overlap of only 0.1%, compared with 1% for ZEPLIN II). The fiducial mass, defined by the outer radius for which position reconstruction was possible, was 7 kg. The detector was set up in the same shielding system as that for ZEPLIN II. A three-month run produced seven events close to the edge of an otherwise empty 50% signal region between 2 and 12 keV. These events are compatible with the background and using a likelihood technique, a 90% two-sided WIMP cross-section limit of 7×10^{-8} pb was achieved (Lebedenko, 2008).

ZEPLIN III is being upgraded by the substitution of lower activity PMTs and by the addition of an active Gd-loaded hydrocarbon veto. The anticipated reduced background is expected to enable the background-free signal region to be increased from 50% to 70%, with a possible reduction in electron recoil energy threshold to 1.5 keV. A 1–2 year run should improve the ZEPLIN III WIMP cross-section sensitivity to 10^{-8} pb.

3. The LUX detector

The LUX experiment (Gaitskell, 2008) aims at deploying a 100 kg fiducial mass, two-phase XeTPC in a water shield to be constructed in the 4800 mwe Sandford Underground Laboratory of the Homestake Mine, in South Dakota. Homestake has been selected as the site for a Deep Underground Science and Engineering Laboratory (DUSEL) in the USA, currently under study. The LUX detector adopts the same principle as the other two-phase detectors but makes greater use of self-shielding to reduce the large background contributed by the PMTs in the fiducial region. 200 kg out of the 300 kg total mass is used for self-shielding. The TPC volume is viewed by 120 Hamamatsu R8778 PMTs, located above and below the target region (Fig. 62). This 2 in. diameter PMT was originally developed for the XMASS 100 kg prototype, discussed next. It features high quantum efficiency (>30%) and low radioactivity, compared to other VUV PMTs such as those used in ZEPLIN III, and can operate at LXe temperature.

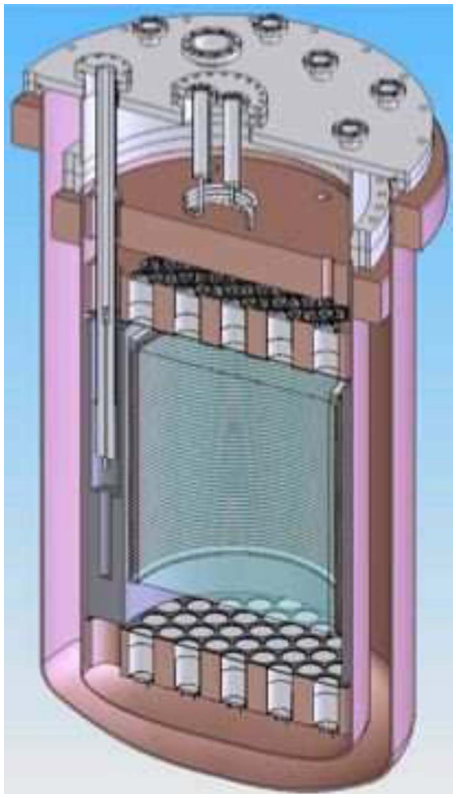

FIG. 62. (Color online) Schematic of the LUX detector (Gaitskell, 2008).

The goal of this experiment is to reach a WIMP cross-section sensitivity better than $\sim 7 \times 10^{-9}$ pb in 1 yr of operation. A 50 kg prototype with four PMTs has been built and is currently being tested above ground.

4. The XMASS detectors

The XMASS experiment proposed in 2000 aims at neutrinoless double beta decay, *pp*, and ^{7}Be solar neutrinos detection, in addition to dark matter direct detection, with a 10 ton LXe detector based solely on scintillation detection. The strategy is to use the excellent self-shielding capability of the liquid to achieve an effectively background-free inner volume. In the first phase of the XMASS program, a 100 kg prototype for dark matter detection was built and deployed at the Kamioka underground laboratory, in Japan.

The detector, in the form of a cube of 30 cm side, was contained in a low activity copper vessel, further shielded for gamma and neutron background reduction. To detect the scintillation of LXe, 54×2 in. low-background Hamamatsu R8778 PMTs were coupled to the copper vessel with MgF_2 windows. The PMT photocathode coverage was 17%. A picture of the PMT developed for XMASS is shown in Fig. 53, together with the other PMTs developed for XENON. Position reconstruction with a vertex resolution of ~6.5 cm for 10 keV events was demonstrated and used to reduce the gamma background from the PMTs activity. To reduce the ^{85}Kr contamination in Xe, a cryogenic distillation system was developed and successfully used to achieve a Kr/Xe level below 3 ppt (Abe *et al.*, 2008).

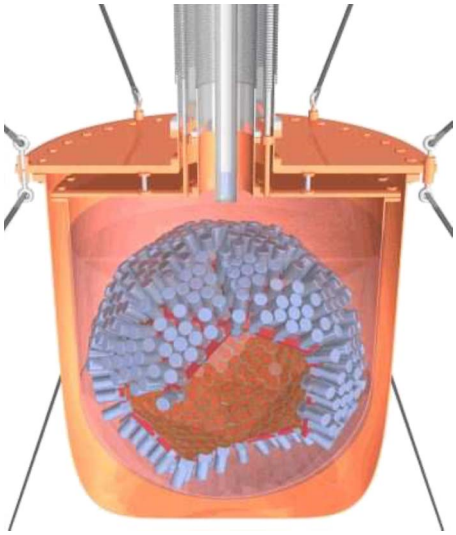

FIG. 63. (Color online) Schematic of the XMASS detector (Suzuki, 2008).

The second phase, currently under development (Suzuki, 2008), consists of a 857 kg LXe detector with the main physics goal of detecting dark matter (Fig. 63). The large liquid volume is viewed by 642 hexagonal PMTs (Fig. 64), arranged in an approximately spherical shape with 67% photocathode coverage of the inner surface of the detector. Simulations predict a light yield of 8 photoelectron/keV. If the new PMTs achieve their specification of a factor of 10 reduction in U/Th activity compared with their predecessors, the expected reduction in background events with radius should leave a central mass of 100 kg free of background, for at least a 1 yr running period. The experiment is installed in the new underground area in the Kamioka mine, inside a water shield to remove external gamma and neutron background. The projected WIMP-nucleon spin-

FIG. 64. (Color online) Photo of the hexagonal PMT of the XMASS detector.

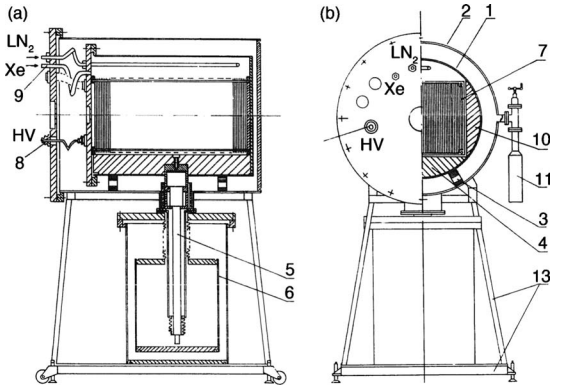

FIG. 65. Schematic of the Russian LXe ionization calorimeter. (a) and (b) Inner (1) and outer (2) cylindrical vessel, (3) multiplate supports, (4) and (10) aluminum segments, (5) copper bar, (6) cryostat with LN_2, (7) electrode system, (8) HV connector, (9) Xe gas supply tube, (11) zeolite trap (Baranov *et al.*, 1990).

independent cross section sensitivity is $\sim 10^{-9}$ pb for a running time of 5 yr. The advantage of a single phase detector such as XMASS, compared with the previously discussed two-phase detectors, is clearly the simpler design, but this comes at the expense of a large amount of nonfiducial liquid Xe. Without the diagnostic value of the ionization signal, the whole experiment relies on absolute suppression of both external and internal backgrounds.

C. Applications to particle physics

1. Prototypes of LXe ionization and scintillation calorimeters

Due to its high cost, LXe has not found widespread use in calorimeters for high-energy physics experiments despite the superior energy resolution and compact scale of a LXe ionization calorimeter, as discussed in Sec. III.A. Two prototypes have been built to date. The first was built by the Russian group (Baranov *et al.*, 1990) and is shown in Fig. 65. It is 25 cm in diameter and 50 cm in length. Two different electrode configurations were tested, one a multiplate type for energy measurement, and the other consisting of strip electrodes for position measurement. Figure 66 compares measured results with a Monte Carlo simulation. The measured resolutions in the range 1–6 GeV were $\sigma_E/E = 3.4/E^{0.5}\%$ for energy and $\sigma_x/E = 4.6/E^{0.5}$ mm for position, with E in GeV.

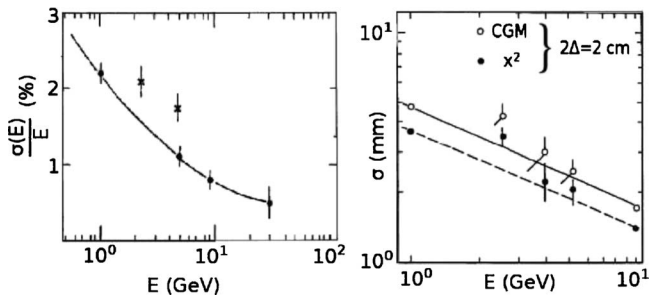

FIG. 66. Energy and position resolution performance of the Russian LXe ionization calorimeter. (Left) Energy resolution dependence on electron energy. Crosses are the experimental points and circles are points from Monte Carlo simulations. (Right) Position resolution dependence on electron energy based on two different reconstruction algorithms. Full and open circles are data for two different position reconstruction algorithms, and the dashed and solid lines the corresponding predictions from simulation (Baranov *et al.*, 1990).

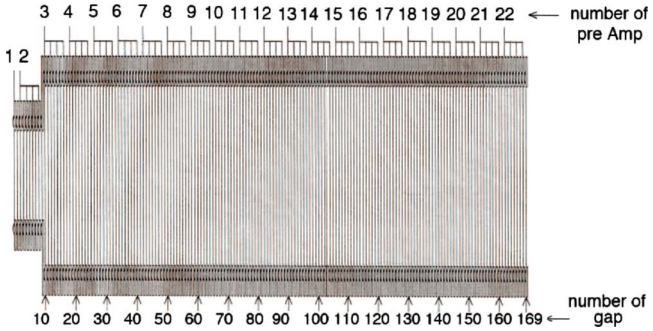

FIG. 67. (Color online) Schematic of the Waseda multiplate LXe ionization calorimeter (Okada *et al.*, 2000).

The second homogeneous liquid Xe calorimeter prototype was built by the Waseda group (Okada *et al.*, 2000) and tested in a high-energy electron beam at CERN. Figure 67 shows the electrode system, consisting of 169 cells and their readout arrangement. An energy resolution of 0.9% (1σ) was measured with 70 GeV electrons, close to the simulated value of 0.7%.

In 1988, a LXe scintillation calorimeter with fast response, excellent energy and position resolutions, and high radiation resistance was proposed (Chen *et al.*, 1988) for an experiment at the Superconducting Super Collider (SSC), under discussion at that time. The design (Radermacher *et al.*, 1992) included a long barrel homogeneous calorimeter and two end-cap sampling calorimeters.

A full length (66 cm) LXe prototype cell with a volume of 4 l was built to investigate the light collection uniformity in the homogeneous section of the calorimeter (see Fig. 68). The cell walls, made of MgF_2-coated Al, were used as UV reflectors with 85–90 % reflectivity. Three large area, UV-sensitive, Si photodiodes with mesh type surface electrode detected the LXe scintillation (Kashiwagi *et al.*, 1993).

To achieve sufficient longitudinal uniformity, the cell had a tapered shape for a focusing effect, in addition to using small light collimators in the form of grids coated with Al, placed in front of the photodiodes. The relative light collection uniformity was measured with such LXe cell, using cosmic-ray muons and alpha particles. The results are shown in Fig. 69 (Chen *et al.*, 1993). Good uniformity was obtained at the expense, however, of a drastic reduction in number of photons collected. As a result, the energy resolution estimated from Monte Carlo simulations (Chen *et al.*, 1993) was about 0.5% (1σ) for energies above 50 GeV, almost the same as that of a LAr calorimeter (Doke *et al.*, 1985).

At the same time, the MIT-ITEP-Dubna Collaboration constructed a full-scale prototype of a 75 l LXe

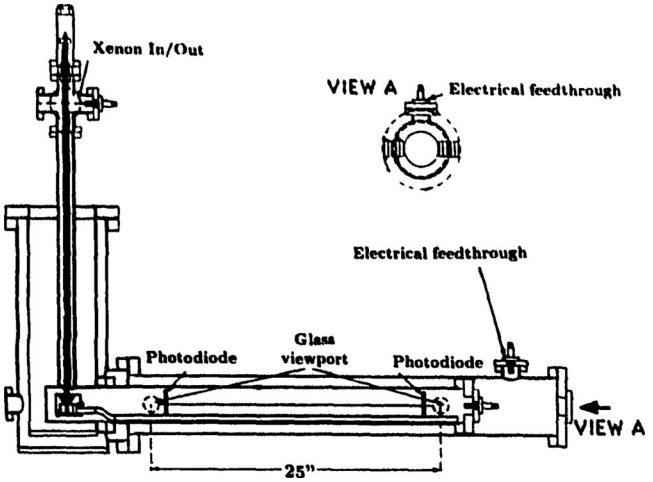

FIG. 68. Schematic of a full length liquid xenon cell for light collection uniformity tests (Chen *et al.*, 1993).

scintillation calorimeter, consisting of 45 unit cells (Akimov *et al.*, 1996).

The walls of each unit cell were partly coated with strips of wavelength shifter (p-therphenyl) to convert the vuv light to visible light (Akimov *et al.*, 1995, 1996) and the silicon photodiodes were replaced with PMTs. Figure 70 shows a schematic of the unit cell and of the full calorimeter reflector structure (Akimov *et al.*, 1995).

The best energy resolution achieved with this prototype was 7.5% (1σ) for 348 MeV electrons, with an energy dependence $\Delta E/E=5/\sqrt{E}\%$, where E (GeV) is the incident electron energy. This energy resolution was not as good as that typical of the liquid xenon ionization calorimeter discussed above. In subsequent years, much improvement was achieved as a result of new developments in photodetectors for the Xe vuv light, which could be operated directly in the liquid. In the following we discuss two experiments dedicated to two rare processes expected from new physics beyond the standard model (SM) of particle physics.

2. The RAPID detector for $\pi\rightarrow\mu\nu\gamma$ decay

In the early 1990s a LXeTPC based on ionization and scintillation light was developed by the Padova Univer-

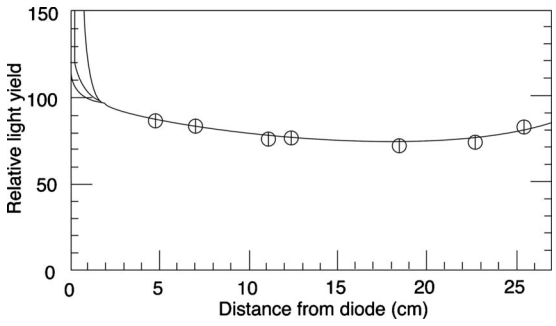

FIG. 69. Relative light yield as a function of the distance from the Si photodiode, measured with cosmic-ray muons. Monte Carlo curves are shown for different light collimators (Chen *et al.*, 1993).

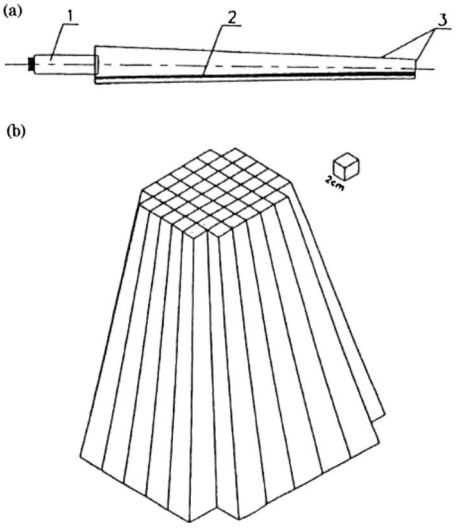

FIG. 70. Schematic of the MIT-ITEP-Dubna LXe scintillation calorimeter. (a) Unit cell of the calorimeter: 1, PMT; 2, fragment of p-terphenyl strip; 3, Mylar reflector. (b) Assembly of the full calorimeter reflector structure (Akimov *et al.*, 1995).

sity group for detection of gamma rays from the rare $\pi\rightarrow\mu\nu\gamma$ decay (Brown and Bludman, 1964; Bressi *et al.*, 1998). The gamma rays can be emitted either from the charged pion and muon [this term is called internal bremsstrahlung (IB)] or directly from the decay vertex due to the composite nature of the pion [structure-dependent (SD) term]. When squaring the decay matrix to get the decay probability, an interference term (INT) appears, which is proportional to SD$\times$IB. The IB term is a pure QED term, well described and calculable within the frame of this theory. The SD term takes into account the fact that the pion is not an elementary particle but is constituted by quarks. In the pion to muon radiative decay, however, both the SD term and the INT term are heavily suppressed compared to the IB term. To a good approximation, the gamma rays emitted from this decay can be thought of as a pure QED process. QED calculations show that for a pion decay at rest the gamma spectrum is strongly peaked at zero, falling approximately as $1/E_\gamma$ up to the maximum energy of 30 MeV. The goal of the RAPID experiment was to measure the energy of both the muon and the gamma produced in the decay, in order to obtain not only the branching ratio but also the full two-dimensional distribution. For the detection of the gamma ray, LXe was recognized as an optimum medium and an ionization TPC with a 38 l sensitive volume, self-triggered by the scintillation light was adopted to achieve low-energy threshold, high detection efficiency, and good energy resolution. The TPC, shown in Figure 71, is described in detail by Carugno *et al.* (1996). It consists of a 64 l cylindrical vessel, with a gamma-ray entrance window made of one 1-mm-thick titanium and 12 quartz windows for the detection of the scintillation light with vuv-sensitive PMTs. The electrode structure, for the detection of the ionization signal, consists of six drift regions, each 6.3 cm long with a shielding grid at 3 mm from the an-

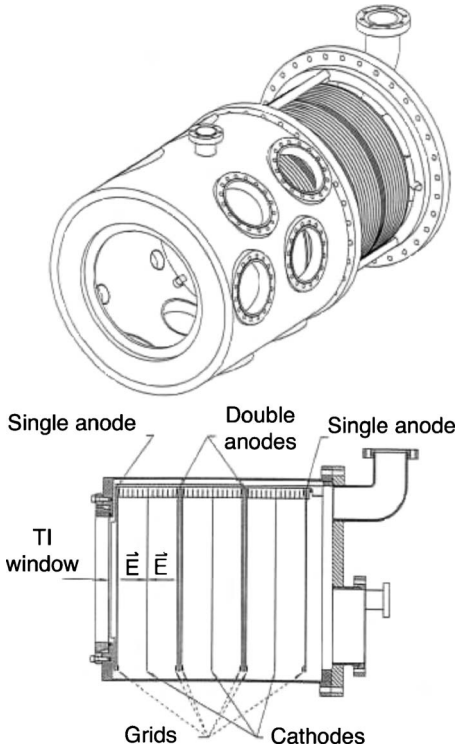

FIG. 71. Schematic of the RAPID LXeTPC. TPC vessel with Ti window for incident γ rays and quartz windows for PMTs (top) Cross section of the electrodes for charge readout (bottom) (Bressi *et al.*, 1998).

ode. With an applied electric field of 0.5 kV/cm, the energy threshold achieved was 230 keV. This was the first large volume TPC successfully implemented for a physics experiment and the first to address the demanding requirement of high purity of the liquid for charge drift and a long-term stability of the charge yield. The Padova group successfully implemented cleaning and purification procedures, including continuous recirculation of Xe gas through hot metal getters by means of a clean circulation pump. An electron lifetime in excess of milliseconds was achieved and the TPC response was stable for a period of two months. The energy resolution obtained with this detector was about 7% (1σ) at 1 MeV:

$$\frac{\sigma(E_\gamma)}{E_\gamma} = \frac{7\%}{\sqrt{E_\gamma}} \oplus \frac{0.14\ \text{MeV}}{E_\gamma}, \tag{24}$$

where E_γ is in MeV and $\oplus$ indicates a quadratic sum. Despite the high detection threshold and the large low-energy gamma-ray background, the branching ratio for gamma rays of energy larger than 1 MeV was measured to be $2.0\times10^{-4}\pm12\%(\text{stat})+4\%(\text{syst})$, in good agreement with the theoretical QED expectation (Bressi *et al.*, 1998).

3. The MEG detector for $\mu\to e\gamma$ decay

Lepton flavor violation is predicted in supersymmetric grand unified theories (SUSY-GUTs) at a measurable level. The rare $\mu\to e\gamma$ decay is the most promising lepton flavor violating process, with a predicted branching

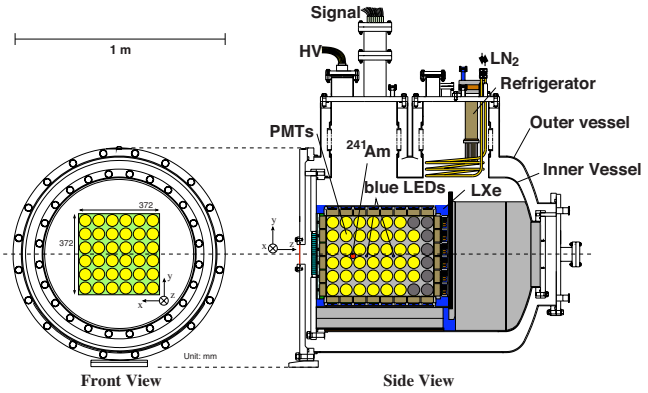

FIG. 72. (Color online) Schematic of the large MEG prototype (Mihara, 2004).

ratio above 10^{-14} (Orito and Mori, 1997). The first and present experimental upper limit to this branching ratio was reported in 1999 at a level of 1.2×10^{-11} (Brooks *et al.*, 1999). In the same year, an experiment capable to improve on this limit by at least two orders of magnitude was proposed (PSI, 1999), based on the original suggestion by Doke to use a position sensitive LXe scintillating calorimeter, with excellent energy and position resolution, later to be known as the MEG detector (Baldini *et al.*, 2002). A $\mu\to e\gamma$ decay event is characterized by the clear two-body final state where the decay positron and the gamma ray are emitted in opposite directions with energies equal to half the muon mass ($E=52.8$ MeV). While positrons of this energy are abundant from the standard Michel decays of muons, gamma rays with such high energies are very rare. Therefore the key requirement for the MEG detector is high-energy resolution for gamma rays since the accidental background rate decreases at least with the square of the energy resolution (Baldini *et al.*, 2002; PSI, 1999).

The excellent properties of LXe as scintillator and the developments of new PMTs with high quantum efficiency, fast timing, and their possible operation in LXe motivated the choice of the detector for the MEG experiment. With the Xe scintillation light detected by a large number of PMTs immersed in the liquid volume, the detector's energy resolution is proportional to $1/\sqrt{N_{pe}}$, where N_{pe} is the number of photoelectrons, and was estimated to be better than 1% (1σ) for 52.8 MeV gamma rays (Doke and Masuda, 1999). In addition, the gamma-ray interaction points can also be determined from the light distribution on individual PMTs (Orito and Mori, 1997). Following the R&D with a small prototype (Mihara *et al.*, 2002) and with further improvement of the metal channel type PMT, a large LXe prototype (68.6 l) with 228×2 in. PMTs was constructed and tested with gamma rays of 10 to 83 MeV (Mihara, 2004). The prototype and associated cooling and purification apparatus, shown schematically in Fig. 72, were tested at the Paul Scherrer Institute in Switzerland, where the final MEG experiment is located. In this prototype, a PTR was first used to condense Xe gas and maintain the liquid temperature stable over long periods

of time. The PTR, optimized for liquid xenon, had a cooling power of 189 W at 165 K (Haruyama *et al.*, 2004).

This prototype was large enough to test both the reliability and stability of the cryogenics system based on the PTR and the efficiency of the purification system required for the calorimeter's performance. The study of the impact of impurities on Xe scintillation light transmission was particularly important and valuable to later LXe detectors, such as those developed for dark matter searches discussed earlier. While the transmission of the scintillation light is also affected by Rayleigh scattering, this process does not cause any loss of light and hence does not affect the energy resolution. Two types of purification systems were developed for studies with this prototype. One is a gaseous purification system where liquid xenon is evaporated, purified by a heated metal getter, and then liquefied back in the cryostat (Mihara *et al.*, 2004). This method is effective in removing all types of impurities but not efficient since the purification speed is limited by the cooling power. The other method was developed specifically to remove water, which was identified as the major contributor to light absorption, at a much higher rate (100 l/h) by circulating the LXe with a cryogenic centrifugal pump. Water is efficiently removed by a filter containing molecular sieves. Using this method, the total impurity concentration was reduced in 5 h from 250 ppb to 40 ppb in the total 100 l LXe volume of the MEG prototype (Mihara *et al.*, 2006).

Novel calibration and monitoring techniques have also been developed with this prototype study. In particular, a lattice of radioactive point sources was developed by permanently suspending in the active volume (100 μm diameter) gold-plated tungsten wires carrying a small amount of ^{241}Am (Baldini *et al.*, 2006). This method was successfully implemented and used to determine the relative quantum efficiencies of all PMTs and monitor the stability of the detector during the experiment. In the final MEG detector, the PMT configuration is similar to that tested in the prototype, hence the methods of reconstructing the gamma-ray energy and interaction points were proven with the prototype. The reconstructed energy distribution for 55 MeV gamma rays

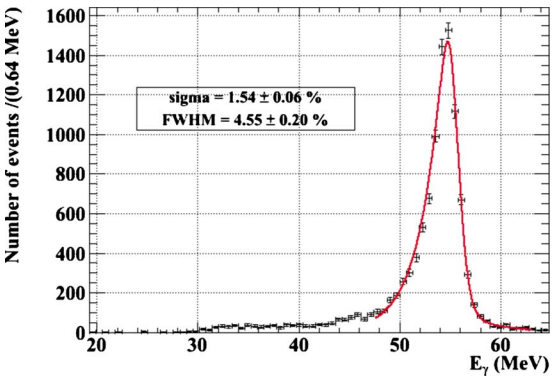

FIG. 73. (Color online) Energy spectrum for 55 MeV gamma rays measured with the large MEG prototype (Baldini *et al.*, 2005).

TABLE VII. Basic parameters of the liquid xenon scintillation calorimeter for the MEG experiment.

Inner radius of the vessel	634 cm
Outer radius of the vessel	1104 cm
Acceptance angle	±60°
Volume of liquid xenon	0.9 m^3
Number of photomultipliers	846
Total mass of PMTs with their holders	450 kg
Weight of the vessel	2.7 tons
Total weight of the calorimeter	6 tons

from π^0 decay is shown in Figure 73 (Baldini *et al.*, 2005; Ootani, 2005; Sawada *et al.*, 2007). The spectrum is asymmetric with a low-energy tail caused mainly by gamma-ray interactions with materials in front of the sensitive region and by the leakage of shower components. The energy resolution of 1.54±0.6% is roughly equal to the value obtained by extrapolation of the small prototype data. The events remaining above 55 MeV are known to be due to mistagging of π^0 events. The position and time resolutions are evaluated to be 5 mm and ~120 ps (FWHM), respectively (Baldini *et al.*, 2006).

The MEG cryostat, consisting of cold and warm vessels, is designed to reduce passive materials at the gamma-ray entrance. The same PTR tested on the prototype will be used for cooling, with an emergency cooling system based on liquid nitrogen flowing through pipes installed both inside the cold vessel and on its outer warm vessel. Gaseous and liquid purification systems are located on site for removing impurities possibly retained after liquefaction. Table VII shows the basic parameters of the LXe scintillation calorimeter for the MEG experiment. The construction of the calorimeter was completed in 2007. Calibration started the same year and physics data taking continues to date. MEG (Fig. 74), with a total LXe volume of almost 2.7 tons and about 850 PMTs is currently the largest LXe detector in operation worldwide.

4. The EXO detector for $0\nu\beta\beta$ decay of ^{136}Xe

A key topic in particle physics is the nature of neutrinos, their relationship to the charged leptons, and their mass. Oscillation experiments have confirmed mixing between the three neutrino types, from which mass differences can be estimated. The absolute mass of the neutrino remains unknown but is now expected to be in the region 0.01–0.1 eV (Avignone, King, and Zdesenko, 2005). If neutrinos are Majorana in nature, i.e., they are their own antiparticle, the absolute mass scale can be determined by observations of nuclei which undergo double beta decay ($2\nu\beta\beta$), a decay with the emission of two electrons and two neutrinos. As Majorana particles, they can also decay into two electrons without emitting neutrinos, giving a signal at a single well-defined energy. One such nucleus is ^{136}Xe, an 8% constituent of natural Xe. Enrichment by centrifuging allows to increase this

FIG. 74. (Color online) Photo of the full scale MEG LXe scintillation calorimeter.

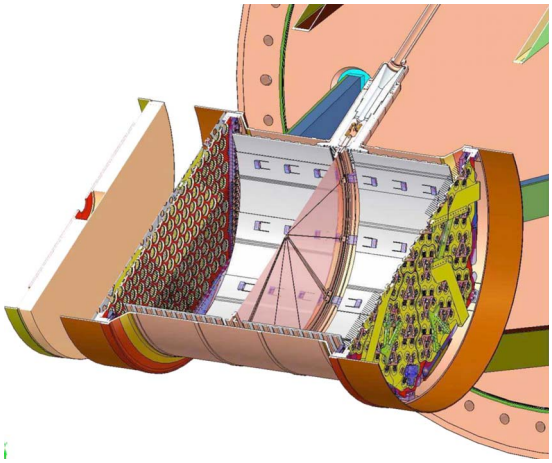

FIG. 75. (Color online) Schematic of the EXO-200 TPC (Gratta, 2009). The length of the TPC as well as the diameter of the TPC planes are 40 cm.

fraction to at least 80%. Neutrinoless double beta decay of ^{136}Xe will occur at an energy of 2479 keV, at a rate which depends on the square of the neutrino mass scale. Hence observations of this mode of decay could fix the neutrino mass scale for the first time. The sensitivity of such experiments is quoted as the reciprocal of the decay rate or as the lifetime of the observed decay in years. For the expected neutrino mass range of 0.01–0.1 eV, the lifetime would be in the region of 10^{27}–10^{28} yr, which in the case of ^{136}Xe requires 1–10 tons of that isotope for observation of a few events in 1–2 yr.

The experimental effort using LXe to search for the $0\nu\beta\beta$ decay of ^{136}Xe was pioneered more than 20 years ago by Barabanov *et al.* (1986). A small detector filled with ^{136}Xe enriched LXe was used by Bernabei *et al.* (2002). The EXO experiment plans to reach the multiton level in two stages, the first of which is EXO-200, a 0.2 ton prototype. Although the search is for a signal at a single specific energy, it is necessary to have excellent energy resolution to separate this signal from the tail of the $2\nu\beta\beta$ decay spectrum, for which the $0\nu\beta\beta$ line is at the end point. As discussed in Sec. III.E, the simultaneous detection of ionization and scintillation promises the best energy resolution for LXe detector, hence the EXO-200 experiment is baselined on a liquid xenon time projection chamber (LXeTPC) with detection of both charge and light signals. To minimize instrumental background, the cryostat is made from a double wall of selected low activity copper, inside a 25-cm-thick lead enclosure for gamma shielding, and located in the underground site of the Waste Isolation Pilot Plant (WIPP), at a depth of 2000 mwe to minimize muon-induced background. All components used in the EXO-200 have been qualified for low radioactivity with a variety of techniques (Leonard *et al.*, 2008). The cold vessel of the cryostat is cooled with heat exchangers fed by three industrial refrigerators, together capable of 4.5 kW at 170 K. The system offers double redundancy without the use of liquid nitrogen, discouraged at the underground site for safety reasons. Xe is recirculated and purified in the gas phase by hot metal getters, with a custom-built pump, a Xe heater and condenser, cooled by a fourth refrigerator that is also used by a radon trap. A control system maintains the pressure difference across the thin TPC vessel to less than 0.3 bar. The TPC vessel (see Fig. 75) is shaped to minimize dead volumes and hence to make efficient use of the enriched Xe which will be ultimately used, after testing with natural Xe. The drift region, designed to support up to 75 kV with a central cathode plane, is defined by field shaping rings. About 150 kg of Xe are in a fiducial region, where the field is sufficiently uniform and the background sufficiently low for the rare event search. Each end of the cylindrical vessel flares out radially to make space for two wire grids for XY position reconstruction (see Fig. 76). An array of about 250 large area avalanche photodiodes [LAAPDs (Neilson *et al.*, 2009)], mounted on a platter behind the grids, is used to read out the Xe light. Based on Monte Carlo simulations, the overall light detection efficiency is between 15% and 20%, depending on event position in the volume. The readout electronics, for the charge induction and collection wires and for the light sensors, is located outside the lead shielding. The EXO-200 TPC is in the final stages of assembly in a clean room at Stanford, while the support and cryogenic systems are being commissioned underground. It is expected that an engineering run, with natural Xe, has started in 2009 to be followed by a science run with enriched ^{136}Xe. For an estimated energy resolution of $\sim$1.6% (1σ) at the 2.5 MeV end-point energy and with the estimated overall background, the sensitivity of this prototype to the $0\nu\beta\beta$ lifetime is projected as 6.4×10^{25} yr (90% confi-

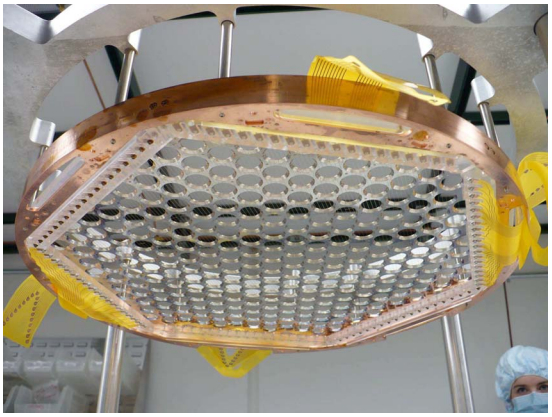

FIG. 76. (Color online) Photo of one EXO-200 anode plane. Induction and charge collection grids cross at 120°. The LAAPD support platter is visible behind the grids (Gratta, 2009).

dence) after two years of data taking. This corresponds to an effective Majorana mass of the neutrino of 0.13 (0.19) eV depending on the nuclear matrix models. EXO-200 should also be able to gather information on the $\nu\nu\beta\beta$ decay, which has not yet been detected.

The required increase in sensitivity to the level of 10^{27}–10^{28} yr to match the expected Majorana mass level, can in principle be achieved with the same technique by increasing the detector mass to the 10 tons level. However, production of enriched xenon requires about an order of magnitude more xenon to start with. Given that the world production is only about 30 tons of xenon per year, it is clear that the procurement of such large amounts of xenon enriched in ^{136}Xe poses a major challenge for the realization of these experiments.

A more positive signal identification can be obtained by the detection of the Ba^{2+} ion to which the ^{136}Xe decays, in coincidence with the electron ionization signal. This was first suggested by Miyajima *et al.* (1974). Individual atoms of ^{136}Ba may be detected using fluorescent spectrometry with laser excitation. Different methods for extraction of ions from liquid xenon have been considered by the EXO Collaboration, including the use of a cryotip or an optical fiber tip, both of which have stringent technical requirements (Sullivan *et al.*, 2007). EXO-200 will not test the Ba tagging method.

An alternative approach has been recently proposed by Arisaka *et al.* (2009) with the ^{136}Xe-Ar-$^{129/131}$Xe (XAX) detector concept, which combines dark matter detection with $0\nu\beta\beta$ decay and includes a concentric arrangement of <5 tons enriched ^{136}Xe surrounded by 5 tons depleted Xe ($^{129/131}$Xe) which provides simultaneously a dark matter target and shielding for the $0\nu\beta\beta$ decay target. The $^{129/131}$Xe also provides a *pp* solar neutrino detector, free from the $2\nu\beta\beta$ decay background in natural Xe. A separate Ar detector is proposed as a comparison target for dark matter signals. Background studies for this scheme indicate that the $0\nu\beta\beta$ decay sensitivity would be competitive with the EXO scheme without the need for the complex Ba tagging.

D. Applications to medical imaging

The excellent properties of liquid xenon for gamma-ray detection make it also attractive for single photon emission computed tomography (SPECT) and positron emission tomography (PET), the two primary modalities in use for functional medical imaging. The large majority of SPECT and PET systems in use today are based on crystal scintillators as detection media. The first application of liquid xenon for SPECT (Zaklad *et al.*, 1972) used a multiwire proportional counter with a position resolution of 4 mm FWHM. However, the counter suffered significant instabilities precluding its use as a practical gamma camera. In 1983, Egorov *et al.* constructed a gamma camera using electroluminescence emission in high-pressure xenon gas. An intrinsic spatial resolution of 3.5 mm (FWHM) and an energy resolution of 15% (FWHM) for 122 keV gamma rays were obtained (Egorov *et al.*, 1983).

Most of the subsequent R&D on liquid xenon detectors for medical imaging has focused on PET systems, with two approaches: (1) detectors which measure the energy and location of gamma rays from the ionization signal, with the scintillation signal used only as an event trigger, and (2) detectors which use only the scintillation signal to measure the energy and location of gamma rays. We discuss recent developments in both approaches. While it will be clear that using all features of LXe (good energy resolution from combined ionization and light, high spatial resolution, and Compton reconstruction) in a high rate high sensitivity PET system is potentially important for medical imaging, there are several practical issues such as cost, safety, complexity compared to conventional systems, plus the added requirement to produce fast images, complicated by the Compton reconstruction, which will require additional studies before this technology is accepted for such applications.

1. LXe Compton PET

The principle of a PET system as diagnostic tool in medicine is to infer the location of a tumor from the measurement of the 3D location of a radiotracer previously injected into the patient and labeled with positron emitting nuclides, such as ^{11}C, ^{13}N, ^{15}O, or ^{18}F. The emitted positrons slow down in the surrounding patient's tissue annihilating with atomic electrons to give two back-to-back 511 keV annihilation photons. The annihilation occurs within a few millimeters from the positron source. By detecting the two photons in coincidence and the coordinates of their interaction points in a detector, it is possible to define a line along which the positron emitting source is located in the patient. A set of such intersecting lines allows 3D reconstruction of the source. Thus the main requirements for a PET detector are the following: (a) high photon detection efficiency (~80% for each 511 keV gamma), (b) position resolution of a few millimeters, (c) time resolution to reduce the rate of false coincidences, (d) good energy resolution

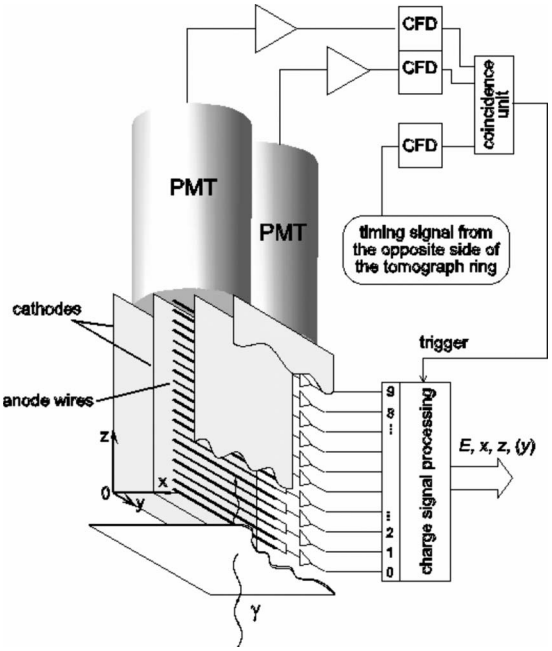

FIG. 77. Schematic of the Coimbra PET prototype (Chepel *et al.*, 2001).

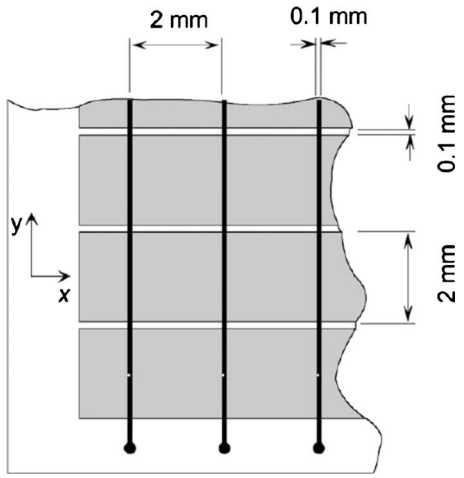

FIG. 78. The ministrip plate of the Coimbra PET prototype (Solovov *et al.*, 2002a).

(<100 keV FWHM) to discriminate photons scattered in the patient, and (e) a high count rate capability ($\sim 10^5$–10^6 s^{-1}/cm^2 of detecting surface).

A LXe based PET detector should be able to improve on the energy and position resolution currently achieved with commercial whole-body PET scanners based on crystal scintillators. The scintillation of LXe is also faster than that from most crystal scintillators, allowing time-of-flight measurement, as discussed later. In a typical high Z, high density detector medium, the 511 keV gamma rays interact predominantly via Compton scattering, i.e., the energy is deposited in one or more interaction points before the gamma ray is photoabsorbed. The interaction points are too close to be resolved and the average location is taken approximately as the first interaction point, which is then the only point on the original gamma-ray trajectory.

If the detector is a LXeTPC such as the one discussed in Sec. IV.A.1, the combined measurement of spatial coordinates and energy loss in each interaction point allows one to use Compton kinematics to determine the sequence of interactions (compare Fig. 7). With the first interaction point known, the lower Z and density of LXe compared to typical crystal scintillators used in PET are no longer a disadvantage.

The first idea of using a LXeTPC for PET was proposed in 1993 by Chepel with subsequent R&D documentation (Chepel *et al.*, 1994, 1995, 1997, 1999, 2001; Lopes *et al.*, 1995; Crespo *et al.*, 1998, 2000). The setup used for the tests of this first Compton PET is schematically shown in Fig. 77. The detector was a LXe multiwire detector consisting of six ionization cells, each formed by two parallel cathode plates with a multiwire anode in the middle. Negative voltage is applied to the cathode, with the anode wires (50 μm diameter and 2.5 mm spacing) at ground. The 20 anode wires were connected in pairs to reduce the number of readout channels. The signal from each charge channel was fed to a low-noise charge-sensitive preamplifier followed by a linear amplifier, connected to a leading edge discriminator and a peak-sensing analog-to-digital converter (ADC). A typical noise level of 800 electrons FWHM was achieved for the charge readout.

The scintillation light produced in the active LXe filling the cell was detected by two Hamamastu R1668 PMTs, coupled to the cell through quartz windows. For each PMT, the fast signal from the last dynode was fed into a constant fraction discriminator (CFD) for triggering and the anode signal was amplified and shaped for measuring the light amplitude. The X coordinate of the interaction point is determined with a precision better than 1 mm (1σ) by measuring the electron drift time triggered by the light signal. The identification of the pair of wires on which the charge is collected gives the depth of the interaction (Z coordinate), with a resolution estimated at 2–5 mm (1σ). For measurement of the Y coordinate, at first the ratio of the amplitudes of the two PMTs was used but the position resolution was only $\sim$10 mm (1σ). To improve this resolution by about a factor of 10, the use of a ministrip plate (Fig. 78) was considered (Solovov *et al.*, 2002a), and several tests for this electrode system were conducted. However, to our knowledge this position resolution has not yet been achieved for 511 keV gamma rays although a multistrip ionization chamber was tested with 122 keV gamma rays, obtaining a position resolution of <2 mm (1σ) (Solovov *et al.*, 2002b, 2003).

Recently two new groups have undertaken further R&D towards this challenge, the Nantes-Subatech group in France (Duval *et al.*, 2009) and the Columbia group (Giboni *et al.*, 2007). While single point position resolution is an important parameter of a LXe detector, for PET the double point resolution, i.e., the minimum distance required between two sources to be still separated in the image, is also important. As discussed by

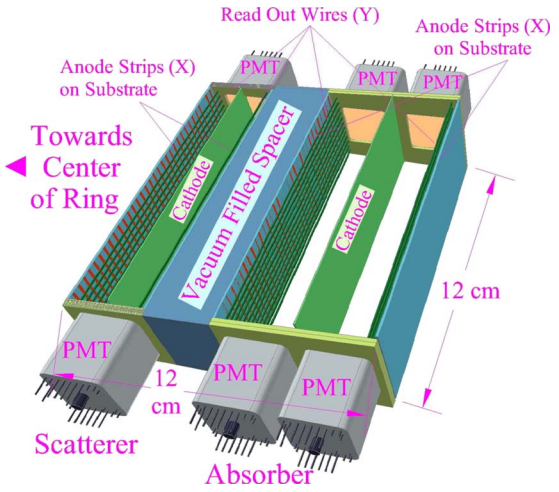

FIG. 79. (Color online) Schematic of the Columbia LXe Compton PET unit cell (Giboni *et al.*, 2007).

Giboni *et al.* (2007), this double point resolution depends not only on position resolution but also on statistics of events from the sources, as well as on the background from unrelated events. In an image, these factors determine the contrast besides the background from wrong Compton sequencing. There is a very strong background from genuine positron annihilation events with at least one gamma-ray Compton scattering even before leaving the patient. Most of these scatters are very forward, with a small angle to the original direction, and with only a small change in gamma-ray energy.

To identify and reject this background as far as possible, energy resolution is by far the most important factor. Giboni *et al.* (2007) proposed the LXe TPC as Compton PET (see Figs. 79 and 80) which relies on the improved energy resolution that results from the sum of the anticorrelated ionization and scintillation signals demonstrated by Aprile *et al.* (2007a). The estimated FWHM energy resolution of 4% must be compared with 15% and 25% for present GSO and BGO crystal scintillators.

Efficient light detection with PMTs immersed in the LXe helps not only the energy resolution but also provides good coincidence timing. Giboni *et al.* (2005) measured a timing resolution of about 270 ps for 511 keV gamma rays in LXe. This might not yet be sufficient for a pure TOF-PET but is sufficient for TOF-assisted PET. Compton kinematics not only determines the sequence of interaction points but also constrains the direction of the incoming photon to the surface of a cone. The opening angle of the cone is the Compton scattering angle in the first interaction point. If the incoming directions are thus determined for both annihilation gamma rays, even if one of the gamma rays scatters within the body, one can still determine the original line on which the annihilation gamma rays were emitted. The number of events with one of the gamma rays scattering once in the body amounts to about twice the number of nonscattered events. Therefore, with Compton reconstruction, the number of acceptable events is nearly a factor of 3 larger than the number of good events in a standard PET detector (Giboni *et al.*, 2007). This increased detection efficiency results in a reduction in the radiation dose for the patient.

The approach used by the Nantes-Subatech group uses a microstructure pattern readout for the charge and a gaseous photomultiplier (GPM) (Breskin *et al.*, 2009) for the light signal. The aim is to achieve an energy resolution similar to that of Aprile *et al.* (2005) and a $\sigma_x \sim \sigma_y \sim \sigma_z \leqslant 0.1$ mm position resolution, in order to reconstruct the incident angle of the 511 keV gamma rays with an angular resolution less than 2° (1σ). Moreover, another medical imaging technique has been proposed by the same group (Grignon *et al.*, 2007), aimed at reducing the examination time and the radiation dose for the patient. This technique is based on precise location in organs of a three-photon emitter (^{44}Sc). The method would provide high-resolution imaging by combining the information from a PET with the direction cone defined by a third gamma ray. The first LXe Compton telescope prototype has been built and is under testing. It features

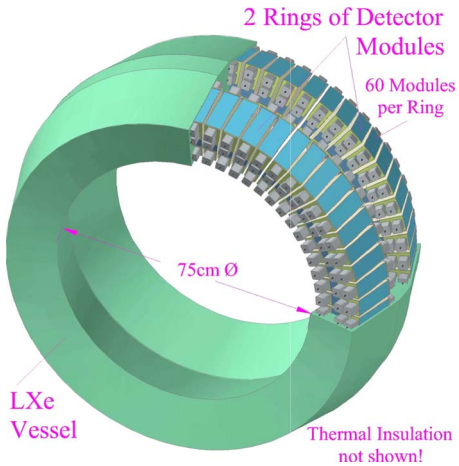

FIG. 80. (Color online) Schematic of the Columbia full scale LXe Compton PET (Giboni *et al.*, 2007).

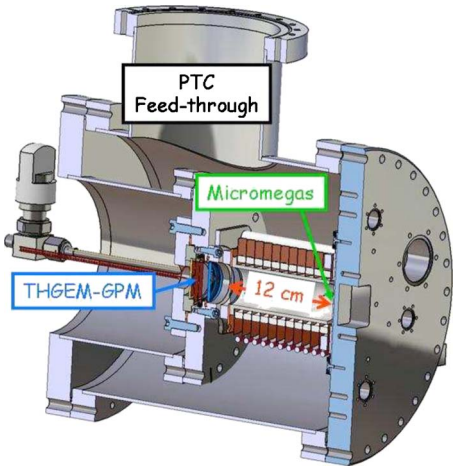

FIG. 81. (Color online) Schematic of the Nantes LXe Compton PET prototype (Grignon *et al.*, 2007).

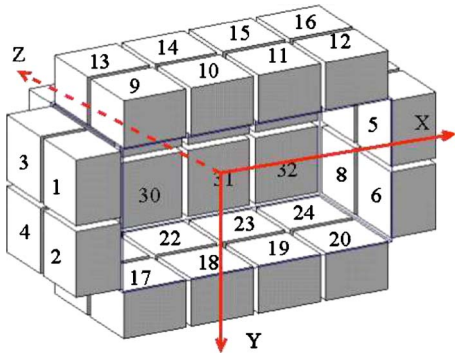

FIG. 82. (Color online) Arrangement of 32 PMTs in Waseda TOF PET prototype (Nishikido *et al.*, 2004).

a $3\times3\times12$ cm^3 active volume (Fig. 81). The LXe cryogenics are controlled by a dedicated pulse tube cryocooler (Haruyama *et al.*, 2004), the same machine used on the XENON100 and MEG experiments. First results are promising, demonstrating the first complete collection of the ionization electrons using a so-called micromegas detector, fully immersed in LXe (Giomataris *et al.*, 1996). The scintillation signal has been so far detected by a standard PMT to be replaced by a GPM (Breskin *et al.*, 2009).

2. LXe TOF PET

The possibility of a TOF PET, based on the excellent properties of LXe as scintillator, was first suggested by Lavoie (1976), and the study of this type of PET was carried out in 1997 by the Waseda group. A prototype, consisting of two LXe chambers, was constructed in 2000. In its initial implementation, each chamber has a LXe sensitive volume of $120\times60\times60$ mm^3 viewed by only 32×1 in. PMTs, with one side left uncovered as an entrance window for gamma rays (Fig. 82). A schematic of the whole assembly is shown in Fig. 83. The distance between the entrance planes is 70 cm. Testing began in 2001 (Nishikido *et al.*, 2004), and soon thereafter improved PMTs became available and were used in the

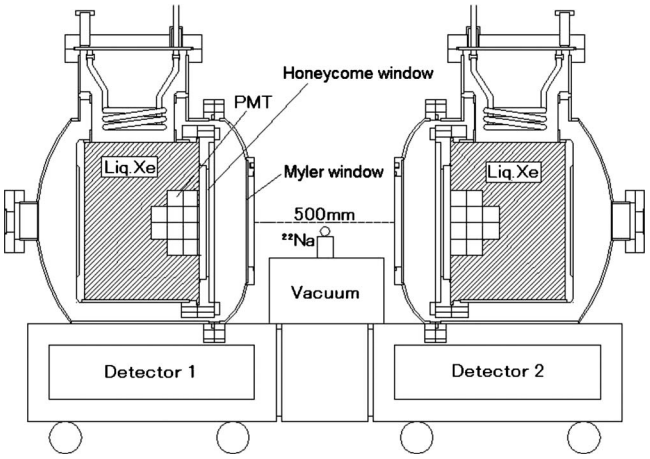

FIG. 83. Schematic of the Waseda TOF PET prototype (Nishikido *et al.*, 2004).

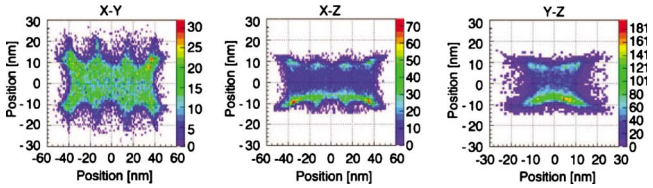

FIG. 84. (Color online) Spatial distributions of 511 keV interaction points reconstructed with the Waseda prototype (Doke, Kikuchi, and Nishikido, 2006).

prototype (Nishikido *et al.*, 2005). Testing of the prototype with the new PMTs was carried out with a ^{22}Na source placed in the center of the setup. The output signals from the 32 PMTs of each chamber were recorded by charge-sensitive analog-to-digital converters (QADCs), and the TOF information was recorded with time-to-digital converters (TDCs). The position of a gamma-ray interaction was determined by the time of flight of the gamma ray to the PMTs. The position distributions of interaction points in *X-Y*, *X-Z*, and *X-Z* planes inside the sensitive volume, reconstructed with this method, are shown in Fig. 84.

The energy resolution obtained from the sum of 32 PMTs was 26.0% (FWHM) (Doke, Kikuchi, and Nishikido, 2006). The resolution of the time difference spectrum between the two detectors was 514 ps (FWHM) for annihilation gamma rays. For a central volume of $5\times5\times5$ mm^3 an even better time resolution of 253 ps was obtained. It is expected that the time resolution improves inversely proportional to $\sqrt{N_{pe}}$, i.e., an increase in the quantum efficiency or the light collection efficiency will improve the timing. This is within reach, based on available PMTs with significantly better quantum efficiency, compared to the PMTs used in the Waseda prototype. With a time resolution of 300 ps, one will be able to reduce the number of background events. A full-scale TOF PET, with an axial sensitive length of 24 cm, has been proposed by the Waseda group (see Fig. 85) (Nishikido, 2005; Doke, Kikuchi, and Nishikido, 2006).

Another proposal for a LXe TOF PET was recently made by the Grenoble group (Gallin-Martel *et al.*, 2006; Gallin-Martel, 2008), applying a light division method to measure the position in the axial direction. However, the reported position resolution was only about 10 mm (FWHM) in the central region, not competitive with what is achieved in commercially available crystal PET. Simulation results show much better performance, but unfortunately the large discrepancy is not yet understood or explained.

Clearly more studies are required to establish LXe Compton or TOF detectors as an alternative to classical crystal PET systems. LXe based detectors require associated systems (from cryogenics to gas handling and purification) which are typically perceived as complex and costly, contributing to some reluctance in their use, especially as diagnostic tools in medicine. In the last few years, however, many significant technological advances have resulted in large LXe detector systems operating

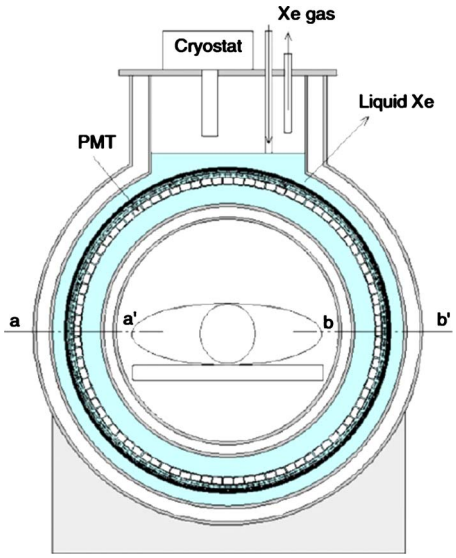

FIG. 85. (Color online) Schematic of the Waseda full scale LXe TOF-PET (Doke, Kikuchi, and Nishikido, 2006).

for many months with excellent and stable performance. In particular, the LXe detectors deployed underground for dark matter searches (see Sec. IV.B) have proven that long term stability, reliability, and also safety issues can be confidently solved.

V. SUMMARY

We have reviewed the current state of the art in liquid xenon detectors and associated principles of operation and performance characteristics. We could not expand on many topics to the extent we would have liked, yet we have attempted to gather the most relevant information from past and recent experimental work on liquid xenon detectors developed for a variety of applications. It is our wish that this article may be a useful resource especially for the new generation of investigators who are turning with enthusiasm to this material for the detection and measurement of different particles in different fields. Recent years have seen an increased interest in liquid xenon detectors and a development of related technologies driven by rare event searches from dark matter to neutrinoless double beta decay. The rate at which the performance of liquid xenon detectors has improved in the last ten years is encouraging. Yet, much work remains to be done in many areas, including a better understanding of the response of LXe to low-energy particles and of the factors affecting the energy resolution. As the scale of some of these experiments grows, so does the challenge to push the performance limit in order to improve the detection sensitivity. Additional challenges for multiton scale LXe detectors will be associated with the availability of xenon, its cost, and purification. The next ten years will bring to fruition many of the ongoing experiments and others now in the planning phase. We are confident that these will make far-reaching contributions to some of the most important questions in physics today. It is also encouraging to see a rapid development of liquid xenon detectors for improved imaging in medicine, a practical application benefiting society as a whole.

ACKNOWLEDGMENTS

We thank the many colleagues who share our passion for this topic and who have contributed to the advancement of liquid xenon detectors. Special thanks go to the many students and young researchers who are working on the experiments covered in this article committed to their success. One of us (E.A.) thanks her graduate students Bin Choi, Luke Goetzke, and Guillaume Plante for their assistance in preparing the article. She gratefully acknowledges support from the National Science Foundation for her research on liquid xenon detectors, specifically for the XENON dark matter project, under Award No. PHY-0705337.

REFERENCES

Abe, K., *et al.*, 2008, J. Phys.: Conf. Ser. **120**, 042022.
Akimov, D., *et al.*, 1995, IEEE Trans. Nucl. Sci. **42**, 2244.
Akimov, D., *et al.*, 1996, Nucl. Instrum. Methods Phys. Res. A **379**, 484.
Akimov, D., *et al.*, 2002, Phys. Lett. B **524**, 245.
Alkhazov, G. D., 1972, Sov. Phys. Tech. Phys. **16**, 1540.
Alner, G. J., *et al.*, 2007, Astropart. Phys. **28**, 287.
Alvarez, L. W., 1968, Lawrence Radiation Laboratory, Physics Notes 672 (unpublished).
Anderson, D. F., 1986, Nucl. Instrum. Methods **242**, 254.
Angle, J., *et al.*, 2008a, Phys. Rev. Lett. **101**, 091301.
Angle, J., *et al.* (XENON Collaboration), 2008b, Phys. Rev. Lett. **100**, 021303.
Aprile, E., and L. Baudis, 2008, Proceedings of Science (IDM2008)018.
Aprile, E., R. Mukherjee, and M. Suzuki, 1990, IEEE Trans. Nucl. Sci. **37**, 553.
Aprile, E., R. Mukherjee, and M. Suzuki, 1991a, Nucl. Instrum. Methods Phys. Res. A **302**, 177.
Aprile, E., R. Mukherjee, and M. Suzuki, 1991b, Nucl. Instrum. Methods Phys. Res. A **307**, 119.
Aprile, E., R. Mukherjee, and M. Suzuki, 1991c, Nucl. Instrum. Methods Phys. Res. A **300**, 343.
Aprile, E., and M. Suzuki, 1989, IEEE Trans. Nucl. Sci. **36**, 311.
Aprile, E. (XENON100 Collaboration), 2009, Ann. Isr. Phys. Soc. **1166**, 205.
Aprile, E., *et al.*, 1989, Proc. SPIE **1159**, 259.
Aprile, E., *et al.*, 1993, Phys. Rev. A **48**, 1313.
Aprile, E., *et al.*, 1995, Astrophys. J. **453**, 685.
Aprile, E., *et al.*, 1998, Nucl. Instrum. Methods Phys. Res. A **412**, 425.
Aprile, E., *et al.*, 2000, Proc. SPIE **4140**, 333.
Aprile, E., *et al.*, 2002, Nucl. Instrum. Methods Phys. Res. A **480**, 636.
Aprile, E., *et al.*, 2003, e-print arXiv:astro-ph/0212005.
Aprile, E., *et al.*, 2004a, IEEE Trans, No. 5.
Aprile, E., *et al.*, 2004b, New Astron. Rev. **48**, 257.
Aprile, E., *et al.*, 2005, Phys. Rev. D **72**, 072006.
Aprile, E., *et al.*, 2006, Phys. Rev. Lett. **97**, 081302.
Aprile, E., *et al.*, 2007a, Phys. Rev. B **76**, 014115.

Aprile, E., *et al.*, 2007b, Nucl. Instrum. Methods Phys. Res. B **173**, 113.
Aprile, E., *et al.*, 2008, Nucl. Instrum. Methods Phys. Res. A **593**, 414.
Aprile, E., *et al.*, 2009, Phys. Rev. C **79**, 045807.
Aprile, E., *et al.*, 2010, e-print arXiv:1001.2834.
Arisaka, K., *et al.*, 2009, Astropart. Phys. **31**, 63.
Arneodo, F., *et al.*, 2000, Nucl. Instrum. Methods Phys. Res. A **449**, 147.
Asaf, U., and I. T. Steinberger, 1974, Phys. Rev. B **10**, 4464.
Atwood, W. B., *et al.*, 2009, http://xxx.lanl.gov/abs/0902.1089.
Avignone, T., G. S. King, and Y. U. Zdesenko, 2005, New J. Phys. **7**, 6.
Bakale, G., U. Sowadaand, and W. F. Schmidt, 1976, J. Phys. Chem. **80**, 2556.
Baldini, A., *et al.*, 2002, Research Proposal to INFN, The MEG experiment, search for the $\mu \rightarrow e\gamma$ decay at PSI (unpublished).
Baldini, A., *et al.*, 2005, Nucl. Instrum. Methods Phys. Res. A **545**, 753.
Baldini, A., *et al.*, 2006, Nucl. Instrum. Methods Phys. Res. A **565**, 589.
Barabanov, I. R., *et al.*, 1986, JETP Lett. **43**, 210.
Barabash, A. S., and A. I. Bolozdynia, 1989, JETP Lett. **49**, 356.
Barabash, A. S., and A. I. Bolozdynia, 1993, *Liquid Ionization Detectors* (Energoatomizdat, Moscow).
Baranov, A., *et al.*, 1990, Nucl. Instrum. Methods Phys. Res. A **294**, 439.
Barkov, L. M., *et al.*, 1996, Nucl. Instrum. Methods Phys. Res. A **379**, 482.
Beaglehole, D., 1965, Phys. Rev. Lett. **15**, 551.
Bernabei, R., *et al.*, 2001, EPJdirect **3**, 1.
Bernabei, R., *et al.*, 2002, Phys. Lett. B **546**, 23.
Bernstorff, S., *et al.*, 1983, Ann. Isr. Phys. Soc. **6**, 270.
Bolotnikov, A., and B. Ramsey, 1997, Nucl. Instrum. Methods Phys. Res. A **396**, 360.
Bolozdynya, A., *et al.*, 1995, IEEE Trans. Nucl. Sci. **NS-42**, 565.
Bolozdynya, A., *et al.*, 2006, *Noble Gas Detectors* (Wiley-VCH Verlag, Berlin), Chap. 5.
Braem, A., *et al.*, 1992, Nucl. Instrum. Methods Phys. Res. A **320**, 228.
Breskin, A., *et al.*, 2009, Nucl. Instrum. Methods Phys. Res. A **598**, 107.
Bressi, G., *et al.*, 1998, Nucl. Phys. B **513**, 555.
Brooks, M. L., *et al.*, 1999, Phys. Rev. Lett. **83**, 1521.
Brown, S. G., and S. A. Bludman, 1964, Phys. Rev. **136**, B1160.
Bunemann, O., T. E. Cranshow, and A. Harvey, 1949, Can. J. Res., Sect. A **27**, 191.
Carugno, G., *et al.*, 1993, Nucl. Instrum. Methods Phys. Res. A **335**, 338.
Carugno, G., *et al.*, 1996, Nucl. Instrum. Methods Phys. Res. A **376**, 149.
Cennini, P., *et al.*, 1994, Nucl. Instrum. Methods Phys. Res. A **346**, 550.
Chen, M., *et al.*, 1988, Nucl. Instrum. Methods Phys. Res. A **267**, 43.
Chen, M., *et al.*, 1993, Nucl. Instrum. Methods Phys. Res. A **327**, 187.
Chepel, V. Y., *et al.*, 1994, Nucl. Instrum. Methods Phys. Res. A **349**, 500.
Chepel, V. Y., *et al.*, 1995, Nucl. Instrum. Methods Phys. Res. A **367**, 58.
Chepel, V. Y., *et al.*, 1997, Nucl. Instrum. Methods Phys. Res. A **392**, 427.
Chepel, V. Y., *et al.*, 1999, IEEE Trans. Nucl. Sci. **NS-46**, 1038.
Chepel, V. Y., *et al.*, 2001, Proceedings on the International Workshop on Technique and Application of Xenon Detectors (Xenon 01), University of Tokyo (unpublished).
Chepel, V. Y., *et al.*, 2006, Astropart. Phys. **26**, 58.
Conti, E., 2003, Phys. Rev. B **68**, 054201.
Crawford, H. J., *et al.*, 1987, Nucl. Instrum. Methods Phys. Res. A **256**, 47.
Crawford, R. K., M. L. Klein, and J. A. Venables, 1977, *Rare Gas Solids* (Academic, London).
Crespo, P., *et al.*, 1998, IEEE Trans. Nucl. Sci. **NS-45**, 561.
Crespo, P., *et al.*, 2000, IEEE Trans. Nucl. Sci. **NS-47**, 2119.
Curioni, A., *et al.*, 2003, Proc. SPIE **4851**, 1293.
Curioni, A., *et al.*, 2007, Nucl. Instrum. Methods Phys. Res. A **576**, 350.
de Lima, E. P., *et al.*, 1982, Nucl. Instrum. Methods **192**, 575.
Derenzo, S. E., *et al.*, 1974, Phys. Rev. A **9**, 2582.
Diehl, R., N. Prantzos, and P. von Ballmoos, 2006, Nucl. Phys. A **777**, 70.
Diehl, R., *et al.*, 2008, New Astron. Rev. **52**, 440.
Doke, T., 1969, Radiat. Phys. **1**, 24.
Doke, T., 1980, Port. Phys. **12**, 9.
Doke, T., 1982, Nucl. Instrum. Methods **196**, 87.
Doke, T., 1993, Nucl. Instrum. Methods Phys. Res. A **327**, 113.
Doke, T., K. Kasahara, and D. J. Suson, 1992, Jpn. J. Appl. Phys., Part 1 **31**, 3668.
Doke, T., J. Kikuchi, and F. Nishikido, 2006, Nucl. Instrum. Methods Phys. Res. A **569**, 863.
Doke, T., and K. Masuda, 1999, Nucl. Instrum. Methods Phys. Res. A **420**, 62.
Doke, T., R. Sawada, and H. Tawara, 2001, Nuclear Proceedings of the International Workshop on Technique and Application of Xenon Detectors (Xenon No1), University of Tokyo (unpublished).
Doke, T., *et al.*, 1976, Nucl. Instrum. Methods **134**, 353.
Doke, T., *et al.*, 1985, Nucl. Instrum. Methods Phys. Res. A **237**, 475.
Doke, T., *et al.*, 1988, Nucl. Instrum. Methods Phys. Res. A **269**, 291.
Doke, T., *et al.*, 1989, Nucl. Phys. B, Proc. Suppl. **10B**, 150.
Doke, T., *et al.*, 1992, Nucl. Instrum. Methods Phys. Res. A **316**, 58.
Doke, T., *et al.*, 2002, Jpn. J. Appl. Phys., Part 1 **41**, 1538.
Dolgoshein, B. A., *et al.*, 1967, JETP Lett. **6**, 224.
Duval, S., *et al.*, 2009, JINST **4** (12), P12008.
Egorov, V. V., V. Ermilova, and B. Rodionov, 1982, Lebedev Physical Institute Report No. 166.
Egorov, V. V., *et al.*, 1983, Nucl. Instrum. Methods Phys. Res. A **205**, 373.
Fano, U., 1947, Phys. Rev. **72**, 26.
Feldman, G. J., and R. D. Cousins, 1998, Phys. Rev. D **57**, 3873.
Frish, O. R., 1945, British Atomic Energy Report BR 49.
Gaitskell, R., 2008, Proceedings of Science (IDM2008)018.
Gallin-Martel, M.-L., 2008, e-print arXiv:0810.2956.
Gallin-Martel, M.-L., *et al.*, 2006, Nucl. Instrum. Methods Phys. Res. A **563**, 225.
Gatti, E., G. Padovini, L. Quartapelle, N. E. Greenlaw, and V. Radeka, 1979, IEEE Trans. Nucl. Sci. **26**, 2910.
Giboni, K., *et al.*, 2005, IEEE Trans. Nucl. Sci. **52**, 1800.
Giboni, K., *et al.*, 2007, JINST **2**, 10001.
Giomataris, Y., *et al.*, 1996, Nucl. Instrum. Methods Phys. Res.

A **376**, 29.
Gratta, G., 2009, private communication.
Grignon, C., *et al.*, 2007, Nucl. Instrum. Methods Phys. Res. A **571**, 142.
Gruhn, C. R., and R. Loveman, 1977, IEEE Trans. Nucl. Sci. **NS-26**, 110.
Gushchin, E. M., A. A. Kinglov, and I. M. Obodovski, 1982, Zh. Eksp. Teor. Fiz. **82**, 1114 [Sov. Phys. JETP **55**, 650 (1982)].
Haruyama, T., *et al.*, 2004, Adv. Cryog. Eng. **49**, 1459.
Hilt, O., and W. F. Schmidt, 1994, J. Phys.: Condens. Matter **6**, L735.
Hitachi, A., T. Doke, and A. Mozumder, 1992, Phys. Rev. B **46**, 11463.
Hitachi, A., *et al.*, 1983, Phys. Rev. B **27**, 5279.
Hitachi, A., *et al.*, 1997, Phys. Rev. B **55**, 5742.
Hitachi, A., *et al.*, 2005, Astropart. Phys. **24**, 247.
Hollis Hallet, A. C., 1961, in *Argon, Helium and the Rare Gases: The Elements of the Helium Group. Vol. 1, History Occurrences and Properties*, edited by G. A. Cook (Interscience, New York), Chap. IX.
Ichige, M., *et al.*, 1993, Nucl. Instrum. Methods Phys. Res. A **333**, 355.
Ichinose, H., *et al.*, 1992, Nucl. Instrum. Methods Phys. Res. A **322**, 216.
Ishida, N., *et al.*, 1997, Nucl. Instrum. Methods Phys. Res. A **384**, 380.
Jaffé, C., 1913, Ann. Phys. **347**, 303.
Jortner, J., *et al.*, 1965, J. Chem. Phys. **42**, 4250.
Jungman, G., M. Kamionkowski, and K. Griest, 1996, Phys. Rep. **267**, 195.
Kashiwagi, T., *et al.*, 1993, Nucl. Instrum. Methods Phys. Res. A **327**, 148.
Klein, C. A., 1968, J. Appl. Phys. **39**, 2029.
Knoll, G. F., 2000, *Radiation Detection and Measurement* (Wiley, New York).
Kramers, H. A., 1952, Physica (Utrecht) **18**, 665.
Kubota, S., M. Hishida, and J. Ruan, 1978, J. Phys. C **11**, 2645.
Kubota, S., *et al.*, 1978, Phys. Rev. B **17**, 2762.
Kubota, S., *et al.*, 1979, Phys. Rev. B **20**, 3486.
Lansiart, A., *et al.*, 1976, Nucl. Instrum. Methods **135**, 47.
Lavoie, L., 1976, Med. Phys. **3**, 283.
Lebedenko, V. N., 2008, e-print arXiv:0812.1150.
Leonard, D., *et al.* (EXO Collaboration), 2008, Nucl. Instrum. Methods Phys. Res. A **591**, 490.
Lindhard, J., 1963, Mat. Fys. Medd. K. Dan. Vidensk. Selsk. **33**, 1.
Lippincott, W. H., *et al.*, 2008, Phys. Rev. C **78**, 035801.
Lopes, M. I., *et al.*, 1995, IEEE Trans. Nucl. Sci. **NS-42**, 2298.
Luke, P. N., 1995, IEEE Trans. Nucl. Sci. **NS-42**, 207.
Masuda, K., T. Doke, and T. Takahashi, 1981, Nucl. Instrum. Methods Phys. Res. **188**, 629.
Masuda, K., *et al.*, 1979, Nucl. Instrum. Methods **160**, 247.
Masuda, K., *et al.*, 1989, Phys. Rev. A **39**, 4732.
Mihara, S., 2004, Nucl. Instrum. Methods Phys. Res. A **518**, 45.
Mihara, S., *et al.*, 2002, IEEE Trans. Nucl. Sci. **NS-49**, 588.
Mihara, S., *et al.*, 2004, Cryogenics **44**, 223.
Mihara, S., *et al.*, 2006, Cryogenics **46**, 688.
Miller, L. S., S. Howe, and W. E. Spear, 1968, Phys. Rev. **166**, 871.
Miyajima, M., S. Sasaki, and E. Shibamura, 1995, Nucl. Instrum. Methods Phys. Res. A **352**, 548.
Miyajima, M., *et al.*, 1974, Phys. Rev. A **9**, 1438.
Mozumder, A., 1995, Chem. Phys. Lett. **245**, 359.
Muller, R. A., *et al.*, 1971, Phys. Rev. Lett. **27**, 532.
Neilson, R., *et al.*, 2009, Nucl. Instrum. Methods Phys. Res. A **608**, 68.
Ni, K., *et al.*, 2005, Nucl. Instrum. Methods Phys. Res. A **551**, 356.
Nishikido, F., 2005, Ph.D. thesis (Waseda University).
Nishikido, F., *et al.*, 2004, Jpn. J. Appl. Phys. **43**, 779.
Nishikido, F., *et al.*, 2005, Jpn. J. Appl. Phys. **44**, 5193.
Oberlack, U. G., *et al.*, 2000, Proc. SPIE **4141**, 168.
Obodovsky, I. M., K. T. Ospanov, and S. G. Pokachalov, 2003, Moscow Eng. Phys. Inst. Report No. 006-93.
Okada, H., *et al.*, 2000, Nucl. Instrum. Methods Phys. Res. A **451**, 427.
Onsager, L., 1938, Phys. Rev. **54**, 554.
Ootani, W., 2005, Proceedings of the Second International Workshop on Applications of Rare Gas Xenon to Science and Technology (XeSAT2005) (unpublished), p. 132.
Orito, S., and Mori, 1997, The Workshop on a New $\mu \rightarrow e\gamma$ Decay Experiment at PSI (unpublished).
O'Sullivan, K., *et al.*, 2007, J. Phys.: Conf. Ser. **120**, 052056.
Owen, A., G. W. Fraser, and K. J. MacCarthy, 2002, Nucl. Instrum. Methods Phys. Res. A **491**, 43.
Ozone, K., 2005, Ph.D. thesis (University of Tokyo).
Pack, J. L., R. E. Voshhall, and A. V. Phelps, 1962, Phys. Rev. **127**, 2084.
Platzman, R. L., 1961, Int. J. Appl. Radiat. Isot. **10**, 116.
Policarpo, A. J. P. L., *et al.*, 1974, Nucl. Instrum. Methods **118**, 221.
Policarpo, A. J. P. L., *et al.*, 1982, Nucl. Instrum. Methods **196**, 53.
Prunier, J., V. F. Pisarev, and G. S. R. Revenko, 1973, Nucl. Instrum. Methods **109**, 257.
PSI, 1999, Research Proposal to Paul Scherrer Institute, "Search for $\gamma^+ \rightarrow e^+\gamma$, down to 10^{-14} branching ratio" (unpublished).
Radermacher, E., *et al.*, 1992, in *Instrumentation in High Energy Physics*, edited by F. Sauli, Advanced Series on Directions in High Energy Physics Vol. 9 (World Scientific, Singapore), pp. 387–511.
Reininger, R., *et al.*, 1982, Phys. Rev. B **26**, 6294.
Reininger, R., *et al.*, 1984, Chem. Phys. **86**, 189.
Robson, R. E., 1972, Aust. J. Phys. **25**, 685.
Rossler, V., 1971, Phys. Status Solidi B **45**, 483.
Rubbia, C., 1977. CERN Report No. CERN-EP/77-08.
Sano, T., *et al.*, 1989, Nucl. Instrum. Methods Phys. Res. A **275**, 346.
Sawada, R., *et al.*, 2007, Nucl. Instrum. Methods Phys. Res. A **581**, 522.
Schmidt, W. F., 2001, Proceedings of the International Workshop on Technique and Application of Xenon Detectors, University of Tokyo, Japan (unpublished).
Schwenter, N., E.-E. Kock, and J. Jortner, 1985, *Electronic Excitations in Condensed Rare Gases*, Springer Tracts in Modern Physics (Springer-Verlag/Elsevier, New York).
Seguinot, G., *et al.*, 1992, Nucl. Instrum. Methods Phys. Res. A **323**, 583.
Seidel, G. M., R. E. Lanou, and W. Yao, 2002, Nucl. Instrum. Methods Phys. Res. A **489**, 189.
Shibamura, E., *et al.*, 1975, Nucl. Instrum. Methods **131**, 249.
Shibamura, E., *et al.*, 1995, Jpn. J. Appl. Phys., Part 1 **34**, 1897.
Shibamura, E., *et al.*, 2009, Jpn. J. Appl. Phys., Part 2 (to be published).
Shockley, W., 1961, Czech. J. Phys., Sect. B **11**, 81.

Signorelli, G., 2004, Ph.D. thesis (Scuola Normale Superiore, Pisa).
Solovov, V., *et al.*, 2002a, Nucl. Instrum. Methods Phys. Res. A **477**, 184.
Solovov, V., *et al.*, 2002b, Nucl. Instrum. Methods Phys. Res. A **478**, 435.
Solovov, V., *et al.*, 2002c, Nucl. Instrum. Methods Phys. Res. A **488**, 572.
Solovov, V., *et al.*, 2003, IEEE Trans. Nucl. Sci. **NS-50**, 122.
Solovov, V., *et al.*, 2004, Nucl. Instrum. Methods Phys. Res. A **516**, 462.
Steinberger, I. T., and U. Asaf, 1973, Phys. Rev. B **8**, 914.
Subtil, J. L., *et al.*, 1987, Phys. Status Solidi B **143**, 783.
Suzuki, S., *et al.*, 1986, Nucl. Instrum. Methods Phys. Res. A **245**, 78.
Suzuki, Y., 2008, Proceedings of Science (IDM2008)018.
Takahashi, T., *et al.*, 1975, Phys. Rev. A **12**, 1771.
Takizawa, K., *et al.*, 2002, Proc. SPIE **4851**, 1294.
Tanaka, M., *et al.*, 2001, Nucl. Instrum. Methods Phys. Res. A **457**, 454.
Terasawa, K., *et al.*, 1998, Advanced Research Institute for Science and Engineering, Waseda University Technical Report No. 98-12.
Thomas, J., D. A. Imel, and S. Biller, 1988, Phys. Rev. A **38**, 5793.
Yamashita, M., *et al.*, 2004, Nucl. Instrum. Methods Phys. Res. A **535**, 692.
Yoshino, Y., U. Spwada, and W. F. Schmidt, 1976, Phys. Rev. A **14**, 438.
Zaklad, H., *et al.*, 1972, IEEE Trans. Nucl. Sci. **NS-19**, 206.
Zimmerer, G., 1998, J. Low Temp. Phys. **111**, 629.